Growth and Characterization of ZnSe by Metalorganic and Gas Source Molecular Beam Epitaxy

By

Christopher Alan Coronado

B.S. Physics, University of Washington, 1984
M.S. Electrical Engineering, University of Michigan, 1987

Submitted to the Department of Materials Science and Engineering
in partial fulfillment of
the requirements for the degree of

DOCTOR OF PHILOSOPHY
IN ELECTRONIC MATERIALS

at the

Massachusetts Institute of Technology
May, 1994

© Massachusetts Institute of Technology, 1994. All rights reserved.

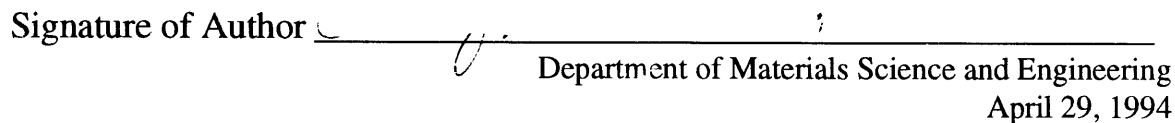

Signature of Author
Department of Materials Science and Engineering
April 29, 1994

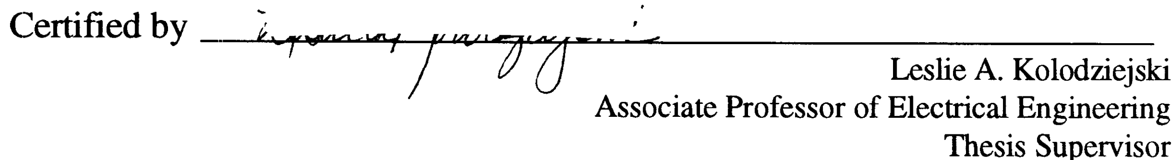

Certified by
Leslie A. Kolodziejski
Associate Professor of Electrical Engineering
Thesis Supervisor

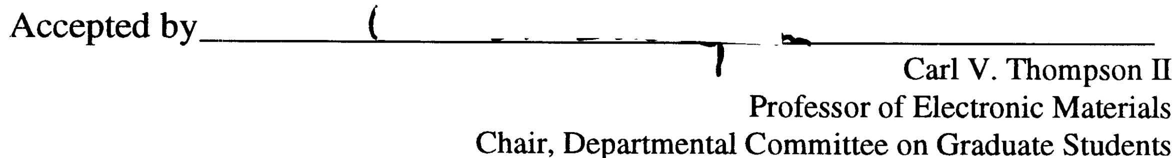

Accepted by
Carl V. Thompson II
Professor of Electronic Materials
Chair, Departmental Committee on Graduate Students

Science
MASSACHUSETTS INSTITUTE
OF TECHNOLOGY

AUG 18 1994

LIBRARIES

Growth and Characterization of ZnSe by Metalorganic and Gas Source Molecular Beam Epitaxy

by

Christopher Alan Coronado

Submitted to the Department of Materials Science and Engineering
on April 29, 1994, in partial fulfillment of the requirements for
the degree of Doctor of Philosophy

Abstract

ZnSe was grown using the gaseous source epitaxial methods of metalorganic molecular beam epitaxy (MOMBE) and gas source molecular beam epitaxy (GSMBE). A nitrogen plasma source was used during GSMBE to incorporate the *p*-type dopant nitrogen into ZnSe epitaxial layers.

The first part of this work was the growth of undoped ZnSe by MOMBE. Diethylzinc and diethylselenium were the primary metalorganic source gases used. The MOMBE growth rate was less than 400 Å/hr when a diethyl metalorganic was the source of Zn and/or Se. The low growth rate is postulated to be the result of surface passivation of metal incorporation sites by chemisorbed ethyl radicals. A parallel study of the effects of laser illumination and electron-beam irradiation during MOMBE growth was also conducted. Laser illumination and electron-beam irradiation were observed to alter the growth rate under appropriate growth conditions. An increase in the growth rate by a factor of 15 over the unilluminated growth rate was observed using laser illumination.

The second part of the study was the growth of ZnSe by GSMBE, and experiments to dope ZnSe *p*-type using a radio frequency (RF) nitrogen plasma source. High quality epitaxial films were produced under a variety of growth conditions as indicated by intense low temperature photoluminescence dominated by free- and donor-bound exciton features. Employing the RF plasma source, nitrogen has been incorporated into ZnSe epitaxial layers in concentrations as high as 6×10^{18} N atoms/cm^3, as measured by secondary ion mass spectroscopy. Hydrogen incorporated in the ZnSe:N grown by GSMBE. Passivation of the nitrogen acceptors by hydrogen greatly reduced the electrically-active nitrogen concentrations; the highest net-acceptor concentration measured by the capacitance-voltage technique was ~ 1×10^{17} cm^{-3}.

Thesis Supervisor: Leslie A. Kolodziejski

Title: Associate Professor of Electrical Engineering

Contents

Abstract **2**

Acknowledgements **14**

Glossary of Acronyms Used in Thesis **15**

1 Introduction **17**

1.1 Background 17

1.1.1 Progress Toward Blue-Green Injection Lasers 17

1.1.2 (Zn,Mg)(S,Se) and (Zn,Cd)(S,Se) Material Systems 19

1.1.3 Material Properties of ZnSe 20

1.1.4 Technological Applications 22

1.1.5 Central Materials Issues 24

1.2 Dissertation Overview 25

1.2.1 Epitaxy System and Experimental Procedures 25

1.2.2 MOMBE and GSMBE 25

1.2.3 Acceptor Compensation in ZnSe 26

1.2.4 ZnSe:N 26

1.2.5 Conclusions and Future Work 27

2 Epitaxy System and Experimental Procedures **28**

2.1 II-VI Chamber Description 30

2.2 Gas Delivery System 33

2.3 Sample Preparation 34

2.3.1 Sample Holder 34

2.3.2 Wafer Preparation 35

2.4 Temperature Calibration 36

2.5 Other Growth Procedures 37

3 Metalorganic Molecular Beam Epitaxy of ZnSe 38
3.1 Instability in MBE Source Fluxes 38
3.2 Metalorganic Gas Sources 40
3.3 Growth Conditions 41
3.4 Low MOMBE Growth Rate 44
3.4.1 Addition of Hydrogen Gas 45
3.4.2 Mixed Source Experiments 46
3.4.3 Site Blockage by Ethyl Radicals 48
3.4.4 Other Reported MOMBE Results 51
3.5 Laser-Assisted MOMBE 53
3.5.1 Laser-Assisted Growth Set-Up 54
3.5.2 Growth Rate Enhancement 56
3.5.3 Intensity Dependence 57
3.5.4 Wavelength Dependence 58
3.5.5 Flow Ratio Dependence 62
3.6 MOMBE Using DMZn and Solid Se 63
3.7 Electron-Beam Assisted Growth 64
3.8 Model for Laser-Assisted Growth. 65
3.9 ZnSe Film Characterization 73
3.9.1 RHEED 73
3.9.2 DCXRD 75
3.9.3 Photoluminescence 77
3.9.3.1 Representative PL of a MOMBE Thin Film 77
3.9.3.2 Laser Tuning of Stoichiometry 78
3.9.3.3 MBE PL 80
3.10 Summary 81

4 Gas Source MBE of ZnSe 84
4.1 GSMBE Growth 84
4.1.1 Growth Conditions 85
4.1.2 H_2Se Cracking 86
4.1.3 Estimate of Growth Rate Uncertainty 87

4.1.4 Growth Rate Dependencies 88
4.1.4.1 Substrate Temperature 89
4.1.4.2 H_2Se Flow and Zn Flux 90
4.2 Characterization of GSMBE films 91
4.2.1 Structural Characterization 91
4.2.1.1 RHEED 92
4.2.1.2 Nomarski and Scanning Electron Microscopy 93
4.2.2 Photoluminescence 96
4.2.3 Electrical Measurements 99
4.3 Effect of Surface Stoichiometry 99
4.5 Summary 101

5 Acceptor Compensation in *P*-Type ZnSe 103
5.1 Early Compensation Model: Native Defects 105
5.2 Recent Compensation Models 106
5.2.1 Lattice Relaxation Models 107
5.2.2 Solubility Limits of Dopants 109

6 Doping With Nitrogen During GSMBE 111
6.1 Radio Frequency Plasma Source 112
6.1.1 Description 112
6.1.2 Operation 114
6.2 ZnSe:N Produced Using a RF Plasma Source 115
6.2.1 Evidence of Nitrogen Incorporation 116
6.2.1.1 Photoluminescence 116
6.2.1.2 Secondary Ion Mass Spectroscopy 118
6.2.2 Plasma Doping Dependencies 120
6.2.2.1 Nitrogen Flow Rate 120
6.2.2.2 RF Power 120
6.2.2.3 Growth Temperature 121
6.2.2.4 Surface Stoichiometry 122
6.3 Characterization of ZnSe:N 123
6.4 Summary 127

7 Outstanding Issues in Nitrogen Doping 129
7.1 Hydrogenation 129
7.1.1 Experimental Evidence of N-H bond in OMVPE Grown ZnSe 129
7.1.2 Possibilities to Reverse Hydrogen Passivation. 131
7.2 Compensation in Heavily Doped ZnSe:N 132
7.2.1 Evidence of a Deep Donor State 132
7.2.2 Proposed Models for Compensation 133

8 Summary and Suggested Future Work 135

Appendix A RHEED 140

Appendix B DCXRD 143

Appendix C Photoluminescence 145

Appendix D Estimate of GSMBE Growth Rate Uncertainty 149

Bibliography 153

List of Figures

Figure 1.1 Bandgap energy versus lattice constant diagram of important compounds in current II-VI light emitting device research........................ 19

Figure 2.1 Diagram illustrating the layout of the interconnected UHV epitaxy systems within the CBE laboratory. The UHV chambers and the major subsystems are identified by name.. 29

Figure 2.2 Top and side view drawings of the II-VI epitaxy chamber which illustrate the geometry of the chamber. The locations of the sources and some key analytical equipment are also shown. 30

Figure 2.3 Detailed view of the high temperature gas cracker. The gas tube wall is PBN and the baffle insert is made of Ta. 32

Figure 2.4 Representative gas routing arrangement on II-VI reactor. A vent-run configuration is used near the cracker switching block to suppress gas flow transients. 34

Figure 3.1 Schematic illustration of growth rate dependence of MOMBE on the growth temperature. 41

Figure 3.2 MOMBE growth rate versus the growth temperature for all experimental conditions investigated when at least one diethyl metalorganic was used. 45

Figure 3.3 Schematic drawing illustrating light path in laser-assisted growth experiments. M indicates the location of a mirror and V indicates the viewport. 54

Figure 3.4 Growth rate versus substrate temperature for regions of a film which were illuminated (•) by the laser, and received no illumination (∘). The gas flows were 2.5 and 0.5 sccm for DEZn and DESe, respectively, and the laser illumination wavelength was 458 nm. 56

Figure 3.5 A thickness profile measured from the center of a laser enhanced growth spot to the edge of the unilluminated region. 58

Figure 3.6 The dependence of the growth rate enhancement during MOMBE (solid points and crosses), and the growth rate suppression during MBE (open circles), as a function of laser illumination energy. The bandgap E_g of ZnSe at a growth temperature of 320 °C is indicated by the arrow. 59

Figure 3.7 Illustration of dependence of growth rate on the gas flow ratios. The DEZn:DESe (II/VI) flow ratio dependence is shown in (a). The flow ratio is inverted in (b) for clarity of presentation of the II/VI ratios less than unity. In these experiments the growth temperature was 320°C, the DEZn and DESe flows ranged from 0.25-2.5 sccm, and the laser illumination wavelength was 458 nm. 62

Figure 3.8 Drawing of possible surface reactions proposed to explain the observed necessary conditions for growth rate enhancement in the MOMBE of ZnSe using at least one diethyl metalorganic source gas. Holes generated by a laser or electron-beam drift to the surface and participate in anti-bonding reactions which free Zn metal sites and remove an ethyl radical through the formation of a volatile species containing C_2H_5 which subsequently desorbs. 70

Figure 3.9 The top left figure (a) represents the proposed dependence of the Zn, Se, and C_2H_5 desorption rates on the photon flux Φ. The bottom left figure (b) is the postulated dependence of the Zn incorporation rate on laser photon flux. The laser-assisted growth rate which is the difference in the deposition rate (proportional to Zn incorporation) and the etching rate (proportional to re-evaporation of Se) is shown in figure (c) to the right. 72

Figure 3.10 Post-growth RHEED photographs of a ZnSe(100) surface in the (a) <011> and (b) <010> azimuths. The two-fold reconstruction in the <010> azimuth and no reconstruction in the <011> direction indicates a Zn-rich surface. 74

Figure 3.11 (400) x-ray reflection of a 1000 Å thick ZnSe film on GaAs. The angular separation of nearly 780 arcseconds indicates the film is pseudomorphic. 76

Figure 3.12 Low temperature (10 K) photoluminescence of a MOMBE thin film grown using DEZn and DESe sources. The PL spectrum in (a) is from an unilluminated region that was 1100 Å thick. The spectrum in (b) is from a laser illuminated region 3400 Å thick. 78

Figure 3.13 Low temperature photoluminescence illustrating tuning of stoichiometry by laser illumination. The spectrum in (a) is dominated by deep level recombination. Laser illumination was observed to dramatically improve the optical properties of the ZnSe film as shown in (b) where the PL spectrum is now dominated by an exciton feature in the near-bandedge. 79

Figure 3.14 Low temperature (10 K) PL of a ZnSe film grown by MBE. The intense exciton features in the near-bandedge and absence of deep level recombination indicate good film quality. 80

Figure 4.1 Growth rate versus the H_2Se cracking temperature illustrating the approximate 700 °C threshold for growth to occur. The growth conditions for these experiments are summarized in Table 4.2. 86

Figure 4.2 Dependence of the growth rate on the growth temperature. The growth conditions of the films whose growth rates are represented by the solid points were grown with a H_2Se flow rate of 2.5 sccm and an average Zn flux of 0.7 Å/s. The H_2Se flow rate was 1.7 sccm and the average Zn flux was 1.0 Å/s for the data represented by the open circles. The dotted line is a linear approximation to the growth rate temperature dependence. 89

Figure 4.3 Growth rate is a linear function of the H_2Se flow rate indicating that arrival of Se to surface is limiting the growth rate. 90

Figure 4.4 Photographs of post-growth RHEED images. The faint two-fold reconstruction in the <011> azimuth (a), and no reconstruction in the <010> direction (b) indicate the final surface was slightly Se-rich. 92

Figure 4.5 SEM image of the typical surface morphology of ZnSe films grown by GSMBE. The scale is indicated by the line on the bottom of the photograph. The white region is a dust particle which was used as an aid in focusing. 93

Figure 4.6 Photograph taken using the Nomarski microscope of a film which was grown at an approximate substrate temperature of 250 °C. Magnification is 1000x. 94

Figure 4.7 SEM image of a ZnSe film where the substrate temperature fell below 250 °C during growth. Pits with three-fold symmetry are visible on the surface. The scale is indicated by the white line at the bottom of the photograph. 95

Figure 4.8 Low temperature (10 K) photoluminescence of ZnSe as a function of the growth temperature. The donor-bound exciton feature at 2.798 eV is speculated to be due to chlorine. 96

Figure 4.9 77 K photoluminescence of ZnSe as a function of the growth temperature. The donor-bound exciton feature now at 2.790 eV red-shifted in energy due to the decrease in the ZnSe bandgap at 77 K. 98

Figure 4.10 Low temperature (10 K) PL illustrating the effect the surface stoichiometry during growth had on near-bandedge features of the photoluminescence. The near-bandedge PL of a film grown with a Se-rich surface (a) was dominated by a donor-bound exciton at 2.798 eV. The film grown with a Zn-rich surface stoichiometry (b) had a distinct free-exciton peak at 2.803 eV. 100

Figure 5.1 Two characteristics of Li which make it a less attractive *p*-type dopant compared to nitrogen. In (a), a SIMS depth profile illustrates how Li diffused into undoped regions during growth from the doped region indicated by the dotted rectangle [93]. The figure in (b) summarizes the net acceptor concentration as a function of the Li concentration. Arrows indicate ZnSe:Li layers which were fully depleted during C-V measurements. 104

Figure 5.2 Postulated stable structural states of neutral column V acceptors in ZnSe [96]. The four-fold coordinated P in (a) is the shallow effective-mass-like state. The more energetically favorable state (b), characterized by a broken P-Zn bond and subsequent lattice relaxation, has C_{3v} symmetry and a nearly planer sp^2 bonding geometry. 108

Figure 6.1 Schematic drawing of the Oxford free radical source. The capacitance matching network which makes electrical contact at the RF coupling (F) is not shown. 113

Figure 6.2 The 10 K photoluminescence intensity as a function of energy for nitrogen flows of: (a) no flow (undoped), (b) 5×10^{-6} Torr, (c) 1×10^{-5} Torr, and (d) 2×10^{-5} Torr, measured by the chamber ionization gauge. 117

Figure 6.3 SIMS depth profile of ZnSe #148. Depth profiles of the calibrated atomic concentrations of nitrogen, hydrogen, and chlorine are shown. The nitrogen concentration in this uniformly doped film was approximately 5×10^{18} atoms/cm^3. 119

Figure 6.4 Nitrogen concentration measured by SIMS as a function of the RF power supplied to the FRS. The background pressure due to the nitrogen flow was 2×10^{-5} Torr during doping. Data denoted by the solid points (•) are from films grown with a Zn-rich surface stoichiometry, while the circle (○) was from a Se-rich growth. 121

Figure 6.5 The 10 K photoluminescence from films grown with (a) a Se-rich , and (b) Zn-rich surface stoichiometry during growth. 122

Figure 6.6 SIMS depth profile of ZnSe #135. The structure consists of a doped ZnSe:N layer on an undoped ZnSe layer. The hydrogen and chlorine concentrations are observed to be higher in the nitrogen doped layer....... 126

Figure 7.1 Proposed configurations for N-H complex based on C_{3v} symmetry of N-H complex determined from Raman spectroscopy [46]. The configuration in (a) has hydrogen located in the bonding direction (bond centered position), while configuration (b) shows the anti-bonding location. 131

Figure 7.2 Model for the deep donor complex in ZnSe:N involving the next-nearest neighbor association of a selenium vacancy and nitrogen acceptor [116]. 134

Figure A.1 Geometry of RHEED configuration on the II-VI chamber. 141

Figure A.2 Illustrations of the origins of RHEED patterns [52]. The surface smoothness may be inferred from the particular RHEED pattern observed. Surface reconstructions are not shown in the figure................ 142

Figure B.1 Schematic drawing of double crystal x-ray diffractometer used to measure rocking curves. 144

Figure C.1 Schematic drawing of photoluminescence apparatus. The laser light path is indicated schematically by the lines. The labels M, L, BC, MS, and PMT correspond to a mirror, lens, beam chopper, mirror sliver, and photomultiplier tube, respectively. 147

List of Tables

Table 1.1 Some selected electrical and optical properties of ZnSe.......... 21

Table 1.2 Selected mechanical properties of ZnSe. 22

Table 3.1 Average bond strength of gaseous precursors [51].......... 42

Table 3.2 Summary of the growth parameter space investigated for MOMBE of ZnSe using DEZn and DESe source gases. The typical growth conditions are indicated in the final column. 43

Table 3.3 Summary of the MOMBE growth rates observed for different combinations of Zn and Se source materials.......... 47

Table 3.4 Comparison of observed growth rates for MOMBE using DEZn and DESe source gases as reported by our group and Hughes Research Laboratories [60,62]. The Hughes MOMBE experiments were performed using very similar growth conditions, yet they were able to achieve a high growth rate. 52

Table 3.5 Summary of the different laser wavelengths used for illumination during the laser-assisted MOMBE growth experiments.......... 55

Table 3.6 Growth conditions for the MOMBE and MBE laser-assisted growth experiments where the wavelength dependence of the growth rate enhancement or suppression is shown in Figure 3.6.......... 60

Table 3.7 The modification of the growth rate induced by laser illumination during MOMBE and MBE is summarized for the different combinations of sources used. 61

Table 3.8 Growth conditions of the films that were characterized by photoluminescence in Figures 3.12-14. 81

Table 4.1 The growth parameter space investigated for GSMBE of ZnSe using H_2Se and elemental Se sources. 85

Table 4.2 Growth conditions of the ZnSe films grown by GSMBE which produced the data shown in Figure 4.1.......... 87

Table 4.3 Percentage uncertainty in growth rate (ΔGR/GR) for different growth conditions. Entries are given as the percentage uncertainty in the growth rate caused by the uncertainty in the variables listed. Uncertainty calculations are carried out in Appendix D. 88

Table 4.4 Summary of the common growth conditions of the experiments from which Figure 4.3 was produced. 91

Table 4.5 Summary of the growth conditions of the films which are characterized by photoluminescence in Figures 4.6 and 4.7.. 97

Table 4.6 Summary of the effect the surface stoichiometry during growth had on the measured free electron concentrations. Hall effect measurements were performed to obtain the values. 101

Table 6.1 Summary of growth conditions and plasma source settings used in RF plasma doping study. The experiment number is entered in the matrix location corresponding to the conditions used....................................... 115

Table 6.2 Growth conditions of the films which have their photoluminescence shown in Figure 6.2. 118

Table 6.3 Summary of the C-V measurements and chemical concentrations of nitrogen and hydrogen measured by SIMS of the ZnSe:N films grown to date. An entry of 'flat-band' indicates the film was highly resistive resulting in a flat C-V trace. [N] and [H] are shown if available............. 125

Table C.1 Known luminescence transitions in unstrained ZnSe based on low temperature PL measurements. Values were based on data in Ref. [86] unless otherwise indicated.. 146

Table D.1 Percentage uncertainty in growth rate (ΔGR/GR) for different growth conditions. Entries are given as the percentage uncertainty in the growth rate caused by the uncertainty in the variable listed..................... 152

Acknowledgments

I would like to thank my thesis committee of Professors Kolodziejski, Kimerling, and Oliveria for their advice, insights, and guidance on directing my thesis research at MIT. I would also like to thank to Dr. Jurgen Michel who labored with me day and night in an attempt to get ODMR measurements of our ZnSe samples.

A special thanks is extended to Easen Ho, an individual of exceptional talents and abilities, who worked many long hours with me during the course of this research. Much of the experimental data was collected and analyzed with his help. During my stay in Boston, I valued his friendship the most.

I would also like to acknowledge past and present members of the research group who I have worked with over the years: Professor Gene Nanto, Steve Shephard, Philip Fisher, Jody House, Kan Lu, Jay Damask, Kuo-Yi Lim, Jack Shue, Sang Park, Ayca Yuksel, and David Lee. Contact with them and many other individuals at MIT has undoubtably enriched me in many ways.

I reserve the greatest thanks for my mother and father who have nutured me and provided financial support over the years.

Finally, I would like to say thank you to Mary Ellen, Leway, Eugene, Jennifer, and Roger who made my social life outside of MIT enjoyable.

Glossary of Acronyms Used in Thesis

ALE	Atomic Layer Epitaxy
CBE	Chemical Beam Epitaxy
CD-ROM	Compact Disc - Read Only Memory
C-V	Capacitance-Voltage
DCXRD	Double Crystal X-Ray Diffraction (Diffractometer)
DESe	Diethylselenium
DEZn	Diethylzinc
DI H_20	Deionized Water
DLD	Dark Line Defect
DMZn	Dimethylzinc
FWHM	Full Width at Half Maximum
FRS	Free Radical Source
GR	Growth Rate
LED	Light Emitting Diode
MBE	Molecular Beam Epitaxy
MEZn	Monoethylzinc
MFC	Mass Flow Controller
MOMBE	Metalorganic Molecular Beam Epitaxy
MQW	Multiple Quantum Well
NBE	Near-Bandedge
OMVPE	Organometallic Vapor Phase Epitaxy (also known as MOCVD)
PBN	Pyrolytic Boron Nitride
PL	Photoluminescence
QMS	Quadruple Mass Spectrometer
RF	Radio Frequency

RHEED	Reflection High-Energy Electron Diffraction
RTA	Rapid Thermal Anneal
sccm	standard cubic centimeter per minute
SEM	Scanning Electron Microscope (Microscopy)
SIMS	Secondary Ion Mass Spectroscopy
SQW-SCH	Single Quantum Well - Separate Confinement Heterostructure
TCA	Trichloroethane
TGA	Toxic Gas Absorber
TPD	Temperature Programmed Desorption
UHV	Ultra High Vacuum

Chapter 1

Introduction

ZnSe is an ionic wide bandgap II-VI semiconductor with a direct room temperature bandgap of 2.67 eV. The bandgap is sufficiently large to permit fabrication of injection devices that emit radiation in the blue and green regions of the visible spectrum. Semiconductor lasers are preferred in certain applications due to their compact size and relatively high quantum efficiency. ZnSe and related wide bandgap II-VI alloys are the subjects of increasing research worldwide as a potential material system to extend the operation of injection lasers into the blue region of the visible spectrum.

1.1 Background

1.1.1 Progress Toward Blue-Green Injection Lasers

ZnSe has been investigated as a potential light emitter in the blue region of the visible spectrum for over 30 years. The 2.67 eV room temperature direct energy gap, which corresponds to a bandgap photon with a wavelength of 464 nm, makes ZnSe an attractive semiconductor for a blue diode. In spite of considerable research effort, a light emitting device fabricated in ZnSe was not produced until 1988, when *p-n* junction light emitting diodes (LEDs) using Li as the *p*-type dopant were first reported [1 ,2]. The first ZnSe-based laser diode was reported in 1991 and this device utilized nitrogen as the acceptor impurity [3]. Within a year of the first laser diode announcement, several other research groups reported blue-green LEDs and laser diodes which used nitrogen as the *p*-type dopant [4 -8]. These advances in device fabrication were possible due to a milestone

breakthrough in doping ZnSe *p*-type by employing a nitrogen plasma source during molecular beam epitaxy [9 ,10].

Stutius [11] was one of the first to suggest that N would be the most promising element for an acceptor in ZnSe based on studies of acceptor atoms incorporated during organometallic vapor phase epitaxy (OMVPE). Theoretical studies by Chadi and Chang [12] had predicted that nitrogen would be the best candidate as a group V substitutional acceptor atom on the Se site. Unfortunately, molecular nitrogen has a very low sticking coefficient when used as a gaseous dopant during epitaxial growth [13], which limited the nitrogen incorporation to the 10^{15} - 10^{16} atoms/cm^3 range. Attempts to introduce nitrogen acceptors through low energy ion implantation were unsuccessful [14], with the films being highly resistive (> 10^4 Ω cm) which might have been a result of implantation damage. The key insight was that a plasma could produce excited species from molecular N_2 with much higher sticking coefficients in the gaseous phase. It has now been demonstrated that nitrogen can be incorporated in significant concentrations (> 10^{19} atoms/cm^{-3}) producing free hole concentrations as high as 10^{18} *h*/cm^{-3} using plasma sources. Studies of the optical discharge of nitrogen plasma sources suggest that atomic nitrogen is the 'active' species which after incorporation produces the useful concentrations of free holes [15 ,16]. The sticking coefficient of atomic nitrogen to the ZnSe surface may be higher due to dangling *p*-orbital bonds enhancing the chemisorption.

An alternate approach to achieve *p*-type ZnSe is being investigated for metalorganic molecular beam epitaxy (MOMBE) of ZnSe. Researchers at Hitachi Central Research Laboratories have reported the achievement of low resistivity *p*-type ZnSe grown by MOMBE where ammonia was the dopant [17]. Using this approach to nitrogen doping, they have reported the fabrication of LEDs with low turn-on voltages for devices employing a simple Au/*p*-ZnSe contact [18].

1.1.2 (Zn,Mg)(S,Se) and (Zn,Cd)(S,Se) Material Systems

Nitrogen plasma sources have been used to produce *p*-type epilayers in II-VI ternary and quaternary alloys of the (Zn,Cd)(S,Se) [3-6] and (Zn,Mg)(S,Se) [7,8] material systems. This is fortuitous since alloying Mg or S into ZnSe increases the energy gap compared to the compound ZnSe, and increases (Mg) or decreases (S) the lattice parameter; the composition of the quaternary (Zn,Mg)(S,Se) can be tailored to a specific bandgap energy while maintaining the lattice match over a range of lattice constants. Alloying Cd into ZnSe lowers the bandgap energy moving the emission to the green region of the spectrum and increases the lattice constant.

Figure 1.1 is a diagram showing the bandgap energy E_g versus the lattice constant a_o of II-VI compound semiconductors which are being investigated for injection devices in the visible. Included in the figure are III-V compounds which alone or as alloys are used as substrate materials for II-VI growth. The values of the elements Si and Ge are

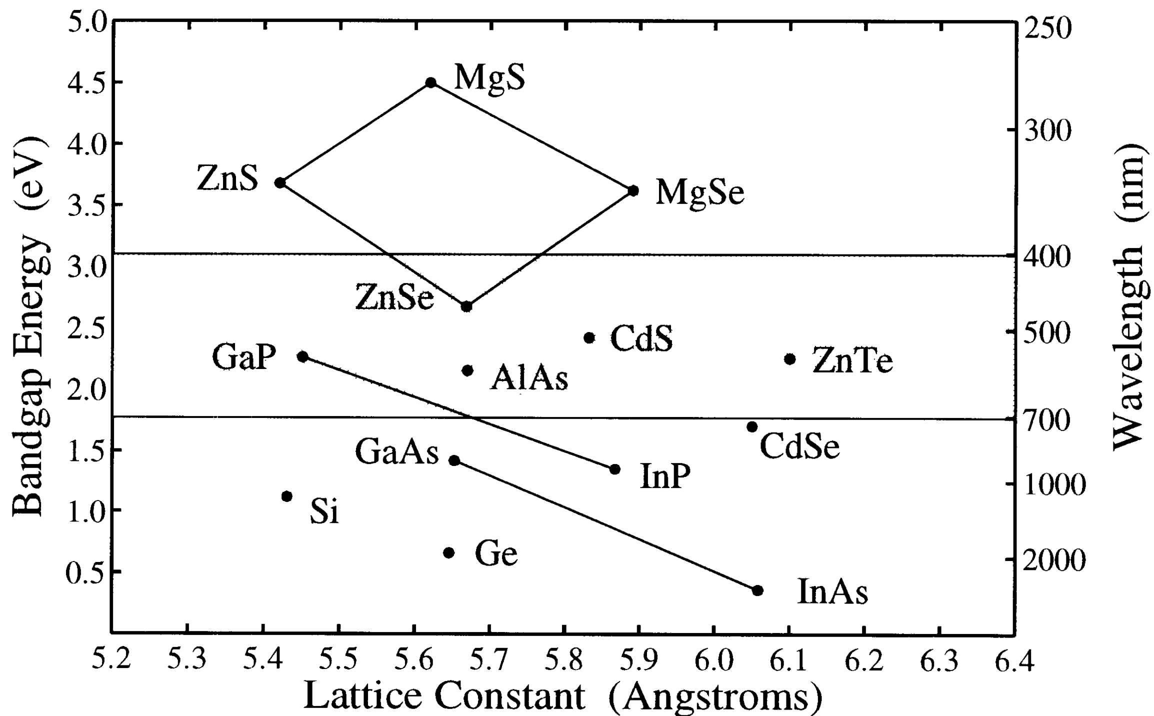

Figure 1.1 Bandgap energy versus lattice constant diagram of important compounds in current II-VI light emitting device research.

provided as a reference. The diamond shaped region connects the ternary alloys that define the quaternary (Zn,Mg)(S,Se). Also shown are lines representing the ternaries of (In,Ga)As and (In,Ga)P which can be lattice matched to a range of II-VI alloys, and a shaded band (between 400 and 700 nm) corresponding to the approximate energies of the visible spectrum. The close lattice parameter match of Ge to ZnSe has encouraged efforts in heteroepitaxy of ZnSe on Ge [19], but the non-polar nature of the substrate results in the formation of anti-phase defects at the interface and misorientation of the layer with respect to the substrate [20].

Heterostructure device design has been an integral factor in achieving light emission in II-VI devices. Judicious selection of heterointerface materials enhances the electrical and optical confinement, thus lowering the threshold current density for operation. The first ZnSe laser diode [3] was a separate confinement heterostructure, single quantum well device (SCH-SQW) consisting of a ZnSe-$ZnS_{0.07}Se_{0.93}$ waveguide, and a $Cd_{0.2}Zn_{0.8}Se$ quantum well between ZnSe barriers. In order to obtain shorter emission wavelengths, other investigators are fabricating SCH-SQW and multiple quantum well (MQW) devices using (Zn,Mg)(S,Se) cladding layers, and ZnSe quantum wells between Zn(S,Se) barriers [7,8]. As of this writing, Sony Corporation researchers have reported the shortest wavelength for an injection laser at 447 nm [7].

1.1.3 Material Properties of ZnSe

ZnSe is the base material to which other elements are alloyed to form ternary and quaternary layers in fabricating blue-green light emitting heterostructures. Some material constants of ZnSe are presented in this section to provide the reader with background on the material characteristics of this increasingly important compound.

ZnSe crystallizes in the zincblende lattice structure with the zinc and selenium atoms located on separate face-centered cubic sublattices. Due to the large difference in the

electronegativity of the Zn and Se atoms, the Zn-Se bond is more ionic than covalent in character. It is calculated that the bonding of Zn and Se atoms in the tetrahedral environment of the zincblende lattice has a 63% ionic component [21]. The polar nature of ZnSe implies that electrons are localized about the Se anion. In terms of band structure, the tighter binding results in relatively large electron and hole effective masses. The interest in ZnSe is due to its large direct bandgap (2.67 eV at room temperature) and large non-linear optical coefficient, due in part, to its non-centrosymmetric crystal structure [22].

Table 1.1 gives values for some electrical and optical properties of ZnSe. An often quoted nonlinear figure of merit is the product $n^3(r_{lk}/2)$, where n is the index of refraction at the wavelength of interest, and r_{lk} is an element of the electro-optic tensor for the material. The figure of merit for ZnSe (1.9×10^{-9} cm/V, at 633 nm) compares favorably to GaAs (2.6×10^{-9} cm/V, at 900 nm), a semiconductor often used to fabricate nonlinear

Table 1.1 Some selected electrical and optical properties of ZnSe.

Property		Symbol	Value	Units	Ref.
Energy Gap	(R.T.)	E_g	2.67	eV	[23]
	(4 K)		2.822	eV	[24]
$\partial E_g/\partial T$			7.2	10^{-4} eV/K	[23]
Spin-orbit Splitting		Δ_{so}	0.45	eV	[23]
Electron Affinity		χ	4.1	eV	[25]
Electron Effective Mass		m_e^*	0.17	m_o	[23]
Hole Effective Mass		m_h^*	0.6	m_o	[23]
Electron Mobility	(R.T.)	μ_e	600	$cm^2/V \cdot cm$	[25]
Hole Mobility	(*hh*, R.T.)	μ_{hh}	~30	$cm^2/V \cdot cm$	[26]
Free-exciton Binding Energy	(*lh*)		21	meV	[27]
LO Phonon Energy		ω_{LO}	31.9	meV	[28]
Dielectric Constant	(Static)	$\varepsilon_r(0)$	9.1	$\varepsilon_r(\varepsilon_o)$	[22]
Index of Refraction	(458 nm)	n	2.66		[22]
Electro-optic Coefficient		r_{41}	2.0	10^{-10} cm/V	[22]

Table 1.2 Selected mechanical properties of ZnSe.

Property	Symbol	Value	Units	Ref.
Lattice Constant	a_o	5.6686	Å	[25]
Expansion Coefficient	α	7.0	10^{-6} /°C	[23]
Melting Point	M_p	1520	°C	[23]
Thermal Conductivity	K	0.19	W/cm·K	[23]
Elastic Constants	C_{11}	8.59	10^{10} dyne/cm^2	[30]
	C_{12}	5.06	10^{10} dyne/cm^2	[30]

devices. ZnSe has the advantage of being an extremely low loss waveguide at III-V device wavelengths, and can be used as a waveguide at many visible laser wavelengths. To demonstrate these advantages, a rib-waveguide optical phase modulator has recently been demonstrated in the ZnSe-Zn(S,Se) material system [29].

Knowledge of the mechanical properties of ZnSe is essential to accurately interpret characterization data in certain measurements such as photoluminescence (PL) and x-ray diffraction. As an example, ZnSe PL can exhibit positive or negative energy shifts in the excitonic features depending on the nature of the strain within the heteroepitaxial film. Understanding how particular growth conditions interact with the mechanical properties of the film and substrate to introduce strain is critical in evaluating energy values in PL spectra, and angular separations in x-ray diffraction measurements. Values of selected mechanical properties of ZnSe are given in Table 1.2.

1.1.4 Technological Applications

A promising application for blue laser diodes is in CD-ROM and magneto-optical recording. The areal density of recorded information is inversely proportional to the square of the wavelength, being limited by the minimum diffracted spot size. The GaAs/AlGaAs double heterostructure lasers currently in use in CD-ROM equipment have a near infrared wavelength of ≈ 870 nm. A laser operating at 440 nm could read

approximately 4 times the recorded density than is possible with an AlGaAs laser. Another requirement for the lasers employed in commercial CD-ROM equipment is compact size. The laser is integrated into an optics assembly for tracking and reading the data. The whole assembly must be compact so that electro-mechanical actuators can quickly and accurately position the optics assembly over the recorded media. Frequency doubled AlGaAs laser diodes which also emit blue radiation through up-conversion in a non-linear crystal [31] are too large to be used in current generation CD-ROM and magneto-optic equipment. Frequency doubled AlGaAs lasers will likely be limited to high-end systems where more expensive beam steering approaches to tracking and reading the information are less of a price issue.

A compact semiconductor laser in the blue could also be used in low-power applications where long coherence lengths are not required. Most argon and krypton ion lasers require special electrical and cooling facilities and are physically large in size. Additionally, the plasma tube must be replaced at substantial cost every five to ten years. (Zn,Mg)(S,Se) and (Zn,Cd)(S,Se) based injection lasers have the potential to span almost the entire range of the emission lines produced by the argon and krypton lasers. If high powers are needed, arrays of II-VI lasers could be built.

A promising application being investigated at North Carolina State University (NCSU) is to build bright emissive LEDs [32]. The NCSU researchers are using (Zn,Cd)(S,Se) and Zn(Te,S,Se) active layer materials for blue and green LED applications, respectively. The performance of the blue LEDs are better than commercially available SiC LEDs. The green LEDs are brighter and have a narrower emission bandwidth compared to GaP devices on the market. The challenge they are now addressing is increasing the lifetime beyond the several hundred hours currently obtained [32].

1.1.5 Central Materials Issues

The aforementioned applications will require that the device lifetimes be dramatically increased. As of this writing, the room temperature operational lifetime of ZnSe based laser diodes has been reported to be a few minutes to one hour [33]; this number needs to be increased by approximately five orders of magnitude for practical commercial devices. Light emitting diodes which are less demanding structures in terms of materials quality have yet to achieve lifetimes beyond a few hundred hours [32]. This technological hurdle may be possible to clear if the history of III-V lasers can be repeated. The earliest III-V lasers had equally short lifetimes, but a thorough study of the mechanisms which led to device failure enabled preventive solutions to be devised which eventually resulted in devices with lifetimes in excess of 10^5 hours.

ZnSe and other wide bandgap II-VI compounds present unique problems from a materials standpoint in eliminating or suppressing defect generation mechanisms. The low energies required to generate point defects and the large bandgap of the materials make them susceptible to electronically-enhanced defect reactions [34] resulting from nonradiative electron-hole recombination events. It was proposed that dark line defects (DLDs), which are nonradiative recombination centers which have been observed in the active region of III-V devices, are formed by the climb of dislocation networks by a mechanism induced by the operation of the device [35 ,36]. Recently, a study of the degradation of the active region of II-VI blue-green light emitters has revealed the rapid production and propagation of crystalline defects analogous to the DLD in III-V devices [33]; it was observed that the degradation that quenched the light emission nucleated at pre-existing defects near heterointerfaces. To reduce the probability of DLD formation, it is necessary to minimize the potential DLD nucleation sites such as threading dislocations and stress fields near the interfaces. The II-VI devices that have been described required heterointerfaces to enhance their performance. Therefore, precise control of the ternary

and quaternary alloy compositions are critical to minimize the strain that can develop at heterointerfaces.

1.2 Dissertation Overview

This thesis investigated novel epitaxial methods to the growth of ZnSe. The early chapters will describe and present the results of metalorganic molecular beam epitaxy (MOMBE) and gas source molecular beam epitaxy (GSMBE) growth of ZnSe. If gaseous source epitaxy of ZnSe is to be a viable method, it will be necessary to demonstrate that ZnSe can be doped *p*-type using these techniques. The initial work investigating the potential of using a nitrogen plasma source to dope ZnSe *p*-type is presented. The consequences of hydrogen contamination of ZnSe:N films resulting from the gaseous growth process are discussed. The non-ideal behavior of nitrogen as a dopant is becoming an area of increasing concern. The nature of this non-ideal behavior is discussed and recent theoretical explanations for the observed phenomena are presented.

1.2.1 Epitaxy System and Experimental Procedures

The second chapter contains a description of the II-VI epitaxy system in the Chemical Beam Epitaxy (CBE) Laboratory. The layout of the interconnected ultra high vacuum (UHV) systems and more detailed drawings of the II-VI reactor are shown. The special features for using and handling gases are described. The second part of the chapter is a presentation of the standard experimental procedures for preparing a sample for growth. The procedures covered include: preparation of the sample holder and the GaAs wafer, the method used to calibrate the temperature of the substrate in the vacuum system, and the remaining actions necessary prior to commencement of growth.

1.2.2 MOMBE and GSMBE

Two variations of molecular beam epitaxy (MBE) known as metalorganic molecular beam epitaxy (MOMBE) and gas source molecular beam epitaxy (GSMBE) were

investigated. These techniques are best described as hybrid technologies between MBE and metalorganic vapor phase epitaxy (OMVPE). The raison d'être for using gaseous sources is an attempt to overcome the difficulties in reproducibly controlling the composition of ternary and quaternary alloys. The constituent elements of II-VI compounds have higher vapor pressures than most III-V semiconductors which makes it difficult to maintain a stable flux throughout growth when effusion ovens are used. GSMBE has been demonstrated to be an effective epitaxial growth method to reproducibly control the composition of the quaternary (In,Ga)(As,P) which contains the high vapor pressure elements As and P [37]. Growth of the II-VI quaternary (Zn,Cd)(S,Se) by MOMBE has recently been demonstrated [38]. Chapter 3 is concerned with MOMBE growth of ZnSe where the effects of laser irradiation were simultaneously investigated during growth. A major observation of this research was that light could alter the growth rate of the film through surface interactions of photo-generated electrons and/or holes with adsorbed species [39 -43]. Chapter 4 discusses the current research in GSMBE of ZnSe using Zn and hydrogen selenide [44].

1.2.3 Acceptor Compensation in ZnSe

Chapter 5 addresses the past difficulties in attaining conductive *p*-ZnSe and reviews proposed explanations for acceptor compensation in the material. Contrary to the hopes of the ZnSe research community, nitrogen is not behaving as an ideal acceptor in ZnSe. The behavior that has attracted the most attention is an apparent solubility limit of nitrogen which prevents the attainment of free hole concentrations sufficient to tunnel across the Schottky barrier formed with common contact metals.

1.2.4 ZnSe:N

A nitrogen plasma source has been used to incorporate nitrogen into GSMBE grown ZnSe:N in concentrations as high as $6x10^{18}$ N atoms/cm^3, as measured by secondary ion

mass spectroscopy (SIMS). Chapter 6 discusses the characteristics of the ZnSe:N produced using the RF plasma source. Most ZnSe:N films have been highly resistive giving flat-band capacitance-voltage traces. A puzzle in ZnSe research of recent years has been that only MBE grown nitrogen doped epilayers have yielded low resistivity *p*-ZnSe. Recent characterization of our GSMBE films, and films other researchers have grown by OMVPE, suggests that hydrogen passivation is the most probable cause for the low degree of acceptor activation [45 ,46] of ZnSe:N grown by these methods. SIMS depth profile analysis of our films has revealed that hydrogen is incorporating at concentrations equal to or greater than the [N], and preferentially in ZnSe layers with nitrogen. Chapter 7 reviews some of the literature on hydrogenation of semiconductors and relates what is known about hydrogenation to our ZnSe:N epilayers. Recently proposed models for the origin of nitrogen acceptor compensation at high doping levels observed in MBE grown ZnSe:N are also discussed in Chapter 7.

1.2.5 Conclusions and Future Work

The final chapter summarizes the major results of the thesis research. Some comparison of the gaseous techniques of MOMBE and GSMBE to the established method of MBE are presented. Recommendations are made for future experiments, and technological hurdles necessary to be overcome are identified.

Chapter 2

Epitaxy System and Experimental Procedures

One thrust of the research effort of the chemical beam epitaxy (CBE) laboratory at MIT is to investigate alternate epitaxy methods for the growth of ZnSe. In pursuit of this goal, two gas source MBE systems are being used within the laboratory. To enable the use of metalorganic and hydride gas sources, a greatly enhanced pumping capability is a notable feature of these systems. One reactor which will be described in detail is dedicated to the growth of II-VI thin films. A second GSMBE system (Riber CBE 32) is used to produce III-V epitaxial layers for II-VI heteroepitaxy, and to fabricate novel III-V devices based on the (In,Ga)(As,P) materials system.

Figure 2.1 is a drawing of the layout of the interconnected ultra high vacuum (UHV) chambers within the laboratory. Separate growth chambers are utilized to prevent cross-contamination of II-VI films by III-V elements and visa versa. An UHV transfer chamber containing a mechanical transfer mechanism connects the other chambers, and permits *in vacuo* movement of a sample between chambers, which greatly reduces the amount of background gas adsorption on a sample surface. The buffer chamber between the III-V reactor and transfer chamber is designed to facilitate the transfer of a wafer between the III-V and II-VI epitaxy chambers for subsequent heteroepitaxy. Hardware in the buffer chamber (not yet available when this thesis was written) is designed to mate a II-VI sample holder to a modified Riber sample block. Separate chambers for introducing the sample into vacuum (load lock), and for analyzing and evaporating metals onto the samples, are connected to the transfer system.

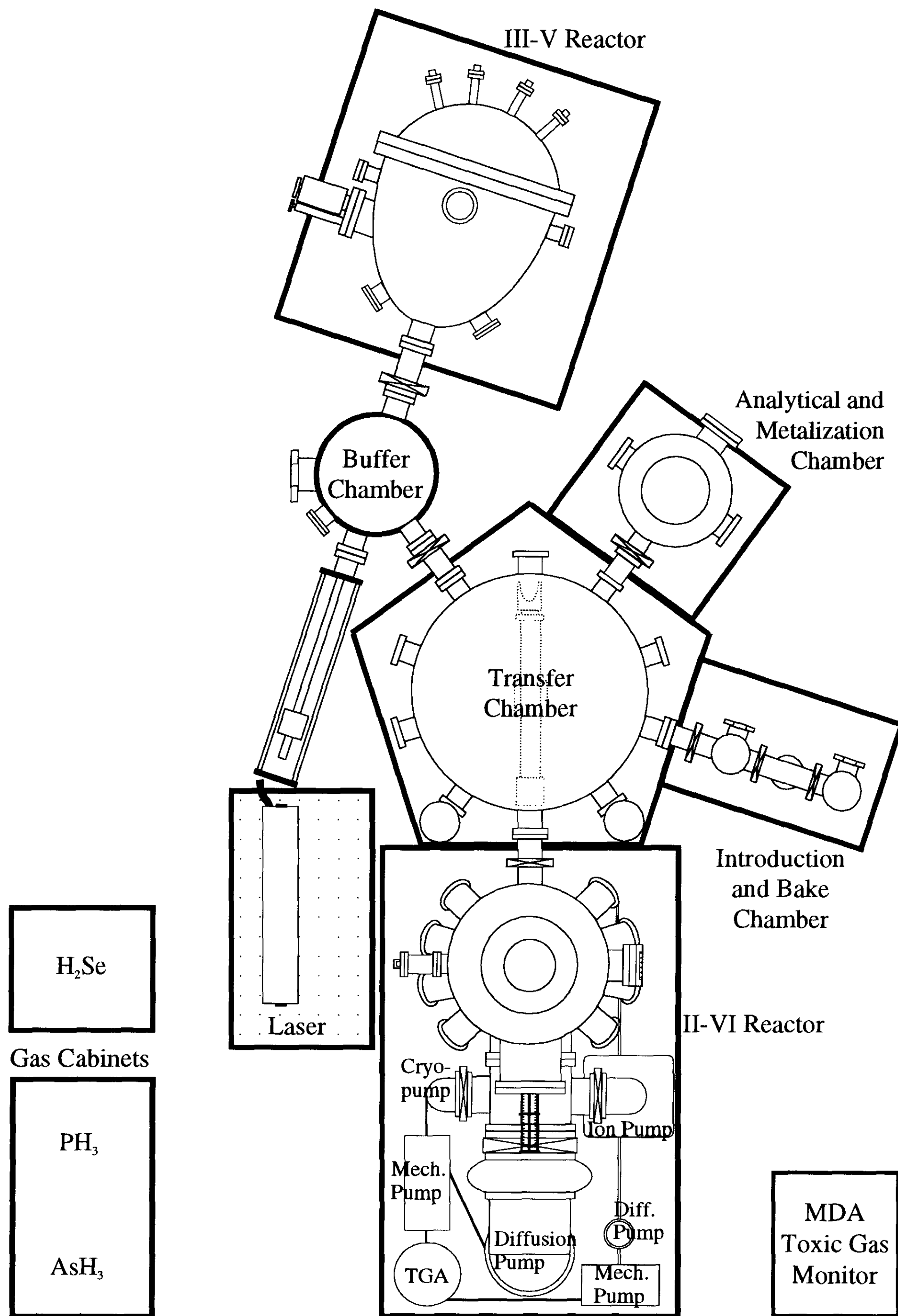

Figure 2.1 Diagram illustrating the layout of the interconnected UHV epitaxy systems within the CBE laboratory. The UHV chambers and the major subsystems are identified by name.

2.1 II-VI Chamber Description

The II-VI reactor is a custom-built MBE chamber with the capability to pump large gas loads typically generated in MOMBE or GSMBE. To pump gas flows in the 10 standard cubic centimeter per minute (sccm) range, a 2300 *l*/s diffusion pump and a liquid nitrogen cryotrap are employed during growth. When the reactor is idle, the chamber is maintained near UHV pressures by a 1500 *l*/s cryopump and a 440 *l*/s ion pump. Figure 2.2 shows schematic views of the growth chamber indicating the positions of the solid source effusion ovens, gas 'crackers'/injectors, substrate, viewports and other hardware. The distance from the exit apertures of the effusion ovens and crackers to the center of the

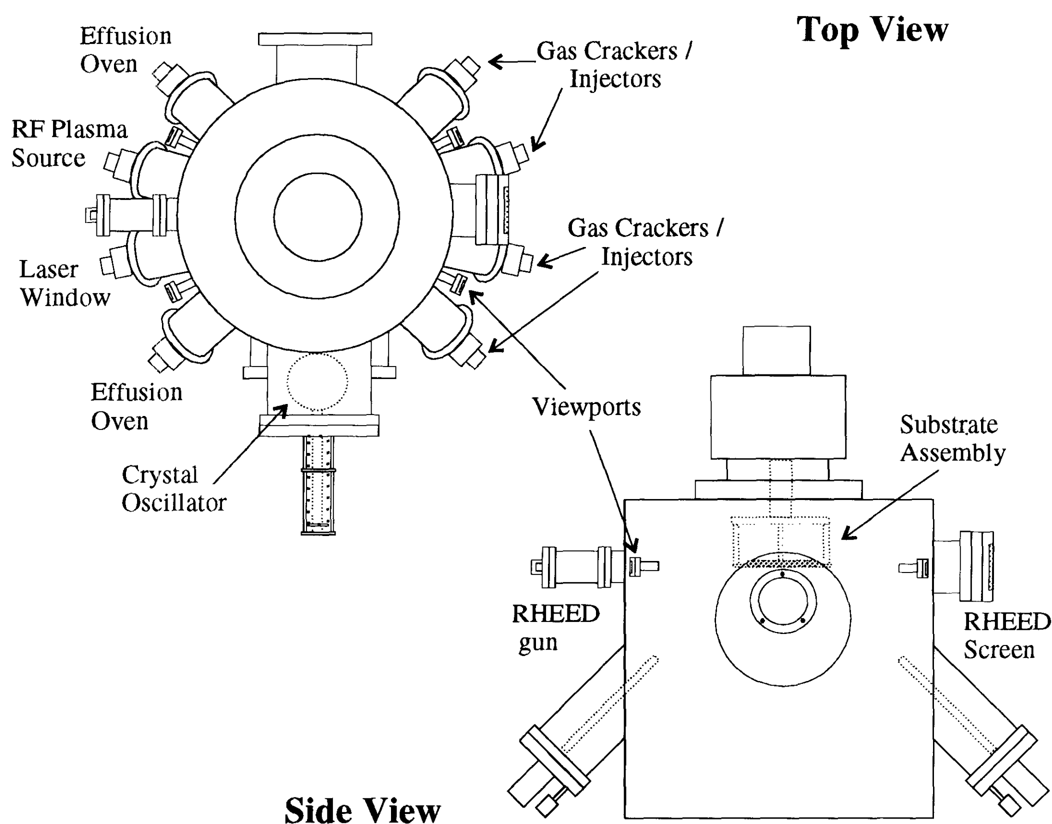

Figure 2.2 Top and side view drawings of the II-VI epitaxy chamber which illustrate the geometry of the chamber. The locations of the sources and some key analytical equipment are also shown.

substrate is approximately 21 cm. On one side of the chamber is the vent-run gas manifold supplying four gas crackers: two high temperature crackers for column V and VI gaseous sources, and two low temperature crackers for the column II and III gas sources. The opposite side of the chamber has four 6" source flanges where the effusion ovens, the RF plasma source, and a viewport for laser-assisted epitaxy are placed. The configuration for H_2Se GSMBE is to use Zn and $ZnCl_2$ effusion ovens, the RF plasma source, and a laser viewport window. The eight source flanges are oriented upward making a 45° angle with the reactor wall, and are positioned such that a straight line exists from the center of each flange to the center of the substrate. The substrate is mounted horizontally with the sample normal pointing downwards. 360 degrees of rotation is available in the substrate assembly to increase the uniformity in film thickness and composition. Four window viewports located at the elevation of the substrate assembly provide views into the chamber to assist in sample transfers. Two additional windows are positioned to view the substrate and are normally equipped with an optical pyrometer and a CCD camera.

The effusion ovens and gas crackers were supplied by EPI of St. Paul, Minnesota. The effusion ovens are standard design source and doping Knudsen cells. The gas crackers are baffled gas feed tubes surrounded by a heating filament, which extend into the reactor. The low and high temperature gas crackers are of different design. The material in the cracking zone of the low temperature cracker is tantalum. A tantalum diffuser plate on the end of the parabolic cracking zone was removed on the group II cracker to improve the collimation of the gas beam at the substrate. The high temperature cracker shown in detail in Figure 2.3 is of composite material construction. The gas feed tube is pyrolytic boron nitride (PBN) which is surrounded by a Ta:PBN filament assembly. A removable Ta baffle insert provides catalytic surfaces and increases the gas collisions with the heated PBN walls.

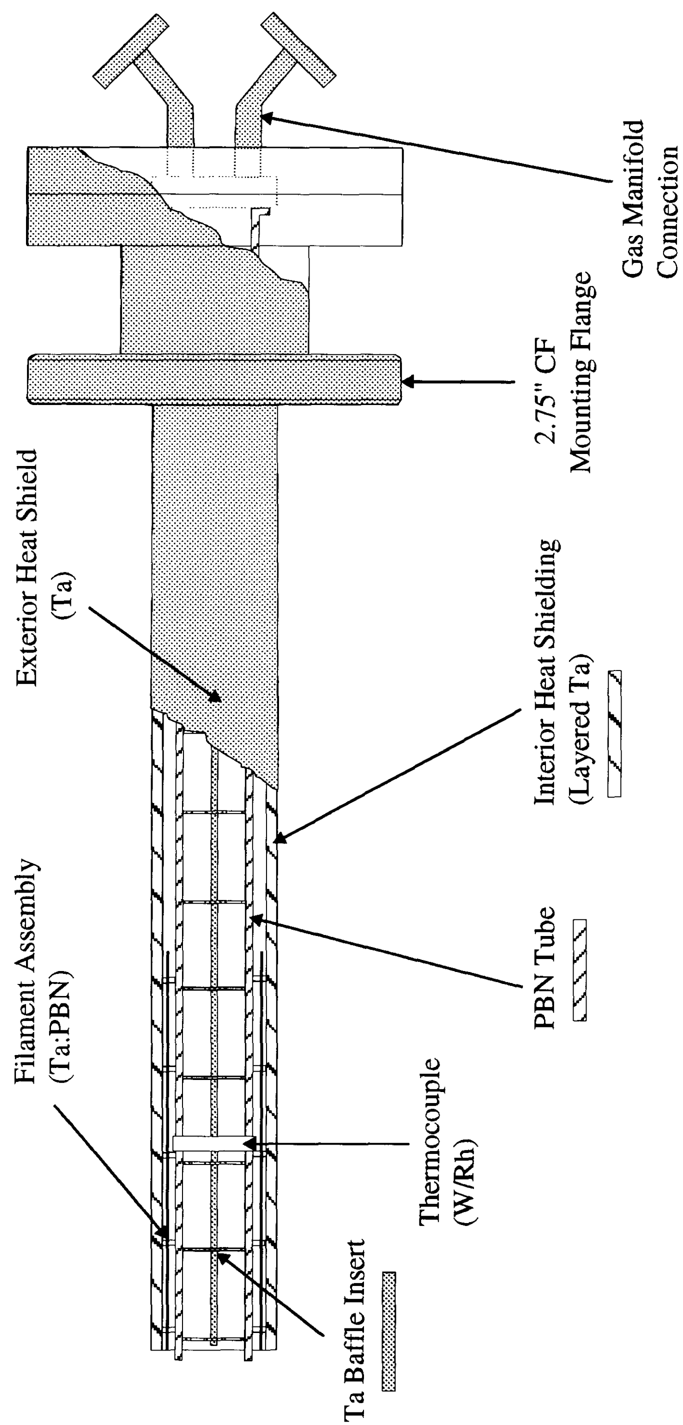

Figure 2.3 Detailed view of the high temperature gas cracker. The gas tube wall is PBN and the baffle insert is made of Ta.

2.2 Gas Delivery System

Growth of certain types of device structures such as quantum wells require that gas flows be switched on and off rapidly to achieve abrupt interfaces. To reduce pressure transients that decrease the abruptness of interfaces, a well designed vent-run gas switching network is needed near the entrance to the gas crackers/injectors. A vent-run configuration is a gas switching arrangement that either directs the gas into the reactor (run), or into a pumped vent line (vent) as illustrated in Figure 2.4. This arrangement insures that the gas flow established by a mass flow controller (MFC) upstream of the injector does not experience pressure buildups due to a closed valve. The metalorganic gases are metered into the reactor using vapor phase mass flow controllers manufactured by MKS (model 1150A). These vapor phase MFCs do not require a carrier gas, are calibrated for flows up to 5 sccm, and operate with as little as a few Torr of inlet pressure. The hydride gas MFCs are industry standard 0-10 sccm controllers (MKS 1461A).

Hydride gases are acutely toxic and require special equipment to be handled safely. The hydride gases in the laboratory are stored in Semi-Gas cabinets which contain five-valve gas purge manifolds. The gas purge manifold allows the tubing connected to the hydride cylinder to be thoroughly purged before changing the cylinder. The hydride lines that exit the Semi-Gas cabinets are coaxial; the gas line is surrounded by an outer tube that terminates near a hydride gas detection point. Constant monitoring for hydride gas leaks is performed by three MDA toxic gas detection systems which provide redundancy in coverage. These monitors are capable of detecting a hydride gas at concentrations that are far below levels that will cause harm. Alarms in the laboratory are activated if one of the monitors detects a hydride concentration above predetermined safe values.

The exhausted gas from the reactor has residual hydride and metalorganic gases removed by a toxic gas absorber (TGA). The TGA consists of an activated charcoal resin bed which reacts with the hydride and metalorganic gases as they percolate through. The

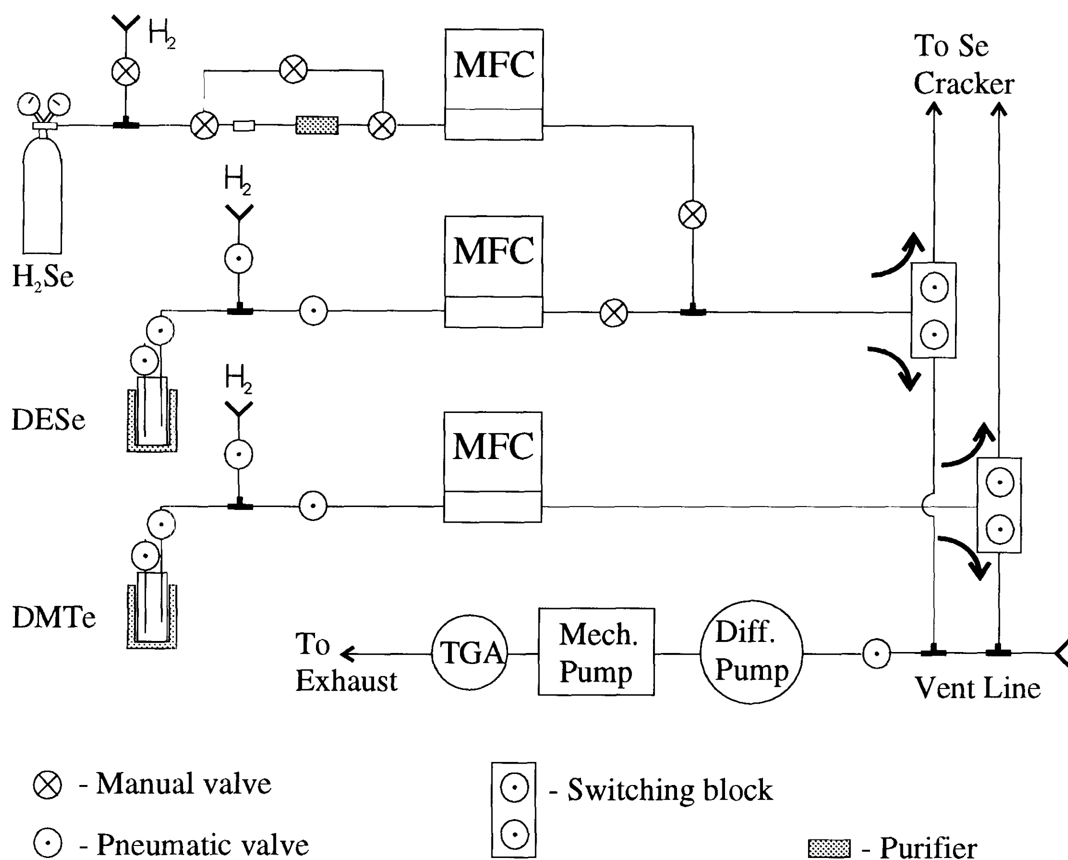

Figure 2.4 Representative gas routing arrangement on II-VI reactor. A vent-run configuration is used near the cracker switching block to suppress gas flow transients.

effluent of the TGA which empties into the room exhaust is monitored by an MDA process point to verify proper operation.

2.3 Sample Preparation

2.3.1 Sample Holder

GaAs wafers were mounted on a two piece refractory metal sample holder. The outer piece which was either molybdenum or niobium, was a rim which supported an inner disk, and had a ring around the periphery to allow a two tine fork to be inserted to lift and transport the sample holder. The inner piece was a molybdenum disk which rested on an

inner lip of the outer rim. A 50 mm GaAs wafer could be placed directly in the outer rim where the center disk normally was placed, but in most experiments a partial GaAs wafer was mounted to the center disk using In solder. Prior to use, the two pieces of the sample holder were degreased (to be described in the next section) and etched in a diluted solution of 20-30% HNO_3 acid. The pieces were next immersed in undiluted HCl acid to remove the oxide formed, and then thoroughly rinsed in deionized water (DI H_2O). To remove acid that might have collected in surface irregularities and at grain boundaries, the sample holder was vacuum outgassed for 1 hour in the introduction chamber bake station at a thermocouple setting of 700 °C.

2.3.2 Wafer Preparation

ZnSe was grown heteroepitaxially on GaAs substrates. Growth on all three substrate conduction types of GaAs were investigated: semi-insulating with a resistivity > 10^7 Ω cm, *n*-type wafers with [Si] ~ 10^{18} atoms/cm^{-3}, and *p*-type substrates with [Zn] or [B] on the order of 10^{18} atoms/cm^{-3}. The wafers were purchased from either the Sumitomo Electric Company or American Crystal Technology. A wafer In soldered to a molybdenum disk was normally cleaved into quarter pieces or smaller sizes. Prior to mounting, the wafer piece was degreased and then etched to form a new 'clean' oxide. The degrease steps were as follows: (1) wafer was boiled twice in trichloroethane (TCA); (2) TCA was removed by rinsing with acetone and shaking in an ultrasonic bath cleaner; (3) acetone was rinsed off by immersing wafer in methonal and placing in ultrasonic cleaner; (4) wafer was thoroughly rinsed in DI H_2O and dried with N_2. The wafers were purchased as epi-ready out of the packaging, but the wafers were etched to form a new clean oxide. The wafer etch was a 5:1:1 solution of H_2SO_4:H_2O_2:DI H_2O mixed approximately 1 minute prior to dipping a wafer. Wafers were etched for 90 seconds and then thoroughly rinsed under flowing DI H_2O and dried before mounting on the molybdenum disk. A layered

eutectic was also degreased and mounted alongside the GaAs wafer and was used for temperature calibration.

2.4 Temperature Calibration

ZnSe was usually grown around 320 °C. As is common in MBE systems, the substrate was heated radiatively from the backside by a heating element located behind the sample holder. The substrate thermal couple was located in a black body cavity formed by the heater, the heat shielding, and the substrate holder. The thermocouple did not make physical contact with the sample holder. The energy radiated per unit time per unit area (u) by a blackbody, which the carbon filament approximated (adjusted for its emissivity), is described by the Stefan-Boltzmann law [47],

$$u = \frac{2\pi^5 (kT)^4}{15h^3c^2} \equiv \sigma T^4 , \qquad \text{(Eq. 2.1)}$$

where σ is defined as the Stefan-Boltzmann constant. Since the Stefan-Boltzmann blackbody emissive power varies as T^4, heating and cooling of the sample holder required longer periods of time compared to III-V growth. A 20 °C shift in the growth temperature can have a significant impact on the characteristics of ZnSe, so temperature calibration was an extremely important step.

An absolute temperature reference was required for each run to insure repeatability. A layered structure composed of metals which form a eutectic system was used. A layered eutectic was produced by depositing several hundred angstroms of one metal of the alloy on a substrate of the other metal. When the temperature was raised to the eutectic temperature the alloy phase formed. The gold-germanium alloy has a eutectic temperature of 356 °C which was close to ZnSe growth temperatures. A layered eutectic of ~ 500 Å of Au on a Ge substrate was used to identify a known temperature within the vacuum. Visual observation of the phase change was possible due to the change in color from gold

to a dull silver, and the surface texture became rougher. An alternate approach is to view the eutectic with an optical pyrometer and observe where the temperature changes suddenly due to the change in emissivity when the alloy phase forms. Once the absolute temperature of 356 °C was established as described above, the emissivity of the optical pyrometer was set so the pyrometer would read 356 °C at the observed eutectic phase change. The pyrometer was the calibrated temperature reference used before and during growth.

2.5 Other Growth Procedures

Prior to growth, the GaAs oxide was removed by elevating the substrate temperature to a temperature near 600 °C, but below the congruent sublimation temperature of GaAs of ~ 640 °C. Reflection high-energy electron diffraction (RHEED) images were observed to detect the appearance of lattice diffraction lines and surface reconstructions which indicated the removal of the oxide. After the oxide was removed, the substrate temperature was set to the growth temperature and allowed to cool for at least 1 hour, so the substrate could equilibrate to the lower growth temperature.

During growth, the surface of the sample holder became coated by Zn and Se thin films. As a result, the emissivity of the sample holder increased which altered the relationship between the substrate thermocouple and the actual wafer temperature. To get accurate temperature readings during growth, the optical pyrometer was aimed to measure the temperature of the In soldering the wafer to the sample holder. The GaAs substrate and ZnSe thin film were transparent to the infrared wavelengths used by the optical pyrometer to measure the temperature. By monitoring the temperature of the In solder protected by the GaAs substrate, it was possible to obtain calibrated temperature measurements as growth proceeded.

Chapter 3

Metalorganic Molecular Beam Epitaxy of ZnSe

Metalorganic molecular beam epitaxy or chemical beam epitaxy, which utilize either metalorganic gases (MOMBE), or metalorganic and hydride gases (CBE) as the source materials, eliminate many of the difficulties associated with controlling the fluxes of high vapor pressure elements which are common in II-VI epitaxy. The gases are introduced into the epitaxy chamber through gas cracking injectors in carefully metered flows established by mass flow controllers (MFCs). The relative distribution of gaseous species produced during cracking remains constant as long as the cracker temperature and gas flows are unchanged. The cracker temperatures and MFCs are regulated by proportional, differential, integral (PID) controllers to an accuracy of 1 °C or 1% of flow, respectively.

3.1 Instability in MBE Source Fluxes

The stability of metered gas flows and, hence, the flux, can be contrasted with our experience using Knudsen cells to generate a flux of zinc or selenium. The flux emitted by an effusion oven (Knudsen cell) is strongly dependent on the temperature and the exposed surface area to vacuum. Zinc and selenium are relatively high vapor pressure elements which are present in the vacuum. The pressure over a solid of pure material in vacuum can be described by an expression of the form,

$$\log(p[Torr]) = a - \frac{b}{T}, \qquad \text{(Eq. 3.1)}$$

where a and b are constants that can be derived from data in vacuum reference texts [48]. The Knudsen equation for evaporation from an isothermal enclosure with a small orifice (an effusion oven approximates this) predicts an effusion rate Γ as given in equation (3.2), where A is the area of the orifice, p_{eq} is the pressure over the solid, M is the molecular weight, N is the number of molecules evaporating from the surface, and k_B and N_A are the Boltzmann and Avogadro constants, respectively.

$$\Gamma \equiv \frac{dN}{dt} = Ap_{eq}\sqrt{\frac{N_A}{2\pi M k_B T}} \quad (\text{mol s}^{-1}) \qquad \text{(Eq. 3.2)}$$

To illustrate the sensitivity of the molecular flux to effusion oven temperature, a demonstration calculation is carried out for selenium. The selenium effusion oven temperature during growth was typically 220 °C. Assigning values for the constants a and b in equation (3.1), the vapor pressure of Se at this growth temperature can be found using equation (3.3).

$$P_{Se}\,(\text{Torr}) = 10^{\left[9.073 - \frac{5{,}714}{T(K)}\right]} \qquad \text{(Eq. 3.3)}$$

Calculating the equilibrium pressure from equation (3.3) and substituting into (3.2), a 1 °C rise in effusion oven temperature results in a 5% rise in the effusion rate and, hence, the flux which is the effusion rate per unit area. In this calculation it was assumed that the molecular weight of Se was some weighted average of Se_2, Se_4 and Se_8 that was insensitive to a one degree rise in temperature. II-VI ternary and quaternary alloys are formed from high vapor species, so composition control is expected to be difficult using effusion ovens.

In actual experiments using the Zn and Se effusion ovens, the flux would vary as much as 20% between the beginning and the end of a film growth, even though long

equilibration times were used. The fluxes were measured by a crystal oscillator which was water cooled to enhance metal deposition and the accuracy of the measurements. There was no clear temporal trend in the crystal oscillator readings that would indicate a drift in effusion oven temperature or depletion of the source; one day the flux might decrease by the end of growth, but the next day it might increase. Visual observation of the metal charge when the shutter was open revealed that the geometry of the metal charge changed with time. It is possible that a redistribution of metal in the oven, which alters the exposed area to vacuum and the characteristics of heating, was the major contributing factor to flux variations from the effusion ovens.

3.2 Metalorganic Gas Sources

The metalorganic gases were delivered to the II-VI reactor without the use of a carrier gas as is done in organometallic vapor phase epitaxy (OMVPE). A major obstacle to using a carrier gas in MOMBE is that the total gas load becomes exceedingly difficult to pump and still maintain conditions for molecular beam transport within the chamber. The vapor phase mass flow controllers were designed to regulate the flow of metalorganics without a carrier gas. A few Torr of vapor pressure at the inlet of the MFC was required for proper operation. The room temperature vapor pressure of all the metalorganics used were considerably higher than the minimum inlet pressure requirement.

A technology issue for MOMBE is whether the purity of the group II and group VI metalorganic gases is sufficient to fabricate electrical and optical devices. This same concern arose when metalorganic gases were first used in III-V epitaxy. Increased demand for electronic grade metalorganics for III-V OMVPE motivated manufactures to produce high purity metalorganics. The same stimulus is leading to the availability of high purity II-VI metalorganics. It is possible to obtain II-VI metalorganic sources with trace impurities at the ppm level as certified by the manufacturer. In spite of these claims, our experience suggests that manufacturer supplied purity analyses should be viewed critically.

It is still advisable to assess the purity of films grown after a metalorganic source gas is changed. The metalorganics used in this research were purchased from a subsidiary of the Morton Thiokal company, CVD Incorporated, based in Danvers, Massachusetts. The metalorganics of diethylzinc (DEZn), dimethylzinc (DMZn), and diethylselenium (DESe) were believed to be of high purity. Low temperature photoluminescence measurements of undoped ZnSe did not exhibit appreciable donor- or acceptor-bound exciton peaks normally associated with impurities.

3.3 Growth Conditions

The growth variables in MOMBE are the temperature of the substrate, the flow rates of the metalorganic gases, and the temperature of the gas cracking zones. When laser-assisted epitaxy was performed, as will be discussed in section 3.5, there were the additional variables of laser intensity and wavelength. A series of experiments were conducted where one parameter was varied at a time in order to systematically map the n-dimensional growth space.

The earliest literature on the MOMBE of ZnSe reported that the growth rate has a

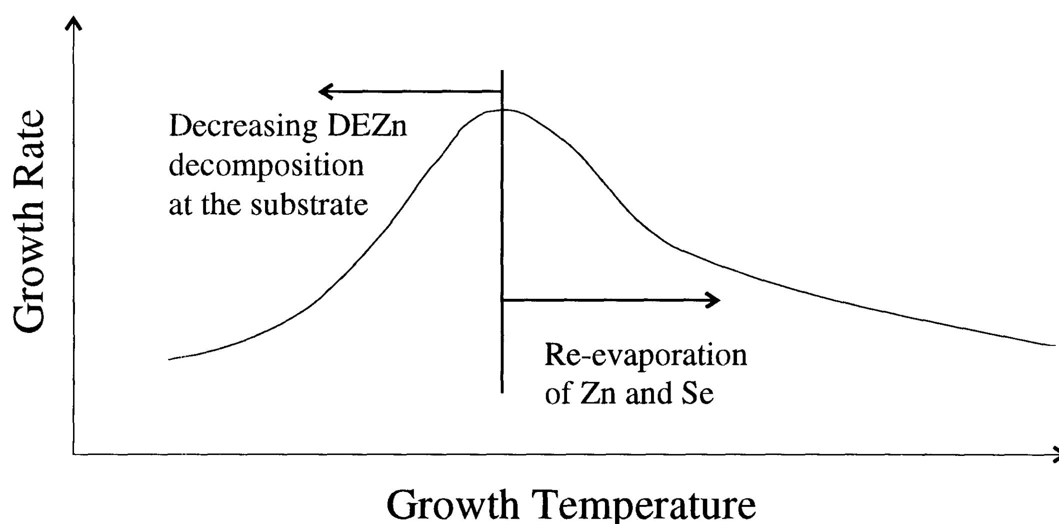

Figure 3.1 Schematic illustration of growth rate dependence of MOMBE on the growth temperature.

strong dependence on the growth (substrate) temperature [49 -50]. A schematic representation of the 'peaked' dependence of the growth rate on the growth temperature is depicted in Figure 3.1. The rapid increase in the growth rate with increasing substrate temperature at low temperatures is postulated to be due to increased thermal decomposition of the zinc metalorganic at the surface, resulting in more Zn metal incorporation into the lattice. The more gradual decrease in the growth rate at higher temperatures is most likely caused by re-evaporation of the constituent elements. In our experiments, the growth temperature was varied from 150 to 475 °C. The lower limit on the growth temperature was the requirement that adatoms have sufficient surface mobility to maintain single crystal, two dimensional growth. At the upper temperature range re-evaporation began to dominate. The majority of the films were grown near a substrate temperature of 320 °C; characterization had identified this as the approximate optimal growth temperature.

Thermal decomposition of the metalorganic gas prior to entering the growth chamber was necessary for DESe, but not DEZn. The average bond energy D_{avg} required to break the first carbon-metal (or hydrogen-metal) bond of the precursor gases used in this research are summarized in Table 3.1. The values were compiled from combined thermochemical and kinetic data [51]. Included in Table 3.1 are values for dimethylzinc (DMZn) and hydrogen selenide (H_2Se) whose use will be described later. Diethylzinc was selected over dimethylzinc in the initial experiments due to its lower decomposition

Table 3.1 Average bond strength of gaseous precursors [51].

Precursor	D_{avg} (kcal/mol)
DESe	58
DEZn	35
DMZn	42
H_2Se	66

temperature. At the growth temperatures investigated (475 °C or less), the thermal energy at the surface was insufficient to pyrolyze the DESe. To determine the required cracking cell temperature of DESe, a quadruple mass spectrometer (QMS) was positioned to intercept the beam exiting the DESe cracker. Analysis of the mass spectra indicated that DESe was thermally decomposed at temperatures ≥ 800 °C. The QMS spectra collected in DEZn cracking experiments indicated that the majority of the DEZn was pyrolyzed at 300 °C by its cracker. Therefore, it was possible in most of the experiments to rely on thermal pyrolysis of the DEZn at the substrate. In the majority of the experiments DEZn was introduced into the chamber near room temperature. When the zinc metalorganic was cracked during injection the growth mode switched to 'MBE-like'; the Zn and Se both arrived at the film surface primarily as metal atoms or clusters as is the case in MBE.

The remaining growth variables were the flow rates of the metalorganic gases. The vapor phase mass flow controllers were capable of regulating flows from 0.1 - 5 sccm. The flows were varied from 0.25 to 2.5 sccm. It was conservatively estimated using an effusion oven flux calculation similar to equation (3.2) [52], that a gas flow of 0.5 sccm would be equivalent to a Zn or Se flux that would result in a growth rate of at least 1500 Å/hr. Subsequent growth experiments using DMZn and solid Se sources appear to support this estimate. The flows were varied to change the mass transport rate and to

Table 3.2 Summary of the growth parameter space investigated for MOMBE of ZnSe using DEZn and DESe source gases. The typical growth conditions are indicated in the final column.

Variable		Values	
	Minimum	Maximum	Typical
Substrate Temperature (°C)	150	475	320
DESe Flow Rate (sccm)	0.25	2.5	0.5
DESe Cracker Temp. (°C)	50	1200	800
DEZn Flow Rate (sccm)	0.5	2.5	0.5
DEZn Cracker Temp. (°C)	25	900	50

alter the VI:II flow ratio. The VI:II flow rate ratio affected the ZnSe film quality which was dependent on the surface stoichiometry at the growth front. The flow rate ratio was varied between 0.2 to 5 in the experiments. Table 3.2 summarizes the growth conditions investigated for MOMBE using the DESe and DEZn sources.

3.4 Low MOMBE Growth Rate

The growth rate (GR) using DEZn and DESe sources was abnormally low [39-43]. The growth rate was less than 400 Å/hr for all investigated growth conditions. The measured growth rates for the growth parameter space explored are shown in Figure 3.2. The growth rate in *angstroms* per hour is plotted against the growth (substrate) temperature to allow a qualitative comparison to Figure 3.1. The data points include significant variations in the following parameters: gas flow rates and VI/II flow rate ratios; the degree of the thermal decomposition of the DEZn which was influenced by its cracker temperature; and the introduction of hydrogen for reasons to be explained. The solid points represent films grown using DESe and DEZn precursors and the open circles denote growths where hydrogen gas was introduced. Figure 3.2 also includes data for 'mixed' source experiments where a diethyl metalorganic and a non diethyl source were used.

The low growth rate observed using DEZn and DESe source gases was in disagreement with a normal growth rate reported by Ando et al. [49,53] in their pioneering work on ZnSe MOMBE using DEZn and DESe. In the original paper [49], a growth rate versus growth temperature plot of similar shape to Figure 3.1 was presented, with a peak growth rate of 0.5 μm/hr indicated for the growth conditions used. An extensive set of experiments were undertaken in an attempt to achieve this reported growth rate using DEZn and DESe source material. These experiments encompassed a broad range of substrate temperatures, flow rates and ratios, and cracking temperatures which spanned the growth conditions reported by Ando et al. in their work. An

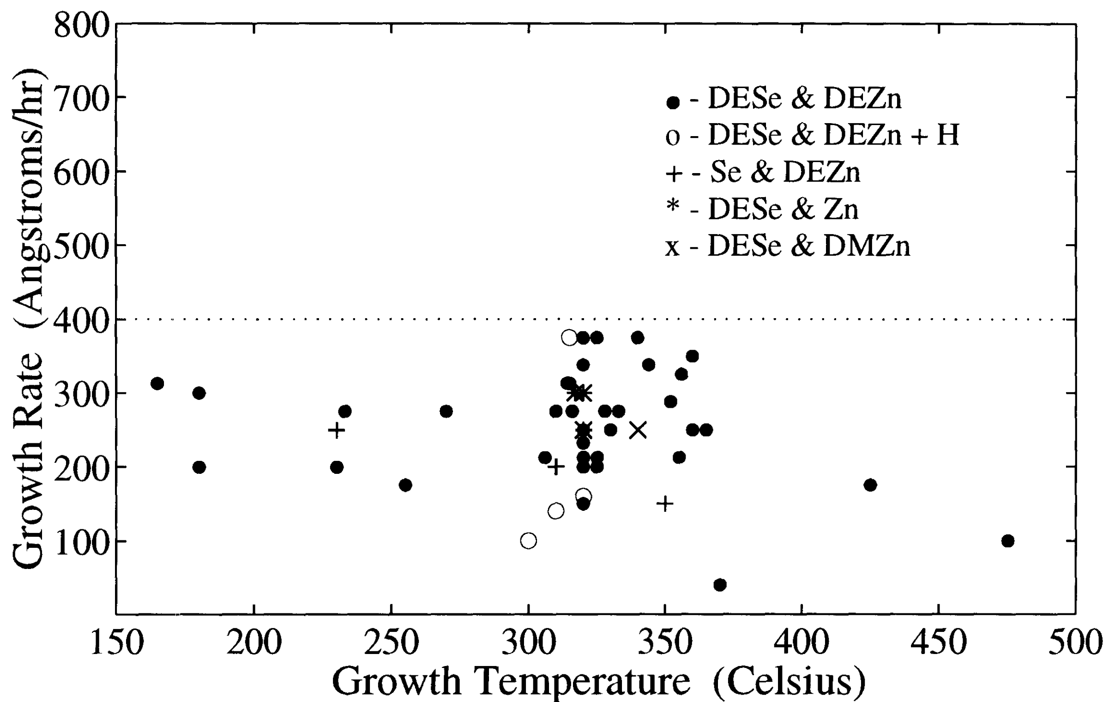

Figure 3.2 MOMBE growth rate versus the growth temperature for all experimental conditions investigated when at least one diethyl metalorganic was used.

unexpected result apparent in Figure 3.2 was that the growth rate remained below 400 Å/hr whenever a diethyl metalorganic source was used. The implication of the low, nearly constant growth rate which exhibited little dependence on growth conditions, was that a reaction at the gas/surface interface involving an ethyl group, e.g. C_2H_5 (ethyl radical) or C_2H_4 (ethylene), or a dissociation product of the diethyl metalorganics, was a rate-limiting step in the kinetics of growth.

3.4.1 Addition of Hydrogen Gas

Hydrogen was introduced during growth to investigate if the persistently low growth rate could be alleviated. The rationale for these experiments was that OMVPE of ZnSe using DEZn and DESe can achieve growth rates of microns per hour [54], and one fundamental difference between MOMBE and OMVPE is that the latter requires a hydrogen carrier gas. In one experiment, hydrogen was mixed with the DESe prior to

cracking. The experiment was designed to investigate if the presence of hydrogen in the cracker would enhance the thermal pyrolysis of DESe, or alter the composition of the cracking by-products, which might then interact to mitigate the growth rate limiting reaction or mechanism. The other experiments introduced hydrogen in a separate heated cracker so that thermally excited, but not dissociated, H_2 would be present at the surface to participate in metal incorporation reactions if needed.

The open circles in Figure 3.2 represent the hydrogen experiments. The observation that these experiments had growth rates less than 400 Å/hr implied that molecular hydrogen had no measurable affect on the growth rate. Three of the experiments using hydrogen had very low growth rates. This bears no significance since these films were grown using a source of metalorganics which were of low purity, and tended to yield lower growth rates.

3.4.2 Mixed Source Experiments

A series of 'mixed' source experiments were conducted in an effort to elucidate the origin of the low growth rate [40-43]. A mixed source experiment employed one diethyl metalorganic source with either a solid metal source or dimethylzinc. The growth rates for three combinations of these mixed source experiments are plotted in Figure 3.2 and are less than 400 Å/hr. Based on the experiments utilizing different combinations of Zn and Se source materials, it became evident that a by-product of the diethyl metalorganic decomposition was responsible for the growth rate limitation; the common factor in all experiments with a low growth rate was the presence of an ethyl metalorganic. To verify that a system related problem was not the cause, MBE and MOMBE using DMZn and elemental Se were performed. The growth rates in these experiments were only limited by the mass transport of source material. Table 3.3 summarizes the combinations of zinc and selenium sources used and the resultant rates of growth. A 'high' entry in the growth rate (GR) column indicates normal growth rates while 'low' denotes that the growth rate was

Table 3.3 Summary of the MOMBE growth rates observed for different combinations of Zn and Se source materials.

Source of Zn	Source of Se	MOMBE GR*
DEZn	DESe	No Growth
DEZn	Cracked DESe	Low
DEZn	Elemental Se	Low
Cracked DEZn	Cracked DESe	Low
Elemental Zn	Cracked DESe	Low
Cracked DMZn	Cracked DESe	Low
Cracked DMZn	Elemental Se	High
Elemental Zn	Elemental Se	High

* Low: less than 400 Å/hr. High: typical of MBE

kinetically limited to less than 400 Å/hr. Special attention is drawn to the entry where DEZn and elemental selenium were the sources. The low entry for this combination of sources demonstrates that it was not inefficient cracking of the DESe that was responsible for the low growth rate. Based on the summarized results in Table 3.3, we have hypothesized that at the necessarily low ZnSe growth temperatures investigated, blockage of metal incorporation sites by chemisorbed ethyl radicals was occurring [39-43].

The low MOMBE growth rate using DESe and DEZn deterred us from doping ZnSe and producing device structures. A minimum film thickness of approximately one micron is required for capacitance-voltage and Hall effect measurements of undoped films; otherwise, the depletion width on the semiconductor side of the metal-semiconductor interface might extend to the substrate resulting in parallel conduction of current in the substrate. Fabricating devices was impractical due to a minimum thickness requirement of several microns.

3.4.3 Site Blockage by Ethyl Radicals

An understanding of the surface chemical processes taking place in MOMBE would be an aid to unraveling the low growth rate phenomena observed. No specific studies have been made of the growth kinetics of ZnSe MOMBE, but recent research investigating the adsorption and decomposition of triethylgallium (TEG) [55 ,56] and DEZn [57] on GaAs(100) has been published. Additionally, kinetic models of GaAs CBE/MOMBE growth using TEG and arsine have been proposed [58 ,59]. I believe there is applicability of these surface science experiments and growth models to the MOMBE of ZnSe. The adsorption and decomposition of DEZn decomposition on a ZnSe(100) surface is likely to be similar to that of TEG and DEZn on GaAs(100).

Direct experimental confirmation that ethyl radicals are tightly bound to a GaAs surface at temperatures less than 330 °C was obtained by Murrell et al. [55] and Banse and Creighton [56] in studies of the surface chemistry of triethylgallium adsorption and decomposition on GaAs(100). Temperature programmed desorption (TPD) in conjunction with x-ray photoelectron spectroscopy, low energy electron diffraction, and high resolution electron energy-loss spectroscopy were used in these studies to identify desorbing species and to determine stable reaction intermediates on the surface as a function of substrate temperature.

Murrell et al. and Banse and Creighton reported that ethylene (C_2H_4), ethyl radicals (C_2H_5), and hydrogen (H_2) would desorb from the surface near 330 °C, and ethane (C_2H_6) at a slightly higher temperature of 350 °C. Three competing reactions were proposed to explain the desorption of the ethyl groups. The simplest reaction shown in equation (3.4), was the direct desorption of ethyl radicals from the chemisorbed state.

$$C_2H_{5(ads)} \rightarrow C_2H_{5(g)} \qquad \text{(Eq. 3.4)}$$

This reaction could not explain the nearly identical desorption temperature of C_2H_4 and H_2 in the TPD signals. To account for this observation, it was suggested a β-hydride elimination reaction, equation (3.5), was removing the ethyl radicals from the surface.

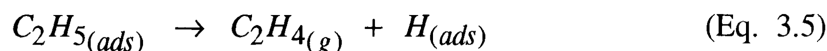

$$C_2H_{5(ads)} \rightarrow C_2H_{4(g)} + H_{(ads)} \qquad \text{(Eq. 3.5)}$$

The surface recombination rate of adsorbed H to molecular H_2(g) was assumed to be very fast compared to all other reactions, so the removal of hydrogen from the surface was not a rate limiting step. Further support for the β-hydride elimination reaction was provided by studies of the desorption of H_2 from a GaAs(100) surface [55]. Hydrogen desorbed from the GaAs at 250 °C, a 80 °C lower temperature than observed in the decomposition of TEG. This and other data indicated that hydrogen desorption was controlled by a rate-limiting step, rather than a simple desorption process, suggesting that a β-hydride elimination reaction was occurring. A third possibility was the surface recombination of ethyl radicals with adsorbed atomic hydrogen forming volatile ethane.

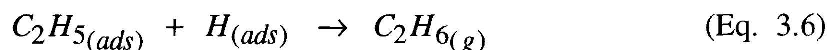

$$C_2H_{5(ads)} + H_{(ads)} \rightarrow C_2H_{6(g)} \qquad \text{(Eq. 3.6)}$$

Ethane (C_2H_6) was detected in the TPD experiments, but it was inconclusive as to whether ethane was being formed at the surface or in wall reactions between gaseous ethyl radicals and hydrogen [56]. The β-hydride elimination reaction in equation (3.5) was inferred to be the dominant reaction for the removal of ethyl radicals based on the data.

Rueter and Vohs [57] examined the adsorption and dissociation chemistry of DEZn on GaAs(100). The desorption temperatures they observed for ethylene, ethyl radicals, and hydrogen were lower by approximately 80 °C (250 °C). The lower desorption temperatures might have been due to the presence of Zn on the surface lowering the reaction/desorption temperatures [57]. They concluded that a β-hydride elimination reaction and direct desorption of ethyl radicals (equations (3.4) and (3.5)) were the origin

of the TPD signals at 250 °C. Ethane (C_2H_6) was also detected at a slightly higher desorption temperature, but ethane was estimated to be only 1-4% of the hydrocarbon products on the surface.

Murrell and co-workers [55] developed a model for the observed TPD which calculated the steady-state surface coverage of the adsorbed species. The computer simulations closely reproduced the thermal desorption spectra they had measured experimentally. One result predicted by the simulation was that *ethyl species would build-up on the surface blocking adsorption sites for the TEG when the temperature fell below 430 °C.* Computer modeling of the reaction kinetics of CBE growth of GaAs has also been performed [58,59]. The CBE growth models calculated the steady-state surface concentrations of adsorbed species as a function of growth temperature. Using kinetic parameters derived from the recent surface science experiments on TEG decomposition and desorption [55-57], it was predicted that adsorbed ethyl groups would block the adsorption of TEG at temperatures less than 430 °C resulting in a decrease of the growth rate.

In summary, adsorption and decomposition studies of triethylgallium and diethylgallium on GaAs(100) observed that ethyl radicals remained chemisorbed on a GaAs(100) surface at temperatures up to 330 °C. Modeling of the surface reaction kinetics indicated that the coverage of ethyl radicals would inhibit adsorption of TEG (and hence, growth) at temperatures below 430 °C. The temperature at which ethyl radical coverage begins to block adsorption sites is most likely different for a ZnSe(100) surface, but the temperature might be in the range of normal ZnSe growth temperatures. The surface science experiments and growth models described in this section support the existence of a surface which is chemically passivated by chemisorbed ethyl radicals, which has been postulated to explain the low growth rate in MOMBE when using a diethyl metalorganic source.

3.4.4 Other Reported MOMBE Results

Besides the pioneering work of Ando et al. [49], only one other group has presented research on MOMBE using DESe and DEZn. Rajavel et al. at Hughes Research Laboratories recently reported that they had achieved normal growth rates using similar growth conditions to our experiments [60]. A brief effort to do MOMBE using these diethyl metalorganics was made at AT&T Bell Laboratories in which they observed an abnormally low growth rate, but the results were never published [61]. Table 3.4 compares the MOMBE growth conditions and the resultant growth rates for experiments performed by our group and by the researchers at Hughes Research Laboratories [60,62]. The growth conditions were very similar for these 'MBE-like' MOMBE experiments, which points to an equipment related cause for the markedly different observed growth rates. In the early stages of our MOMBE research a low cracking efficiency of the DESe cracking injector was suspected to be the origin of the low growth rate, even though cracking experiments using the quadruple mass spectrometer indicated the DESe was being thermally decomposed. Subsequent experiments with an elemental zinc source also experienced the low rates of growth, which suggests a more subtle equipment related phenomenon had produced the very different rates of growth.

The designs of the metalorganic gas cracking cells were different amongst the research efforts investigating MOMBE using diethyl metalorganics. Conversations with Dr. Rajavel [62] revealed that a modified VG Semicon metalorganic cracker was used to thermally decompose the DESe at 900 °C during growth; the DEZn was cracked at 800 °C in a commercial VG metalorganic cracker. The modifications to the DESe cracker were part of a proprietary design which consisted of a quartz tube surrounded by heater filaments, with internal baffling to insure that the metalorganic gases experienced wall collisions in the heated cracking zone. The Hughes group's motivation for using a quartz cracker was to avoid tantalum, the usual cracker catalytic material, because it reacted with tellurium during growth of ZnTe. Ando et al. had built their own DESe cracking cells

Table 3.4 Comparison of observed growth rates for MOMBE using DEZn and DESe source gases as reported by our group and Hughes Research Laboratories [60,62]. The Hughes MOMBE experiments were performed using very similar growth conditions, yet they were able to achieve a high growth rate.

Investigator	Growth Temp. (°C)	DEZn (Cracking Temperature °C)	DESe (Cracking Temperature °C)	Growth Rate (μm/hr)
Hughes Research Laboratories:	220-325	~ 1 sccm (800)	~ 1 sccm (900)	1.0-1.5
MIT CBE Laboratory:				
ZnSe # 5	320	0.5 sccm (800)	0.5 sccm (1000)	0.015
ZnSe # 6	370	0.5 sccm (900)	0.5 sccm (1000)	0.004

using a quartz gas tube with a Ta wire inside to heat the metalorganics [49]. Our DESe cracker shown in detail in Figure 2.3 consisted of a PBN gas injection tube with a Ta baffle insert down the center to promote gas collisions. The filament assembly surrounded the outside of the PBN tube. The construction of the AT&T group's cracker is unknown. Since Ando et al. had performed MOMBE without cracking the DEZn and achieved high growth rates [49], and the Hughes researchers had used a specially designed DESe cracker, the construction of the DESe cracking cell appears to have been a critical factor influencing the growth rate.

Recent research on atomic layer epitaxy (ALE) of Ge using diethylgermane [63] indicates that atomic H might be necessary to scavenge adsorbed ethyl radicals (C_2H_5) from a semiconductor surface at low temperature. In the ALE of Ge, the substrate at 250 °C was exposed to alternating beams of diethylgermane and H per cycle. The atomic hydrogen which was created by heating H_2 with a tungsten filament at 2000 °C was used to recover a clean surface through the removal of C_2H_5 and other adsorbed species. Without the hydrogen exposure the growth rate was low (< 500 Å/hr) and considered 'self-limited'. Depending on the H_2/diethylgermane ratio, the growth rate could be enhanced by a factor of 4-8.

The evidence suggests a cracking by-product of DESe decomposition was necessary to remove the kinetic limitation in growth caused by ethyl radical passivation of surface sites. I speculate that the quartz crackers used by the other investigators were producing an atomic hydrogen flux, and the PBN cracker we used was producing little, if any, atomic hydrogen. The atomic hydrogen present at the surface is hypothesized to participate in reactions which remove the ethyl radicals, similar to what was observed in the growth of Ge using diethylgermane [63], thus preventing passivation of the surface. This hypothesis might be tested in future experiments by modifying the design of our DESe cracker, or by introducing atomic hydrogen during growth using a plasma source.

3.5 Laser-Assisted MOMBE

Concurrent to the investigation of MOMBE, laser-assisted growth experiments were conducted by illuminating a portion of the wafer with laser light. It was observed that the growth rate could be either enhanced or suppressed in the illuminated region, depending on the growth conditions [39-43]. In the case of laser induced growth rate enhancement, the growth rate could be increased by over an order of magnitude, suggesting the potential for selective area epitaxy.

Ando et al. was the first group to experiment with photo-assisted growth of ZnSe from metalorganic sources [64]. The experiments involved ultraviolet irradiation of the substrate during OMVPE from diethylzinc and dimethylselenide source gases. The light source was a low-pressure mercury lamp emitting ultraviolet (UV) light primarily at 185 and 254 nm. It was demonstrated that UV illumination enhanced the growth rate over the entire temperature range investigated, and permitted epitaxial growth at much lower temperatures. Other researchers extended the investigation of photo-assisted OMVPE of ZnSe by examining the wavelength dependence of growth rate enhancement using filtered Xenon lamp irradiation [65] and the different emission lines of an argon ion laser [66].

In both studies the researchers observed a threshold photon energy to induce growth rate enhancement.

3.5.1 Laser-Assisted Growth Set-Up

The laser-assisted MOMBE experiments were accomplished by directing laser light through a viewport at one of the effusion oven locations. The viewport was oriented 45° with respect to the substrate normal, so the laser beam spot would form an ellipse on the wafer. Figure 3.3 is a schematic drawing of the optical path from the laser to the substrate. A continuous wave (cw) intensity of 180 mW/cm^2 was used in most experiments in order that the effect of illumination by different laser emission lines could be compared. This low illumination intensity insured that local thermal heating of the substrate was negligible. The local temperature rise ΔT induced by a cw laser beam

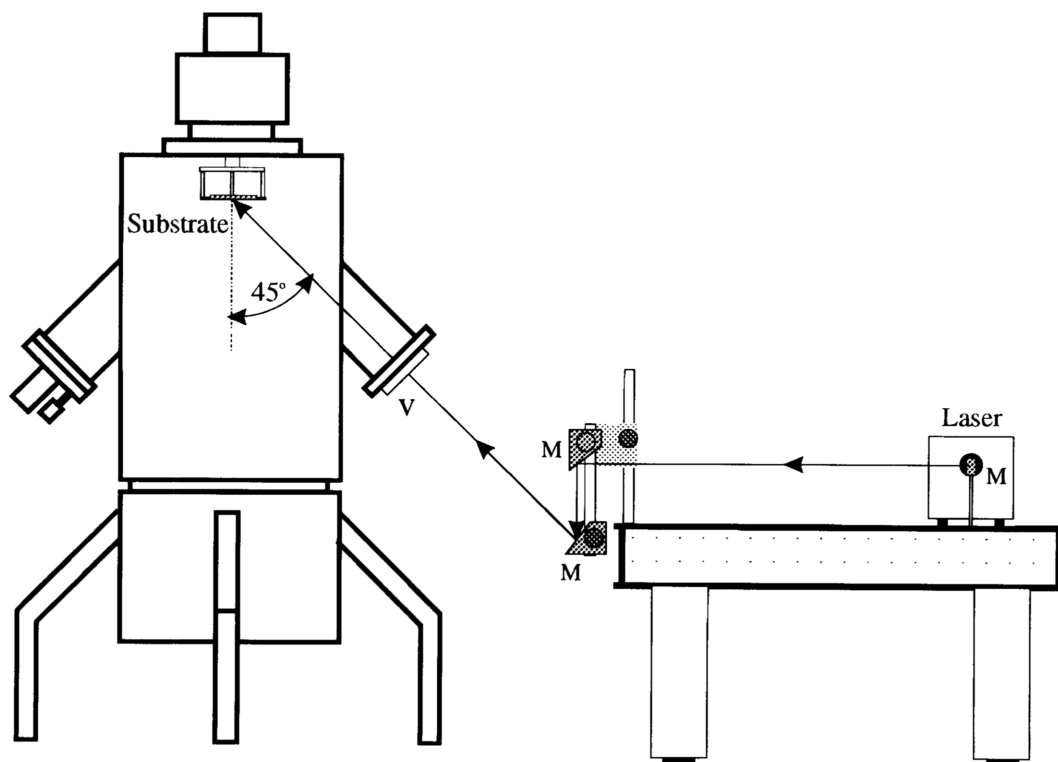

Figure 3.3 Schematic drawing illustrating light path in laser-assisted growth experiments. M indicates the location of a mirror and V indicates the viewport.

impinging on a solid was estimated using equation (3.7) [67],

$$\Delta T = \frac{2(1 - r)P}{\pi KD} , \qquad \text{(Eq. 3.7)}$$

where r is the reflectivity of the sample, P is the laser power, K is the sample's heat conductivity, and D is the diameter of the laser spot at the surface. Assuming that $r = 0$ (worst case), converting the laser power density of 180 mW/cm^2 into a (P/D) value of 0.25 W/cm, and using $K = 0.19$ W/cm·K from Table 1.2, the local temperature rise ΔT in ZnSe induced by the laser was estimated to be less than 1 degree K. A similar calculation for GaAs using $K = 0.17$ W/cm·K [68] predicts that the temperature rise in the GaAs substrate was also less than 1 K.

Three lasers were used in these experiments. The primary laser was a 5 Watt argon ion laser (Spectra-Physics, model 2025). All of the powerful visible emission lines and the combined UV lines were used for illumination. A dye laser (Coumarin 7 dye) pumped by the argon ion laser provided a nearly continuous set of emission lines near the ZnSe bandgap. A Ti:sapphire laser pumped by the Ar^+ laser was used to illuminate with radiation far below the bandedge. The laser wavelengths used are summarized in Table 3.5.

Table 3.5 Summary of the different laser wavelengths used for illumination during the laser-assisted MOMBE growth experiments.

Wavelength (nm)	Spectrum	Laser
780	infrared	Ti:saphire
555	visible	dye
538	visible	dye
520	visible	dye
515	visible	Ar^+
488	visible	Ar^+
458	visible	Ar^+
352-364	ultraviolet	Ar^+

Metal films would coat the laser viewport over time, and in particular, would deposit most heavily where the laser was incident on the glass. The deposited spots would absorb some of the incident radiation; the net effect was to slightly reduce the laser intensity at the substrate as growth proceeded. The viewport had a maximum bake-out temperature of 250 °C which prevented heating the window to a high enough temperature to re-evaporate the spots. The decline in intensity due to spot formation hindered the collection of quantitative data on laser-induced changes in the growth rate.

3.5.2 Growth Rate Enhancement

Laser illumination was observed to increase the growth rate over that of unilluminated regions of the same film. The degree of enhancement depended on the growth conditions and the sources used, and was observed to be as great as 15 times the unilluminated growth rate. The growth rate as a function of substrate temperature for both illuminated

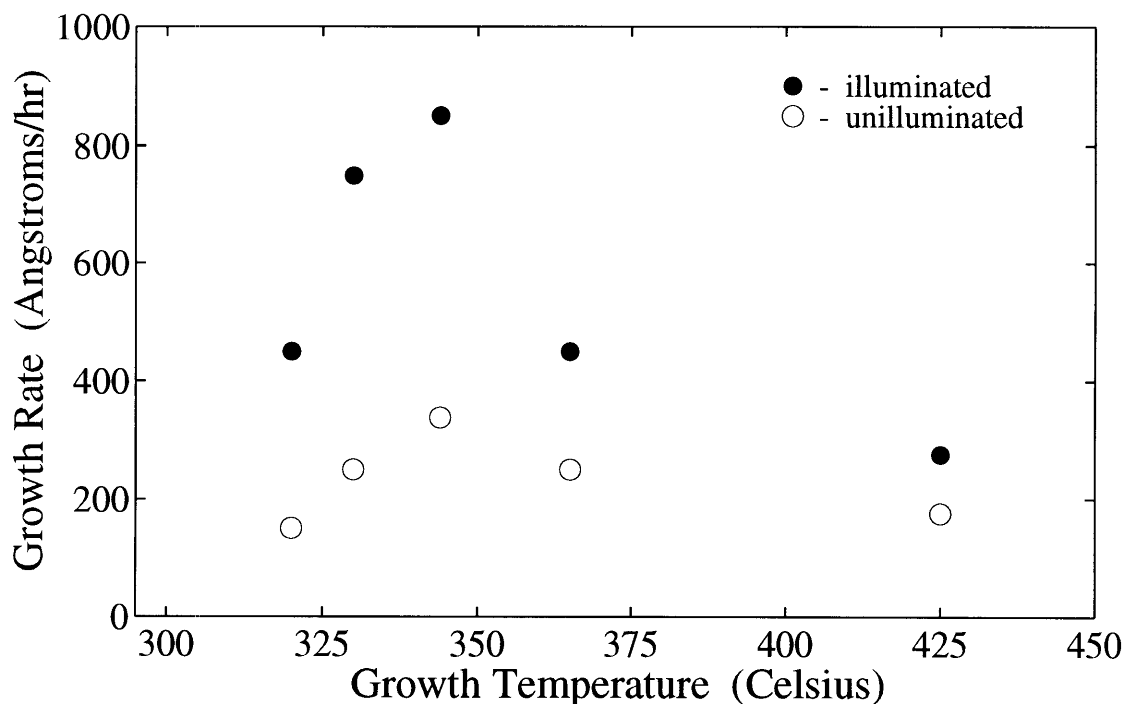

Figure 3.4 Growth rate versus substrate temperature for regions of a film which were illuminated (•) by the laser, and received no illumination (o). The gas flows were 2.5 and 0.5 sccm for DEZn and DESe, respectively, and the laser illumination wavelength was 458 nm.

and unilluminated regions of a film are shown in Figure 3.4. The flow rates for the data displayed in Figure 3.4 were 2.5 and 0.5 sccm for DEZn and DESe, respectively, and the laser illumination wavelength was 458 nm. What is evident from Figure 3.4, but is not apparent in Figure 3.2, is that for fixed gas flows and cracking conditions, there was a peaked dependence of the GR on growth temperature. The increase in the GR due to laser illumination was approximately a factor of 2.5 for each point; a more precise determination of the enhancement factor was not possible due to the uncertainty in the intensity caused by spot formation on the laser viewport. The higher growth rate of the illuminated data more clearly illustrates the strong temperature dependence of MOMBE growth, and the curve shape resembles Figure 3.1 which is characteristic of MOMBE.

3.5.3 Intensity Dependence

The low growth rate enabled the effect of laser irradiation to be visible to the eye. ZnSe films were transparent to all but the shortest visible light wavelengths and were usually less than 1000 Å thick, so interference fringes were visible wherever a thickness gradient existed. The lasers were normally operated in the TEM_{00} mode which has a Gaussian intensity profile. The characteristic fringe pattern of a ZnSe epilayer grown with laser-assistance was an elliptical spot with concentric colored 'rings'.

A thickness profile was obtained by selectively etching the ZnSe from the GaAs, and using a stylus profilometer (Tencor Instruments, Alpha-Step 100) to measure the step formed at the region where the ZnSe was removed. The profilometer was calibrated against VLSI step standards and found to be accurate to ± 50 Å. An intensity profile was measured from the center of a laser illuminated spot out to the edge of the unilluminated region. The thickness profile and a Gaussian curve normalized to the height of the measured data are shown in Figure 3.5. The enhancement ratio plotted on the y-axis is defined as the ratio of the thickness in the laser illuminated region to that of the unilluminated film. The agreement between the ratio of the measured thicknesses and the

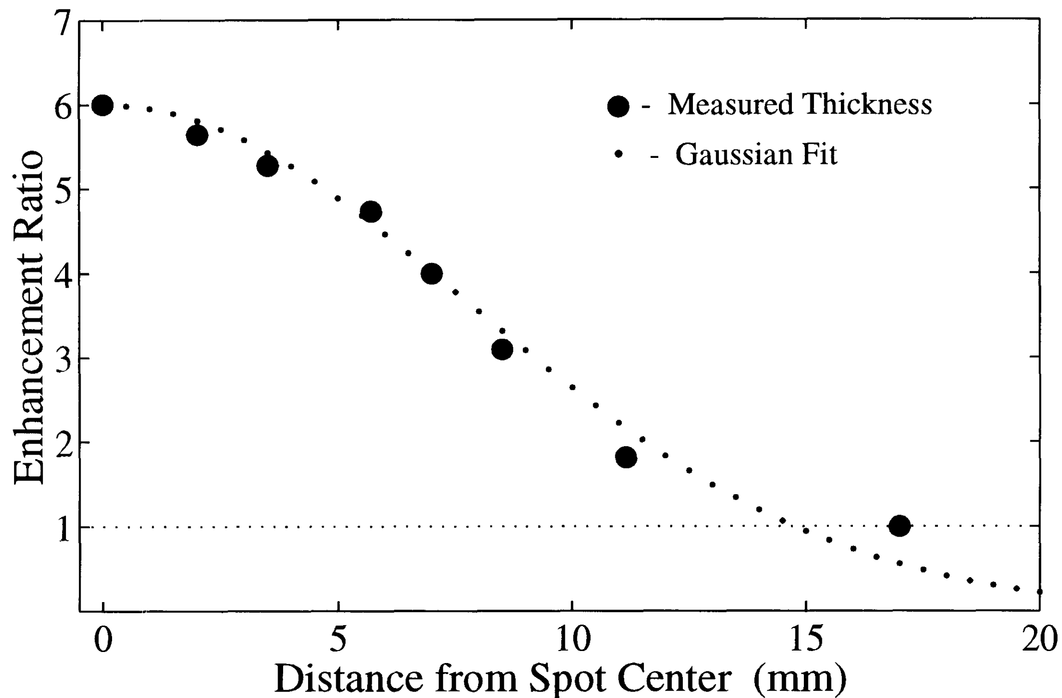

Figure 3.5 A thickness profile measured from the center of a laser enhanced growth spot to the edge of the unilluminated region.

fitted Gaussian curve (representing the Gaussian intensity profile of the laser) strongly suggested that the growth rate enhancement was proportional to the intensity.

3.5.4 Wavelength Dependence

The growth rate enhancement of photo-assisted OMVPE performed using either a filtered broadband light source [65], or the emission lines of an argon ion laser [66], was reported to be wavelength dependent. Illumination of the substrate with photons whose energy was above the bandgap of ZnSe were required for growth rate enhancement to occur. The investigators of the photo-assisted OMVPE studies proposed models for growth rate enhancement where photo-generated electron-hole pairs were integral to the enhancement mechanism. The photo-assisted enhancement in the growth rate when using metalorganic sources contrasts with the suppression of the growth rate that has been observed when illuminating with above bandgap radiation during MBE [42,69 -72].

The advantage of using monochromatic radiation in our study was that the energy of the photons inducing a particular effect could be isolated. The bandgap of ZnSe as a function of temperature was estimated using equation (3.8) [66],

$$E_g = 2.67 - 7.2\text{x}10^{-4}\,(T - 297)\ \ [\text{eV}]. \qquad \text{(Eq. 3.8)}$$

At the most frequently investigated growth temperature of 320 °C the bandgap was 2.45 eV. This bandgap energy was lower than the energy of the argon ion laser lines except for the 515 nm line. Enhancement in the growth rate was observed with all Ar^+ laser lines, although the degree of enhancement was less when using the 515 nm line. To examine the effect of illumination near the bandedge, a tunable dye laser (Coumarin 7 dye) was employed. A Ti:sapphire laser with a wavelength of 780 nm was used to provide

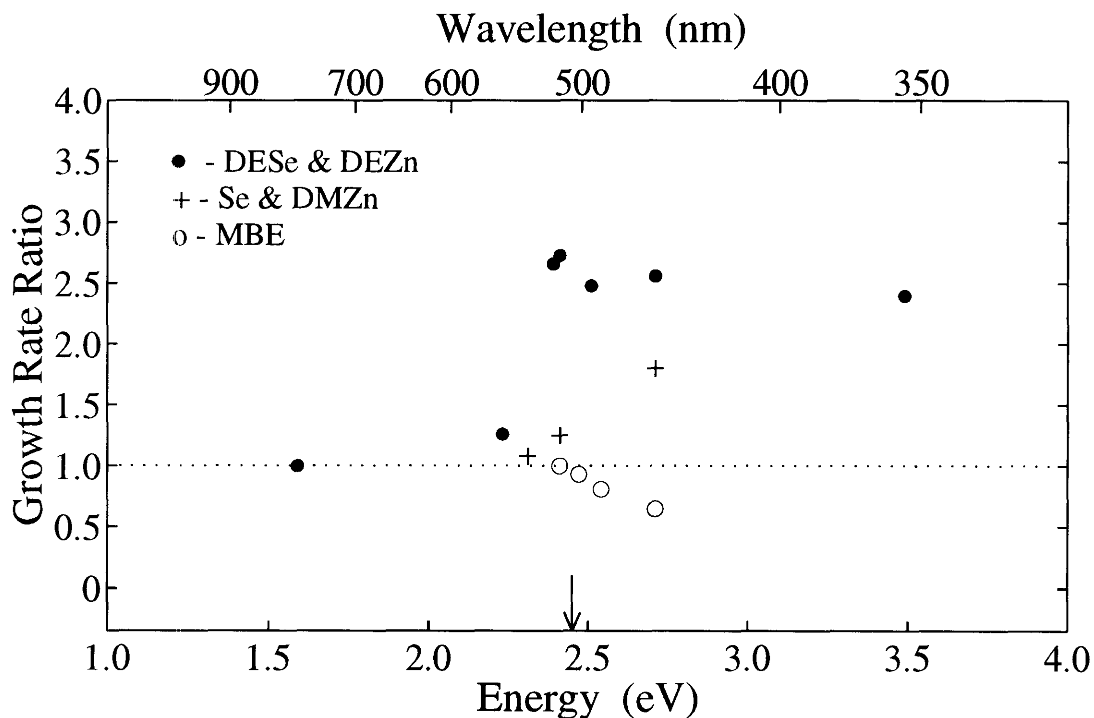

Figure 3.6 The dependence of the growth rate enhancement during MOMBE (solid points and crosses), and the growth rate suppression during MBE (open circles), as a function of laser illumination energy. The bandgap E_g of ZnSe at a growth temperature of 320 °C is indicated by the arrow.

illumination far below the bandgap energy.

Figure 3.6 presents the wavelength dependence of the growth rate ratio (defined as the ratio of the GR in the laser illuminated region to the GR in the unilluminated region) for both GR enhancement and suppression. The growth rate ratio is plotted versus the laser photon energies for the cases of: 1) MOMBE from DESe and DEZn (solid points), 2) MOMBE using Se and DMZn (crosses), and 3) MBE growth (open circles). The growth temperature for the MOMBE experiments using solid Se and DMZn was 340 °C which resulted in a slightly lower bandgap. For each set of experiments, the growth conditions which are shown in Table 3.6 were identical except for the choice of the laser emission line.

The inference from Figure 3.6 was that enhancement or suppression of the growth rate required photons with energies approximately greater than the bandgap. Thermal absorption is known to increase significantly above the bandedge [73], but due to the low illumination intensity used it was estimated that the temperature rose less than 1 °C (see

Table 3.6 Growth conditions for the MOMBE and MBE laser-assisted growth experiments where the wavelength dependence of the growth rate enhancement or suppression is shown in Figure 3.6.

Precursors	Growth Parameter		Value
DESe & DEZn			
	Substrate Temperature	(°C)	310-320
	DESe (800 °C)	(sccm)	0.5
	DEZn (50 °C)	(sccm)	0.5
Se & DMZn			
	Substrate Temperature	(°C)	340
	Se Flux	(Å/s)	0.47-0.57
	DMZn (1050 °C)	(sccm)	1.65-2.0
MBE			
	Substrate Temperature	(°C)	320
	VI:II Flux Ratio		~ 1:1
	ZnSe Growth Rate	(Å/s)	0.41-0.45

section 3.5.1). The direct absorption bands of the metalorganics existed at much shorter wavelengths [74] (248 nm for DEZn) eliminating the possibility of direct photolysis of the metalorganics. This suggested that photo-generated electron-hole pairs were responsible for the growth enhancement or suppression as previously reported in OMVPE [64-66].

Whether the growth rate was enhanced or suppressed depended on the state of dissociation of the DEZn or DMZn. The growth rate was enhanced if unpyrolyzed (or partially decomposed) DEZn was present at the surface. Conversely, elemental Zn present at the surface originating from a Knudsen cell during MBE or created in the thermal decomposition of DEZn in the gas cracker during MOMBE, resulted in growth rate suppression. Table 3.7 summarizes the effect laser illumination had on the MOMBE experiments. In Table 3.7 the combinations of the zinc and selenium sources investigated are presented with the resultant growth rate modifications induced by laser illumination. MOMBE growth where the zinc metalorganic was thermally decomposed in its cracker is referred to as 'MBE-like' growth. The source combinations which resulted in GR suppression were either MBE or 'MBE-like' in that both the Zn and Se arrived at the growing surface primarily as metal atoms or clusters. The entries for MOMBE using

Table 3.7 The modification of the growth rate induced by laser illumination during MOMBE and MBE is summarized for the different combinations of sources used.

Source of Zn	Source of Se	Effect of Laser Illumination
DEZn	DESe	None
DEZn	Cracked DESe	Enhancement
DEZn	Elemental Se	Enhancement
Cracked DEZn	Cracked DESe	Suppression
Elemental Zn	Cracked DESe	Suppression
Cracked DMZn	Cracked DESe	Suppression or Enhancement
Cracked DMZn	Elemental Se	Suppression or Enhancement
Elemental Zn	Elemental Se	Suppression

dimethylzinc were more complicated in that both suppression and enhancement were observed. MOMBE using DMZn will be discussed further in section 3.6. The suppression of the growth rate due to laser illumination in the 'MBE-like' growth mode was similar to that reported for MBE, except that it was the suppression of the kinetically limited low growth rate.

3.5.5 Flow Ratio Dependence

The observation that growth rate enhancement required partially or unpyrolyzed DEZn

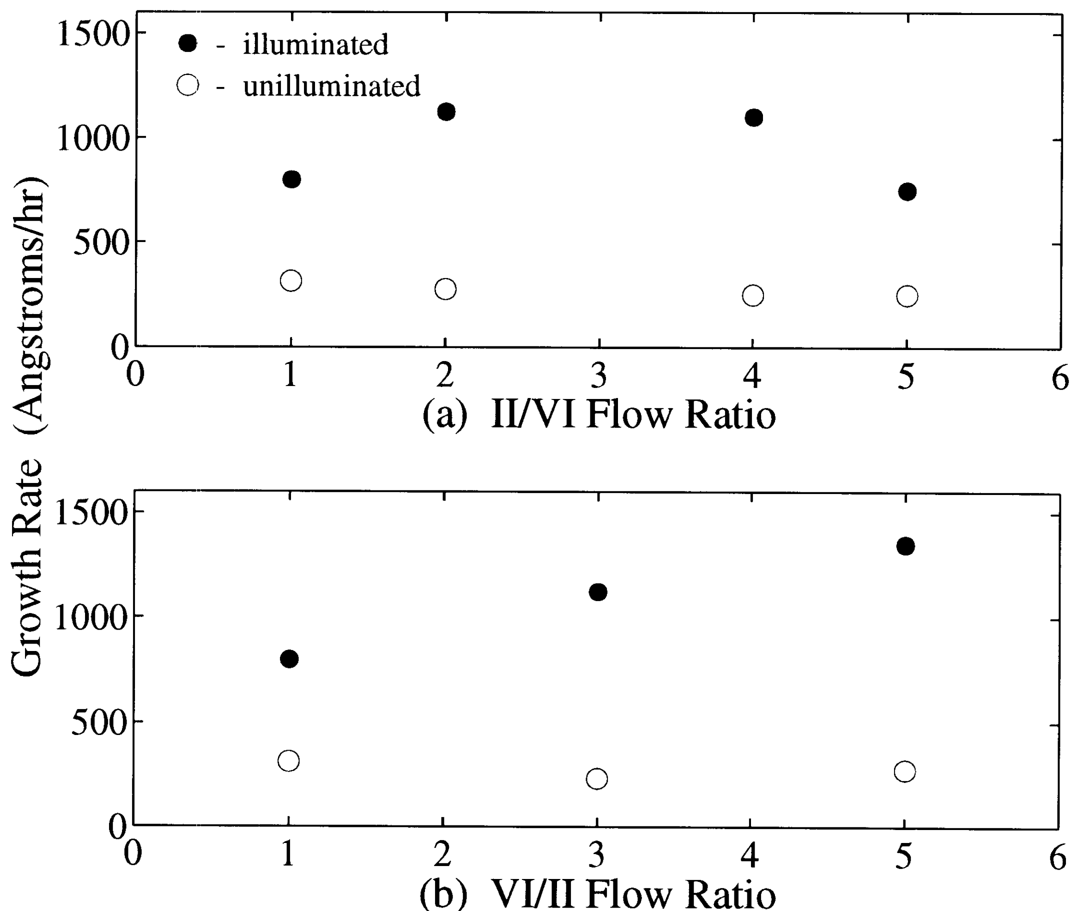

Figure 3.7 Illustration of dependence of growth rate on the gas flow ratios. The DEZn:DESe (II/VI) flow ratio dependence is shown in (a). The flow ratio is inverted in (b) for clarity of presentation of the II/VI ratios less than unity. In these experiments the growth temperature was 320°C, the DEZn and DESe flows ranged from 0.25-2.5 sccm, and the laser illumination wavelength was 458 nm.

at the surface was further supported by studies of the flow ratio dependence of the GR enhancement. Increasing the flow rate of uncracked DEZn for a fixed flow of DESe (0.5 sccm) increased the laser-assisted growth rate as shown in Figure 3.7(a). Larger II/VI flow ratios increased the concentration of the partially or unpyrolyzed DEZn at the surface. The decrease in the illuminated GR at a II/VI flow ratio of 5 might be due to the increased rate of spot formation with increasing DEZn flows. Growth at low substrate temperatures where DEZn was not expected to be efficiently decomposed also experienced larger GR enhancement. It was also observed that II/VI ratios less than unity (VI/II flow ratios greater than one) resulted in larger laser induced growth rates as seen in Figure 3.7(b). A possible explanation for the VI/II flow ratio dependence of the GR is discussed in section 3.8.

3.6 MOMBE Using DMZn and Solid Se

The difficulties experienced in increasing the growth rate with diethyl metalorganics was a contributing factor in the change to dimethylzinc (DMZn) and solid Se precursors. These sources were selected only as a verification test of the MOMBE system; the combination was far from optimal since the higher vapor pressure element was a metal sublimated from a Knudsen cell. Growth using DMZn and elemental Se was mass-transport limited. The attainment of normal growth rates using DMZn and solid Se was additional evidence that chemisorbed ethyl radicals were passivating the metal incorporation sites in MOMBE using DEZn and/or DESe sources.

The higher bond energy of the DMZn compared to DEZn (see Table 3.1) required that it be cracked prior to injection. Cracking complicated the observations of the growth rate modifications induced by the laser. Similar to what was observed using DEZn, the presence of some form of metalorganic zinc at the surface was necessary for growth rate enhancement. Based on the post-growth observations of enhancement or suppression, it was concluded that the state of DMZn on the surface was dependent on the growth

temperature, *and* the combination of cracker temperature and flow rate of DMZn. As an example, if the DMZn cracker was set at a low cracking temperature of 900 °C, laser illumination enhanced the growth rate. Conversely, if the cracker was set at 1050 °C, the growth rate was suppressed for the same growth temperature and DMZn flow rate. An insufficient number of experiments were performed to elucidate which growth conditions lead to enhancement or suppression using DMZn; MOMBE with DMZn was conducted only to demonstrate that an ethyl-based metalorganic was responsible for the low growth rate. Optimization of the growth conditions for MOMBE using DMZn and solid Se sources was attempted, but optical characterization by low temperature photoluminescence of the films always indicated the presence of structural defects and/or impurities. Due to concerns about the purity of the DMZn source, further research into MOMBE with DMZn and solid Se sources was discontinued.

3.7 Electron-Beam Assisted Growth

Early in the MOMBE experiments it was discovered that the electron-beam was inducing similar modifications to the growth rate as the laser. The reflection high-energy electron diffraction (RHEED) gun was normally turned on briefly during a growth because operation when the chamber pressure was in the 10^{-4} Torr range greatly reduced the lifetime of the filament and risked high voltage arcing. The effect of the electron-beam was probably first noted when the RHEED gun was accidentally left on for an extended period during growth. A colored streak appeared where the beam was incident on the surface and was measured to have increased the growth rate. After this discovery, the RHEED gun was left on during selected experiments to verify that the effect of the electron-beam was qualitatively similar to that of the laser. Observations were only qualitative due to limited flexibility in controlling the electron-beam source which was dictated by the chamber pressure. The intended mission of the RHEED gun was to provide diffraction information on the growth surface, so keeping it operational for this

task was of primary importance. To achieve this end, the gun was operated sparsely at low acceleration voltages and beam currents in the harsh operational environment of MOMBE growth.

The electron-beam was observed to effect the MOMBE growth in the same manner as above bandgap laser radiation. An incident electron-beam can produce a cascade of electron-hole pairs in a semiconductor. The effect of the electron-beam when various combinations of sources were used was identical to those summarized in Table 3.7 for the laser. Enhancement was greatest when large concentrations of partially or undecomposed DEZn were present on the surface. The electron-beam also suppressed the growth rate in MBE. To the author, the identical phenomenological influence of the laser and electron-beam on growth suggests that the underlying growth rate enhancement and suppression mechanism(s) were the same. Electron-beam modification of the growth rate has the potential to selectively write fine line features if the method could be adapted to a precision electron-beam source such as a scanning electron microscope.

3.8 Model for Laser-Assisted Growth.

Yoshikawa has reviewed the results of laser-assisted OMVPE of ZnSe films using an Ar ion laser as the irradiation source [75]. The OMVPE growth was performed using dimethylzinc and dimethylselenium sources. The following observations were presented concerning laser-assisted OMVPE: (1) Photons with energies higher than the bandgap of ZnSe at the growth temperature contributed to the growth; (2) the initial growth rate under laser-illumination was increased with increasing thickness of a pre-deposited ZnSe layer; and (3) the quantum yield for forming Zn or Se atoms by photons was high, typically more than 10%. The first observation reports the same wavelength dependence of the growth rate enhancement we observed in our laser-assisted MOMBE experiments (see section 3.5). The second and third observations suggest that a large number of electrons and/or holes were reaching the growing film surface. The pre-deposited layers

were undoped films of ZnSe that had been grown on GaAs substrates prior to the experiments in the which the ZnSe growth rates under laser irradiation were measured. It was proposed earlier by Yoshikawa et al. that photo-generated holes were participating in oxidation reactions of the adsorbed surface species [76]. An energy band diagram for the ZnSe/GaAs heterojunction was proposed; the ZnSe energy bands bend upward from the undoped n-type ZnSe near the GaAs substrate to more intrinsic ZnSe near the surface. Photo-generated holes would drift to the surface under the influence of the built-in field.

To verify that a large number of holes were present at the surface during the laser-assisted MOMBE experiments, an estimate of the number of holes which reached the surface is calculated. It is assumed that the number of holes that reached the surface per unit area per second was described by the equation,

$$h \cong \left(\frac{L_p}{\delta}\right)(1 - R)\eta\Phi \quad [\text{holes/cm}^2\cdot\text{s}] , \qquad \text{(Eq. 3.9)}$$

where L_p is the hole diffusion length, δ is the absorption depth of the Ar ion laser radiation, R is the reflectivity of the ZnSe surface, η is the quantum efficiency in converting photons to e-h pairs (assumed to be unity), and Φ is the incident photon flux. All the holes which were generated within the absorption depth δ will be assumed to have drifted in the direction of the surface due to the band-bending [76]. Converting the 180 mW/cm^2 laser power density to the number of $photons/cm^2\cdot s$ for 500 nm radiation yields $\Phi \cong 5x10^{17}$ $photons/cm^2\cdot s$. The increase in the growth rate on pre-deposited ZnSe layers during laser-assisted OMVPE [75] was observed to reach 90% of the maximum enhancement value when a 0.3 μm thick pre-deposited layer was used; 0.3 μm was close to the estimated penetration depth of the Ar ion laser. Therefore, δ will be assumed to be 0.3 μm in this calculation. The index of refraction of ZnSe is 2.66 for 458 nm radiation (Table 1.1) so R at normal incidence is approximately 0.2. The laser was incident at 45° to the substrate normal and the polarization of the laser at the substrate was not known,

therefore, a higher value for R of 0.5 will be used to be conservative in this estimate. Finally, the hole diffusion length is estimated from the relation,

$$L_p = \sqrt{D_p \tau_p} \ , \qquad \text{(Eq. 3.10)}$$

where D_p is estimated using the Einstein relationship $D_p = (kT/q)\mu_p$, and τ_p is the hole lifetime which will be approximated by the decay time of room temperature blue luminescence in ZnSe of ~ 100 picoseconds [77]. Using μ_p given in Table 1.1, L_p is ~ 0.1 μm. Therefore, the number of holes which reached the surface is estimated by equation (3.9) to have been approximately 8×10^{16} h/cm^2·s. The surface density of Zn and Se atoms is 6×10^{14} atoms/cm^2 which confirms that a large number of holes were available for surface reactions if they were required.

A kinetic model of laser-assisted MOMBE using DEZn and/or DESe sources has been developed. This model is based on proposed surface reactions which are consistent with the observed dependencies of the growth rate enhancement and suppression due to laser illumination discussed in section 3.5. Simple rate equations for desorption and incorporation of adsorbed surface species are derived from the surface reactions; only qualitative predictions were possible since the rate constants for the proposed reactions have not been determined. Enhancement and suppression of the growth rate for the various combinations of Zn and Se sources summarized in Table 3.7 can be explained by the model.

Two necessary conditions for growth rate enhancement were observed in the MOMBE experiments. The first condition was that e-h pairs were generated within the growing ZnSe layer by laser illumination. A band-bending model where holes are swept to the growing film surface [76] will be assumed in this model. The second requirement was that some form of metalorganic Zn was present at the surface. In addition to these necessary conditions for growth rate enhancement, it was observed that VI/II flow ratios

greater or less than unity would increase the GR enhancement. Based on these experimental observations, two possible reactions which might be occurring at the surface resulting in the growth rate enhancement are:

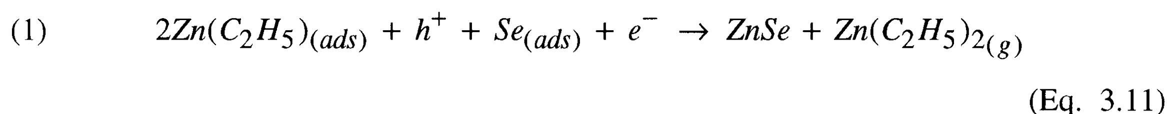

(1) $$2Zn(C_2H_5)_{(ads)} + h^+ + Se_{(ads)} + e^- \rightarrow ZnSe + Zn(C_2H_5)_{2(g)}$$

(Eq. 3.11)

or

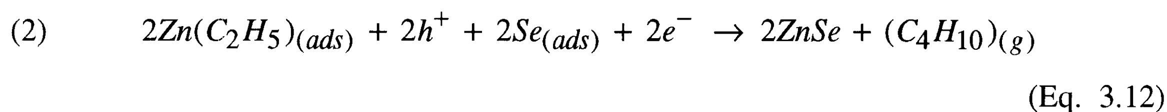

(2) $$2Zn(C_2H_5)_{(ads)} + 2h^+ + 2Se_{(ads)} + 2e^- \rightarrow 2ZnSe + (C_4H_{10})_{(g)}$$

(Eq. 3.12)

Equations (3.11) and (3.12) are bimolecular reactions where the zinc atom(s) are oxidized from the ethyl radical allowing them to incorporate into the lattice, while simultaneously removing the chemisorbed C_2H_5 through the formation of a volatile species. Monoethylzinc (MEZn), $Zn(C_2H_5)$, was the most likely form of metalorganic zinc at the surface since a bond was free for chemisorption to the surface, and the probability of DEZn physisorption on a hydrocarbon terminated surface was most likely low. A hole is required to oxidize the MEZn in reactions (1) and (2) and the adsorption of a Se on the positively charged surface is assumed to require an electron at the surface to maintain charge balance. Reaction (1) is the reverse reaction of DEZn decomposing to MEZn, which would normally occur at the surface in the absence of surface passivation by the ethyl radicals. A recombination of two chemisorbed ethyl radicals at the surface to form a volatile species such as C_4H_{10} (reaction (2)) is another possibility consistent with the experimental evidence. The actual reaction(s) leading to the formation of volatile ethyl species and the subsequent incorporation of zinc could not be determined using our experimental apparatus. One requirement for the reaction imposed by the observations of laser-assisted MOMBE shown in Table 3.7 is that the C_2H_5 desorption involve a a bimolecular reaction. The observation of a suppressed low growth rate when laser-assisted MOMBE was conducted using elemental zinc and cracked DESe was evidence

against direct desorption of (C_2H_5) induced by the laser. The Zn:Se flow ratio dependencies can only be accounted for by a bimolecular surface process.

The proposed reactions satisfy the necessary conditions for growth rate enhancement of an intermediate product of DEZn decomposition (MEZn) at the surface and the presence of photo-generated carries. Figure 3.8 is a schematic drawing of the reactions in equations (3.11-3.12). It should be noted that a MEZn molecule chemisorbed to a Se surface site is equivalent to an ethyl radical chemisorbed to a Zn site as is shown in Figure 3.8 by the circled ethyl radical. Rate equations for the zinc incorporation and the C_2H_5 desorption through the formation of a volatile species can be derived from reactions (1) and (2). Possible dependencies of the incorporation and desorption rates based on reactions (1) and (2) are,

$$R_{Inc}^{ZnSe} \propto k_1[MEZn]^2[h][e] \text{ or } k_2^{\frac{1}{2}}[MEZn][h][e] \qquad \text{(Eq. 3.13)}$$

$$R_{Des}^{C_2H_5} \propto k_1[MEZn]^2[h][e] \text{ or } k_2[MEZn]^2[h]^2[e]^2 \qquad \text{(Eq. 3.14)}$$

where k_1 and k_2 are the rate constants for reactions (1) and (2), respectively. The Zn incorporation rate is either linearly or quadratically proportional to the surface concentration of MEZn, and linearly dependent on the *e-h* concentration generated by the laser. Se is assumed to be arriving at the surface in a sufficiently large flux so that whenever a Zn atom is released in reactions (1) or (2), ZnSe is formed. The desorption rate of C_2H_5 which is a bimolecular desorption process in both reactions is proportional to the *square* of the MEZn surface concentration, and is either linearly or quadratically proportional to photon flux generating the *e-h* pairs.

The steady-state surface coverage of Zn, Se, and C_2H_5 (possibly MEZn on a Se site) has been hypothesized to be shifted to almost complete C_2H_5 coverage at the low temperatures of ZnSe growth [39-43]. The growth rate was the metal incorporation rate

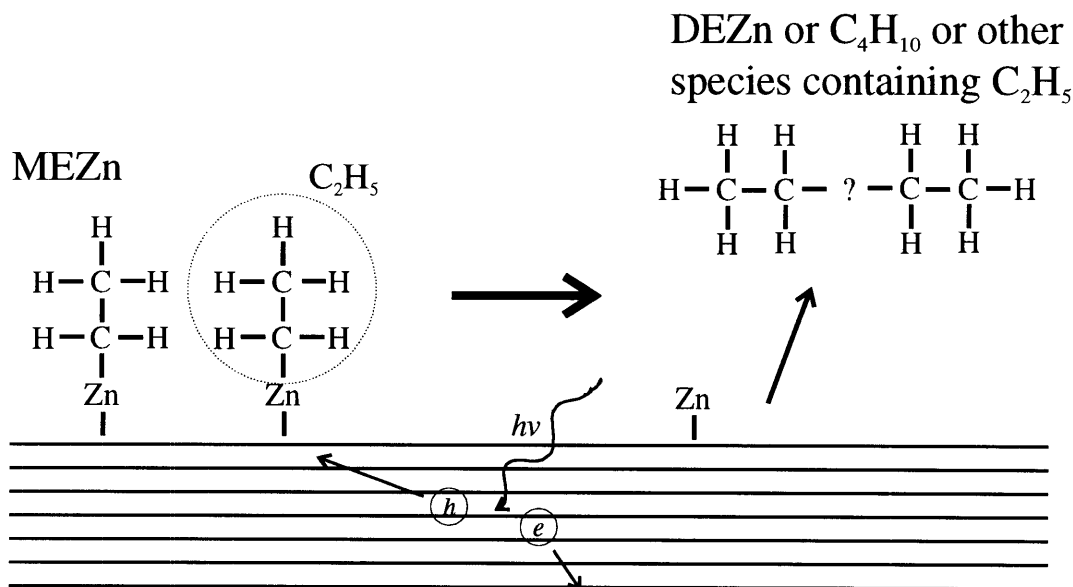

Figure 3.8 Drawing of possible surface reactions proposed to explain the observed necessary conditions for growth rate enhancement in the MOMBE of ZnSe using at least one diethyl metalorganic source gas. Holes generated by a laser or electron-beam drift to the surface and participate in anti-bonding reactions which free Zn metal sites and remove an ethyl radical through the formation of a volatile species containing C_2H_5 which subsequently desorbs.

minus the metal desorption rate. Surface passivation by ethyl radicals was speculated to reduce the sticking coefficient of incident Zn, Se, C_2H_5, and other hydrocarbons lowering the metal incorporation rates. Hence, growth was not mass-transport limited as expected, but instead was reaction-rate limited by the rate of desorption of the chemisorbed C_2H_5. Figure 3.2 suggests that the steady-state surface coverage of C_2H_5 was dominant over the growth temperatures investigated.

Laser illumination is proposed to increase both the rate of C_2H_5 desorption through the formation of volatile gaseous species, and the rate of Zn incorporation. Laser induced changes in the incorporation and desorption rates can qualitative explain the first six entries in Table 3.7 which summarize the effect laser illumination had on the MOMBE growth rate when a diethyl metalorganic source was used. Figure 3.9 shows the expected dependence of the Zn, Se, and C_2H_5 desorption rates (a), the incorporation rate of Zn (b), and the net growth rate (c), on the incident photon flux. The C_2H_5 desorption rate curves in Figure 3.9(a) are shown with curvature to represent the bimolecular desorption rate

process represented by equation (3.14). The Se desorption rate is shown to have a greater dependence on the laser intensity which is consistent with the speculation that suppression of the growth rate observed during MBE was due to enhanced Se desorption. The Zn desorption rate curve is assumed to have little or no slope. A Se incorporation rate curve is not shown in Figure 3.9(b) since Se was assumed to be available as needed at the surface to form ZnSe. Increasing growth rates with increasing concentrations of MEZn on the surface is reflected by a displacement of the C_2H_5 desorption rate curve to the left, and an increase in the photon flux dependence of the Zn metal incorporation rate. The six combinations of laser-assisted MOMBE growth using DEZn and/or DESe are now compared to the qualitative predictions of this model.

The case of no growth using uncracked DESe is simply the consequence that no Se atoms are available at the surface for incorporation without cracking. Suppression of the growth rate was observed for three combinations of sources: (*i*) cracked DEZn and cracked DESe, (*ii*) elemental Zn and cracked DESe, and (*iii*) cracked DMZn and cracked DESe. When the metalorganic of Zn is cracked, Zn arrives as atoms at the surface. In this case the desorption rate curve for C_2H_5 in Figure 3.9(a) and the incorporation rate curve in Figure 3.9(b) are the curves labeled by the number 1. Laser illumination has no effect on the Zn incorporation rate and little effect on the C_2H_5 desorption rate, but does enhance the desorption of Se. This should result in a decrease in the growth rate with increasing photon flux (laser intensity) as shown in Figure 3.9(c) by the curve labeled 1. This prediction agrees with the observed suppression in the GR shown in Table 3.7. Enhancement of the growth rate was observed when uncracked DEZn was used with either cracked DESe or elemental Se. Not cracking the DEZn during injection required that it be decomposed at the substrate surface, insuring a source of MEZn. The desorption rate for C_2H_5 and the Zn incorporation rate are represented by curves similar to those labeled 2 and 3, the actual curves would depend on how the growth conditions used

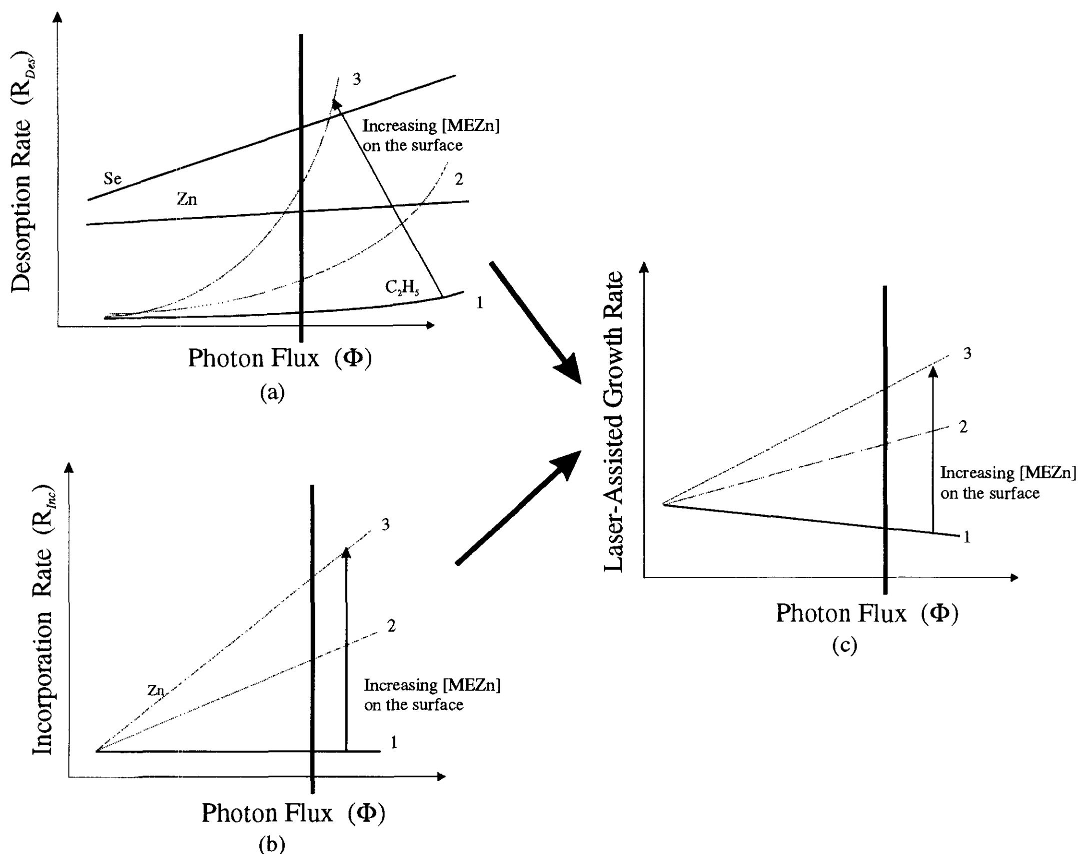

Figure 3.9 The top left figure (a) represents the proposed dependence of the Zn, Se, and C_2H_5 desorption rates on the photon flux Φ. The bottom left figure (b) is the postulated dependence of the Zn incorporation rate on laser photon flux. The laser-assisted growth rate which is the difference in the deposition rate (proportional to Zn incorporation) and the etching rate (proportional to re-evaporation of Se) is shown in figure (c) to the right.

influenced the surface concentration of MEZn. Laser illumination is seen to enhance the desorption of the ethyl radicals and to increase the rate of zinc incorporation. Se (and possibly Zn) also experiences an increase in its desorption rate, but the rate of increase in Zn incorporation should dominate the enhanced Se desorption. Combining the two effects should result in a net increase of the growth rate as shown by the curves numbered 2 or 3 in Figure 3.9(c), which was observed experimentally as shown in Table 3.7.

In summary, the kinetic model developed in this section, based on the rates of incorporation and desorption of the surface species of Zn, Se, and the ethyl radical (C_2H_5),

is able to qualitatively describe the effect laser illumination had on the MOMBE of ZnSe when at least one diethyl metalorganic source material was used.

3.9 ZnSe Film Characterization

Characterization of the structural and optical properties of ZnSe produced by MOMBE was critical to assess the viability of the growth method. Structural characterization of extended defects and the surface morphology was undertaken. The relative density of extended defects were qualitatively determined using the full width at half maximum (FWHM) of x-ray rocking-curve measurements. The surface morphology was examined by RHEED, Nomarski microscopy, and scanning electron microscopy (SEM) measurements. Optical characterization techniques such as photoluminescence (PL) are sensitive to low concentrations of impurities and crystalline defects in semiconductors. Photoluminescence was measured for all ZnSe thin films and was used as the first-order comparison standard amongst the films. The energy of a feature in the PL spectrum could be used to identify a specific impurity and/or defects within the film. The next three sections describe the standard characterization methods used to evaluate the ZnSe epilayers.

3.9.1 RHEED

Reflection high-energy electron diffraction (RHEED) is an *in-vacuo* technique to monitor the smoothness of a surface and the reconstructions that develop to minimize the surface free energy. RHEED is accomplished by directing an electron-beam at near glancing incidence to a film's surface. The electrons reflected off the surface strike a phosphor screen causing luminescence wherever one impinges. Electron interference generated by diffraction from periodic arrangements of atoms near the film surface produce patterns which depend on the orientational azimuth of the substrate. The shallow glancing angle limits the electron penetration depth to a few monolayers since the normal

component of the electrons' energy is small. Therefore, a RHEED image is the diffraction from lattice atoms just below the surface and from any periodic surface reconstruction. A further discussion of RHEED is presented in Appendix A.

Figure 3.10 are RHEED photographs representative of the ZnSe(100) surface observed after MOMBE growth. The long vertical streaks indicate that the film grew in a layer-by-layer Frank-van der Merwe mode. The dimmer streaks between the primary diffraction lines were due to periodic surface reconstructions. The faint two-fold reconstruction in the <010> crystalline azimuth and no reconstruction in the <011> azimuth imply that the final surface was terminated with Zn atoms, i.e. a Zn-rich surface reconstruction. Monitoring the surface reconstructions during growth yielded qualitative information about the surface stoichiometry *in-situ*, increasing our control over the growth conditions.

Figure 3.10 Post-growth RHEED photographs of a ZnSe(100) surface in the (a) <011> and (b) <010> azimuths. The two-fold reconstruction in the <010> azimuth and no reconstruction in the <011> direction indicates a Zn-rich surface.

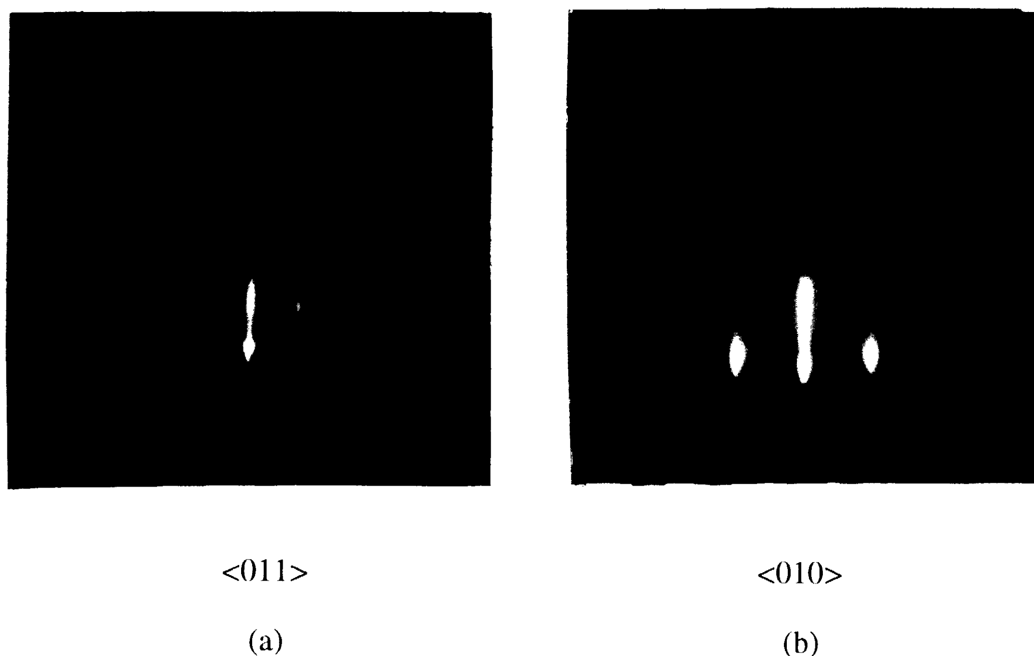

It was postulated in section 3.4 that the low growth rate was due to blockage of lattice sites by strongly chemisorbed ethyl radicals. Experimental evidence from X-ray photoelectron spectroscopy (XPS) studies of laser-induced desorption/decomposition of triethylgallium on GaAs(100) [78] suggest that the alkyl coverage will saturate at roughly one chemisorbed monolayer. The RHEED photographs shown in Figure 3.10 and the patterns observed on the phosphor screen during growth are of the same quality of published RHEED images from MBE of ZnSe. The patterns reflected the same underlying surface stoichiometry of a Zn- or Se-rich surface based on our setting of the flow(s) and/or flux(es) during experiments. The RHEED images appeared to be undisturbed by the hypothesized presence of large concentrations of ethyl radicals on the surface. The adsorbed ethyl radicals were most likely randomly arranged on the surface. Cross-linking of the hydrocarbons was unlikely since any free carbon bonds were probably tied up with hydrogen. If the electron-beam cross-section of the hydrocarbons was not too large, the electron-beam could constructively interfere from the underlying metal layer, although the reconstructions were probably reduced in intensity.

3.9.2 DCXRD

The ZnSe films grown without laser-assistance were normally 1000 Å thick or less. The lattice mismatch between ZnSe and GaAs at room temperature is 0.25 %. The critical thickness widely reported for a MBE grown film to remain pseudomorphic is 1500 Å [79]. The films were expected to be fully tetragonally distorted. Double crystal x-ray diffraction (DCXRD) measurements confirmed this expectation. A description of the DCXRD apparatus used in rocking curve measurements is given in Appendix B. Figure 3.11 is a rocking curve of a 1000 Å ZnSe film grown heteroepitaxially on GaAs. The 780 arcsecond angular separation between the substrate and layer peaks indicated the film was pseudomorphic. The 212 arcsecond FWHM was approximately 60-70 arcseconds larger than values reported for high quality MBE films of similar thickness [80]. The larger

values for the FWHM of MOMBE grown ZnSe might be a consequence of the difficulty in controlling the surface stoichiometry when the surface was experiencing blockage by ethyl radicals.

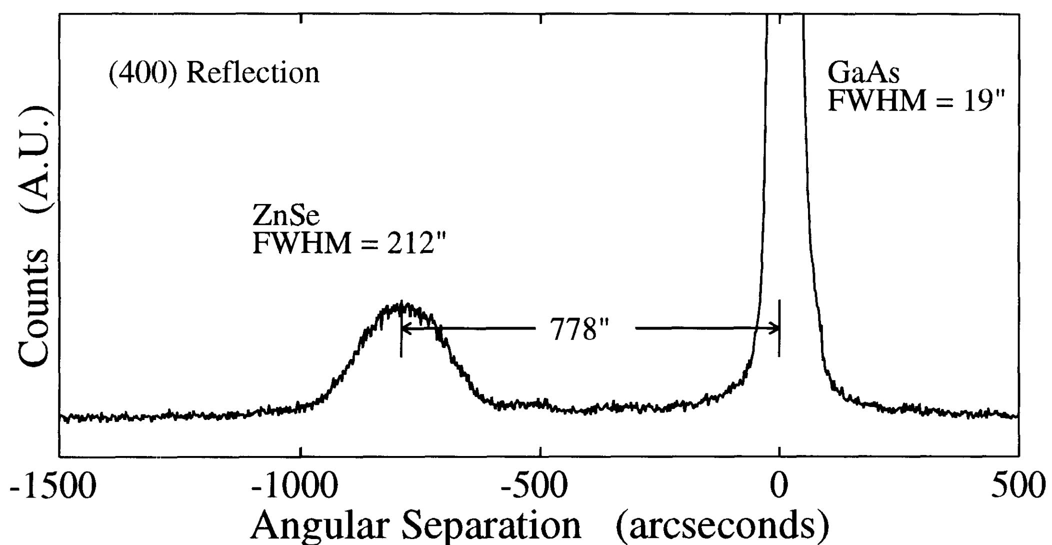

Figure 3.11 (400) x-ray reflection of a 1000 Å thick ZnSe film on GaAs. The angular separation of nearly 780 arcseconds indicates the film is pseudomorphic.

3.9.3 Photoluminescence

Optical characterization by photoluminescence (PL) was the primary characterization method used in this research. Appendix C contains a description of the PL apparatus, a more detailed description of the theory of photoluminescence, and a tabulation of common energy features seen in ZnSe photoluminescence spectra. A photoluminescence measurement records the intensity of electron-hole radiative recombination as a function of the emission wavelength. Electron-hole pairs are generated in the semiconductor by photo-excitation. The charge carriers rapidly thermalize ($\sim10^{-13}$ seconds) to the bandedge or inter-bandgap states. Subsequent recombination of the electrons and holes results in luminescence where the wavelength (photon energy) contains information about the initial electron and hole state energies. PL is usually measured at low temperatures where excitons have not been thermally dissociated; the existence of sharp excitonic features can greatly aid in identifying the energy of features and in providing qualitative information about the film quality.

3.9.3.1 Representative PL of a MOMBE Thin Film

A characteristic feature in nearly all the MOMBE photoluminescence was a broad defect band centered near 2.25 eV. Figure 3.12 contains low temperature (10 K) PL spectra for two regions of an epitaxial film. The luminescence in Figure 3.12(a) came from an unilluminated region while the spectra in (b) was measured in an area illuminated with 488 nm radiation during growth. The growth conditions of this film are given in Table 3.8. The sample was 1100 Å thick in (a) and 3400 Å thick in (b). The usual effect of laser illumination was to either reduce the deep level luminescence so that near-bandedge (NBE) excitonic features would radiate, or to increase the ratio of the intensity of the NBE to the deep level emission. The deep level is commonly observed in highly non-stoichiometric layers. The laser appears to alter the surface stoichiometry during growth so as to reduce the number of native defects in the film.

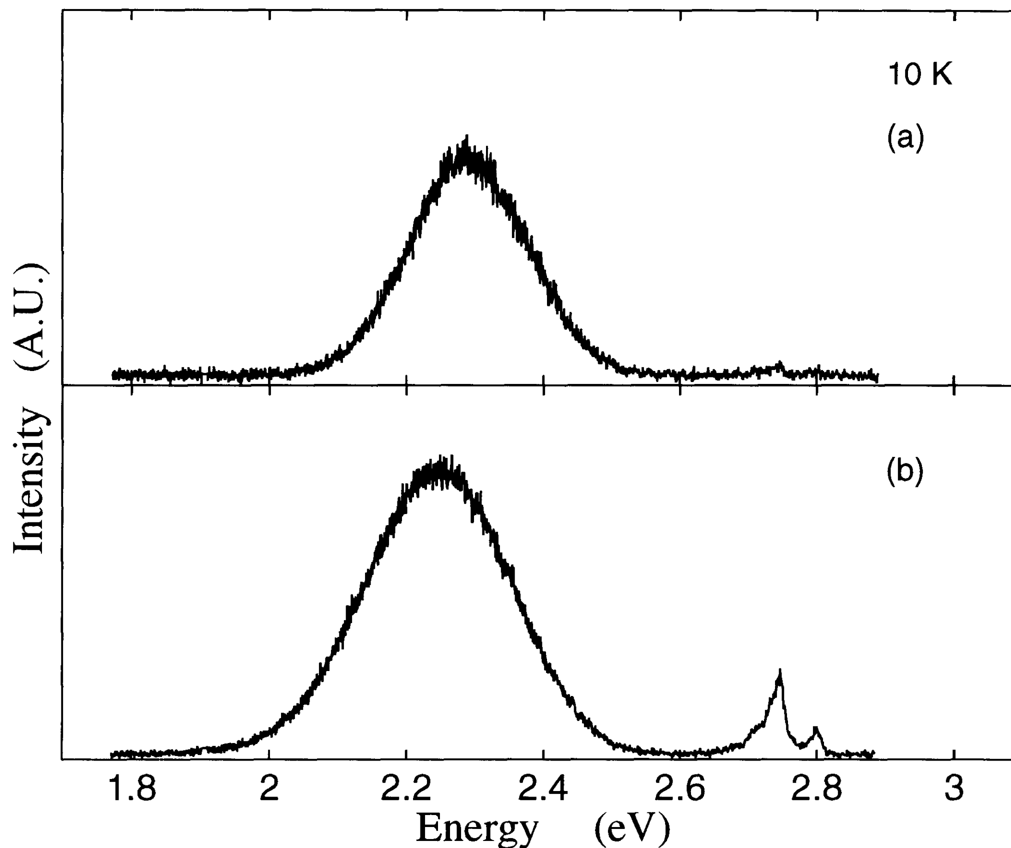

Figure 3.12 Low temperature (10 K) photoluminescence of a MOMBE thin film grown using DEZn and DESe sources. The PL spectrum in (a) is from an unilluminated region that was 1100 Å thick. The spectrum in (b) is from a laser illuminated region 3400 Å thick.

3.9.3.2 Laser Tuning of Stoichiometry

Generally the most prominent feature in the photoluminescence was deep level recombination. This PL is characteristic of highly non-stoichiometric ZnSe. The emphasis in the MOMBE research was to elucidate the origin of the low growth rate and to understand why laser illumination and electron-beam irradiation enhanced the growth rate. Hence, setting the gas flow ratios and/or oven fluxes to obtain optimum PL was not the first priority. In fact, control of the surface stoichiometry via gas flows was probably limited, since laser or electron-beam growth rate enhancement required partially

undissociated zinc metalorganics on the surface, implying the postulated site blockage by ethyl radicals promoted a Zn deficient surface stoichiometry.

In Figure 3.13 the modification of the surface stoichiometry by the laser is dramatically evident. The growth conditions are given in Table 3.8. Figure 3.13(a) is the PL of a 1100 Å thick unilluminated area which was dominated by deep level recombination which is speculated to be caused by zinc vacancy complexes. The region that was illuminated by 458 nm radiation during growth (5500 Å thick) shown in Figure 3.13(b) exhibits an intense donor-bound exciton peak at 2.799 eV, and almost no deep level luminescence. A

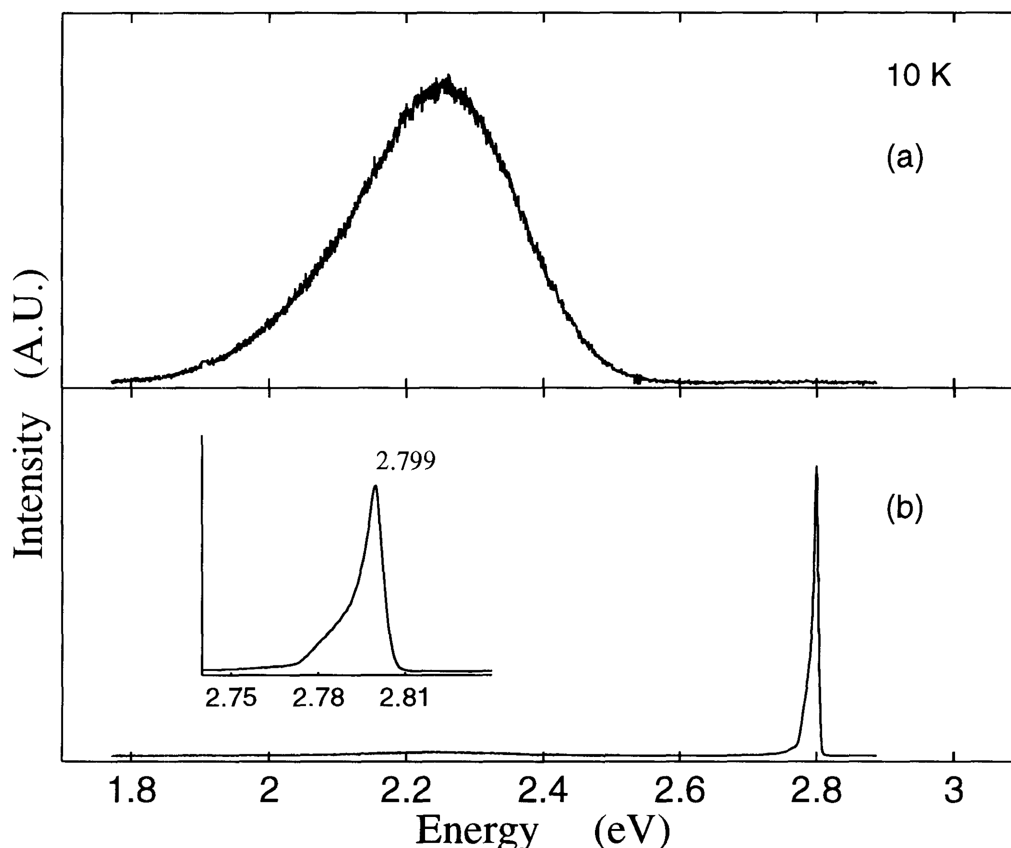

Figure 3.13 Low temperature photoluminescence illustrating tuning of stoichiometry by laser illumination. The spectrum in (a) is dominated by deep level recombination. Laser illumination was observed to dramatically improve the optical properties of the ZnSe film as shown in (b) where the PL spectrum is now dominated by an exciton feature in the near-bandedge.

small blue-shift in the donor-bound exciton peak energy from the bulk ZnSe value was likely for the 5500 Å thick film which had undergone some relaxation of the strain through the formation of misfit dislocations. The donor-bound exciton could be one of several catalogued by Dean et al. [81] (also see Appendix C). Chlorine is suspected to be the impurity since it is a possible contaminant in DESe, and the energy of 2.799 eV is within the ±1 meV resolution of the spectrometer and the slight blue-shift in energy due to residual compressive strain.

3.9.3.3 MBE PL

Molecular beam epitaxy of ZnSe was performed to provide a comparison for the MOMBE growths. Figure 3.14 is the PL of a MBE film exhibiting no deep level luminescence and dominant NBE emission of free- and donor-bound excitons. The growth conditions for this MBE grown film are given in Table 3.8. The insert is a more detailed view of the near-bandedge region showing a free-exciton at 2.807 eV and a donor-bound exciton with

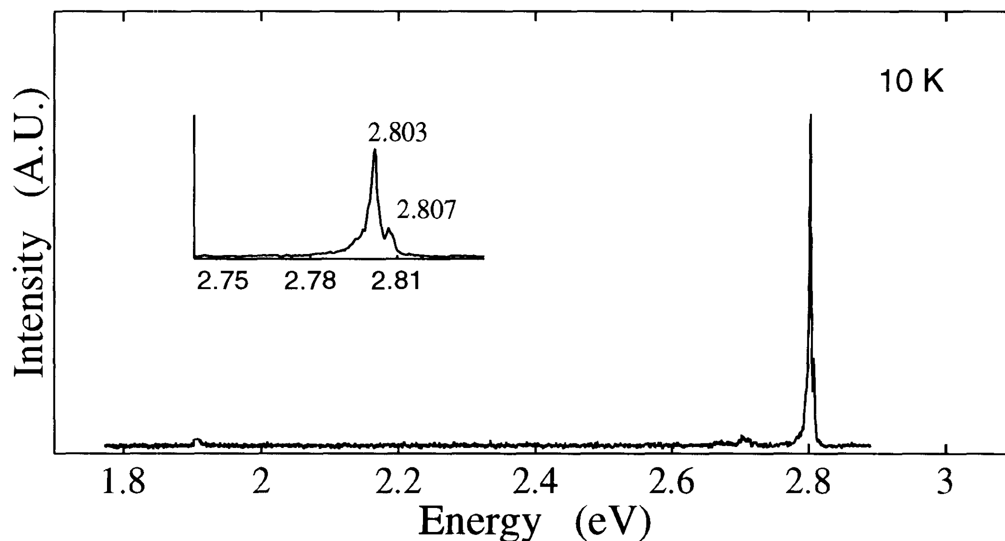

Figure 3.14 Low temperature (10 K) PL of a ZnSe film grown by MBE. The intense exciton features in the near-bandedge and absence of deep level recombination indicate good film quality.

Table 3.8 Growth conditions of the films that were characterized by photoluminescence in Figures 3.12-14.

PL		Parameter		Value
Typical MOMBE	(ZnSe #42)			
		Substrate Temperature	(°C)	320
		DESe (800 °C)	(sccm)	1.5
		DEZn (50 °C)	(sccm)	0.5
Laser Tuning	(ZnSe #37)			
		Substrate Temperature	(°C)	310
		DESe (800 °C)	(sccm)	2.5
		DEZn (50 °C)	(sccm)	0.5
MBE	(ZnSe #68)			
		Substrate Temperature	(°C)	320
		Se Flux	(Å/s)	0.2
		Zn Flux	(Å/s)	0.18

an energy of 2.803 eV. The film was pseudomorphic at the 1200 Å thickness so the strain blue-shifted the energies by approximately 6 meV (see Appendix C). As in the previous example, the donor-bound exciton was attributed to chlorine. This was the photoluminescence of the first film grown by MBE. The 'clean' PL spectrum suggested that metalorganic source gases were compatible with an MBE system since no 'memory' effect from previous MOMBE growths was evident in the PL of the MBE grown film.

3.10 Summary

ZnSe has been grown by the method of metalorganic molecular beam epitaxy. The growth rate during MOMBE was unusually low at less than 400 Å/hr whenever diethylzinc and/or diethylselenium were used. MOMBE experiments using mixed sources where the diethylzinc or the diethylselenium were replaced by DMZn/elemental zinc or elemental selenium, respectively, confirmed that ethyl radicals were contributing to the low growth rate. It was hypothesized that surface sites for incorporation of the metal atoms were saturated by chemisorbed ethyl radicals, thus limiting the growth rate. In a

parallel investigation of laser-assisted MOMBE, it was observed that laser illumination of the substrate during growth would reduce the ethyl radical surface passivation phenomenon under appropriate growth conditions. Electron-beam irradiation of the substrate using the RHEED gun was found to have qualitatively the same effect on the growth rate as the laser beam. Two necessary conditions were required during laser-assisted MOMBE to produce an enhancement in the growth rate when an ethyl source was employed: (*i*) photons having energy sufficient to generate electron-hole pairs had to illuminate the surface, and (*ii*) some form of metalorganic zinc (speculated to be monoethylzinc) was required to be absorbed on the surface. Under these conditions of growth, the measured growth rates of regions illuminated by the laser were increased by as much as a factor of 15 over the unilluminated growth rates. It is hypothesized that the laser illumination or electron-beam irradiation created holes which drifted to the surface and participated in antibonding reactions, which led to the removal of the ethyl radicals, and allowed more Zn to incorporate into the lattice which increased the growth rate. A model for the laser-assisted growth rate enhancement was developed in section 3.8 which could qualitatively explain what was observed experimentally when laser-assisted MOMBE was performed using at least one diethyl metalorganic source.

The quality of the undoped ZnSe grown by MOMBE was strongly dependent on the surface stoichiometry which existed during growth. Low temperature photoluminescence measurements of most films were dominated by a deep luminescence band centered near 2.25 eV. This defect band has been attributed to highly nonstoichiometric growth, and is speculated to be due to zinc vacancy complexes in the MOMBE films. The laser was observed to tune the surface stoichiometry by enhancing the incorporation of zinc atoms, which was being inhibited by the chemisorbed ethyl radicals. X-ray diffraction rocking curves of fully strained ZnSe on GaAs substrates had FWHMs of approximately 220 arc

seconds. MBE grown films of similar thickness have FWHMs in the 150 arc seconds range, indicating a more defective internal structure of the MOMBE films.

Control of the surface stoichiometry by adjusting the metalorganic gas flows was greatly reduced when surface passivation of the metal incorporation sites by the ethyl radicals occurred, resulting in a degradation of the optical and structural properties of the films. Therefore, MOMBE growth of ZnSe under conditions which result in ethyl radical surface passivation is not generally recommended. An exception to this recommendation are applications where the selective deposition of ZnSe may be required. The large difference in the growth rates that have been observed between regions irradiated by a laser or an electron-beam and regions which were not irradiated, might be exploited in selective area epitaxy. It may be possible to optimize the growth conditions such that growth only occurs in a laser illuminated or electron-beam irradiated region. Further experiments are required to test if a growth rate near a micron per hour can be achieved without using laser assistance through modifications of the DESe cracker or the addition of atomic hydrogen during growth. If a usable growth rate can be obtained, it will then be possible to evaluate whether MOMBE of ZnSe using DEZn and DESe is a viable alternative to the more established methods of MBE and OMVPE.

Chapter 4

Gas Source MBE of ZnSe

ZnSe was grown by the method of gas source molecular beam epitaxy (GSMBE) using elemental zinc and hydrogen selenide (H_2Se) as source materials. The use of GSMBE is a new approach to the growth of ZnSe [44,82 ,83]. Heteroepitaxy on GaAs substrates resulted in high quality ZnSe as indicated by intense low temperature photoluminescence dominated by shallow donor-bound exciton transitions.

An advantage of GSMBE is the higher purity of the source materials in comparison to the metalorganics used in MOMBE. MBE grade zinc of six nines purity and H_2Se with impurities at the ppm level were used in the experiments. A drawback of GSMBE is the toxicity of H_2Se which requires the installation of expensive safety equipment and the implementation of special handling procedures, raising the cost of this method.

4.1 GSMBE Growth

Growth of ZnSe by GSMBE was 'MBE-like' in that the constituent elements of Zn and Se reached the substrate as individual metal atoms, or clusters of metal atoms. Thermal dissociation of H_2Se in the high-temperature gas cracker separated the hydrogen from the selenium; the dominant metal species formed has been reported to be Se_2 [84]. An important difference from MBE growth was that during GSMBE, by-products of cracking were also incident on the growing film surface. The cracking by-product with the highest partial pressure detected by the QMS was molecular hydrogen. Hydrogen incorporation in semiconductors, referred to as hydrogenation, is known to occur during certain growth conditions [85]. The presence of hydrogen in a semiconductor can be

detected by a direct measurement such as secondary ion mass spectroscopy (SIMS) if hydrogen is present in sufficiently high concentrations. Hydrogen in a semiconductor may also be inferred if the expected electrical and optical properties of the semiconductor are modified in ways characteristic of hydrogenation. SIMS analysis of the undoped GSMBE grown ZnSe was inconclusive concerning hydrogenation. Hydrogen was not detected in undoped ZnSe at concentrations greater than 5×10^{17} atoms/cm^3, the approximate detection limit for hydrogen in the SIMS measurements. Hydrogen may be present in lower concentrations.

4.1.1 Growth Conditions

The growth conditions for GSMBE were similar to those used in MOMBE [44]. The primary difference was that metalorganic zinc sources were replaced by solid zinc, which was sublimated from a Knudsen cell. As of this writing, only three laser-assisted growth experiments have been performed during GSMBE. The growth rate (GR) was measurably suppressed in all three experiments. Growth rate suppression was expected for 'MBE-like' growth based on our previous studies which examined the effect of laser illumination during MOMBE, summarized in Table 3.7. Additional experiments of laser-assisted GSMBE may be pursued in the future if a means to suppress spot formation on the

Table 4.1 The growth parameter space investigated for GSMBE of ZnSe using H_2Se and elemental Se sources.

Variable		Values	
	Minimum	Maximum	Typical
Substrate Temperature (°C)	245	395	270
H_2Se Flow Rate (sccm)	1.0	2.4	1.2 or 2.2
H_2Se Cracker Temp. (°C)	600	1100	1000
Zn Effusion Cell Temp. (°C)	297	322	304 or 312
Zn Flux (Average) (Å/s)	0.55	2.41	0.7 or 1.0
Growth Time (hr)	3	6.67	4

viewport, which was more severe than spot formation during MOMBE, can be found.

The growth parameter space investigated is presented in Table 4.1. The range of values of the variables are indicated in the minimum and maximum value columns. The typical values listed were the most common experimental conditions used.

4.1.2 H_2Se Cracking

The H_2Se required cracking due to the strength of the hydrogen-metal bond. Table 3.1 indicates the average H-Se bond energy is 66 kcal/mol. H_2Se cracking experiments were conducted using a QMS to record the mass spectrum of the species emitted from the cracker at different cracker temperatures. Analysis of the spectra indicated that H_2Se began to dissociate at temperatures greater than 700 °C; at this temperature the H_2 peak was approximately the same magnitude as the H_2Se peak in the mass spectrum. Figure 4.1

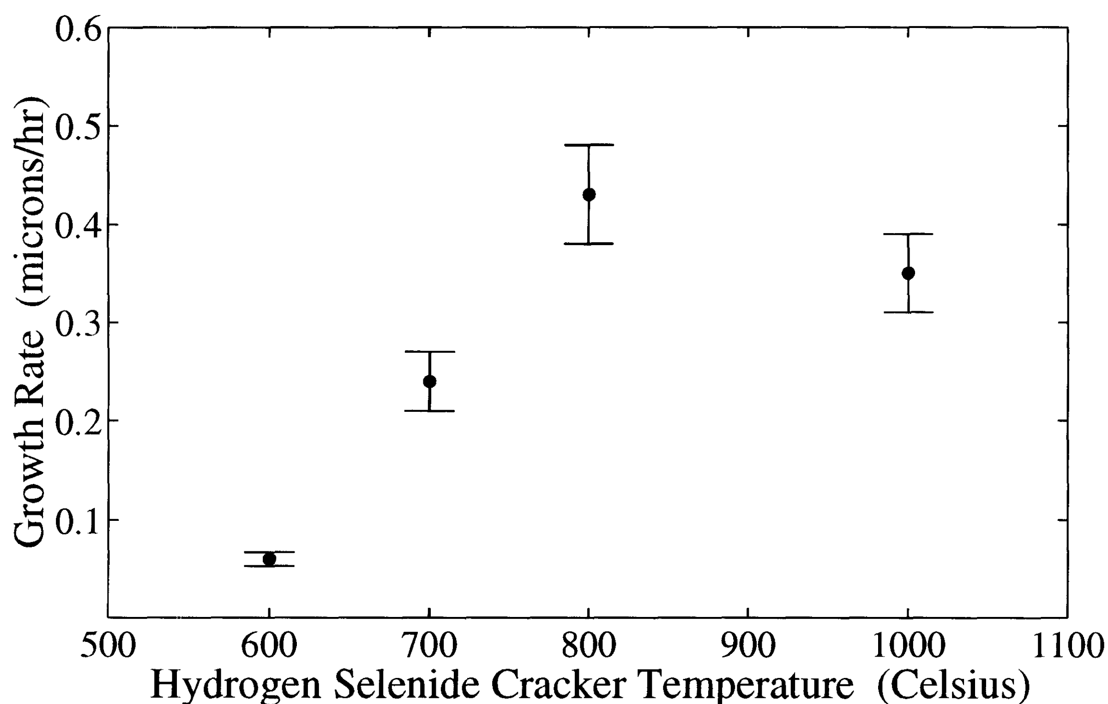

Figure 4.1 Growth rate versus the H_2Se cracking temperature illustrating the approximate 700 °C threshold for growth to occur. The growth conditions for these experiments are summarized in Table 4.2.

Table 4.2 Growth conditions of the ZnSe films grown by GSMBE which produced the data shown in Figure 4.1.

Variable	Units	Value
Substrate Temperature	(°C)	270
H_2Se Flow Rate	(sccm)	1.7
Zn Effusion Cell Temperature	(°C)	307-309
Average Zn Flux	(Å/s)	~ 1.0
Growth Time	(hr)	3

shows the growth rate versus the hydrogen selenide cracker temperature. The figure indicates an approximate threshold H_2Se cracker temperature of 700 °C for growth to occur. The apparent peak in the growth rate at 800 °C may be a consequence of the unstable Zn flux which was described Section 3.1. Error bars are included for growth rate values, reflecting the uncertainties in the Zn flux and the H_2Se flow rate. The determination of the uncertainty in the growth rate is described in the next section. No error bars are given for the cracker temperature since the PID controller regulated the temperature to within ±1 °C. Table 4.2 summarizes the growth conditions of the films from which the data in Figure 4.1 was produced.

4.1.3 Estimate of Growth Rate Uncertainty

The GSMBE growth rate will be shown in Section 4.1.4 to be dependent on the H_2Se flow rate, the Zn beam flux, and the substrate temperature. An estimate of the GR uncertainty is possible based on the uncertainties in these independent variables. The growth rate uncertainty calculations are carried out in Appendix D. The results of these calculations are summarized in Table 4.3. GSMBE will be shown in Section 4.1.4 to be a mass-transport limited growth process, so the GR was linearly proportional to the incident fluxes. It was demonstrated in Appendix D that the percentage uncertainty in a source flux caused the same percentage uncertainty in the growth rate. Since ZnSe is a binary

Table 4.3 Percentage uncertainty in growth rate ($\Delta GR/GR$) for different growth conditions. Entries are given as the percentage uncertainty in the growth rate caused by the uncertainty in the variables listed. Uncertainty calculations are carried out in Appendix D.

Variable	Surface Stoichiometry:	Se-Limited	(ΔGR/GR) Zn-Limited	1:1
Substrate Temperature		± 2%	± 2%	± 2%
H_2Se Flow Rate		± 6%	*	± 6%
Zn Effusion Cell Flux		*	± 9%	± 9%
	Total (ΔGR/GR)	± 8%	11%	± 17%

* No contribution to GR uncertainty with the indicated surface stoichiometry.

compound, the growth rate was limited by the flux which contained the fewest atoms of Zn or Se to incorporate into the film surface, assuming similar sticking coefficients for the Zn and Se. The majority of the films were grown under conditions where one element was mass-transport limited, i.e. Zn- or Se-rich growth. Hence, the uncertainty in the GR was affected by the uncertainty in the flux of the mass-transport limited element only; excess Zn or Se arriving at the surface did not affect the growth rate because Zn or Se coverage beyond one monolayer would desorb. When the ratio of the Zn to Se on the surface was nearly unity as determined by RHEED reconstructions, the uncertainty in both fluxes was assumed significant. The uncertainty in the Zn flux was greater than the uncertainty in the H_2Se flow, hence, Zn-limited growth was subject to a greater variance in the growth rate as shown in Table 4.3.

4.1.4 Growth Rate Dependencies

In the next two sections it will be shown that GSMBE exhibits the same dependence on the growth variables as molecular beam epitaxial growth of ZnSe.

4.1.4.1 Substrate Temperature

Figure 4.2 shows that the growth rate was dependent on the growth (substrate) temperature. The growth rate decreased at higher growth temperatures due to re-evaporation of the Zn and Se. ZnSe growth does not require an overpressure in the anion species as is common in III-V materials growth because of the similar sticking coefficient of both constituents. The higher growth rate at lower substrate temperatures is also observed in MBE of ZnSe. The solid points and open circles correspond to different sets of growth conditions. The solid point data was measured from films grown with a 2.5 sccm H_2Se flow rate and an average Zn flux of 0.7 Å/s as measured by the quartz crystal oscillator; the surface stoichiometry during growth was Se-rich as determined from the RHEED reconstructions. The open circle data were grown using a 1.7 sccm H_2Se flow

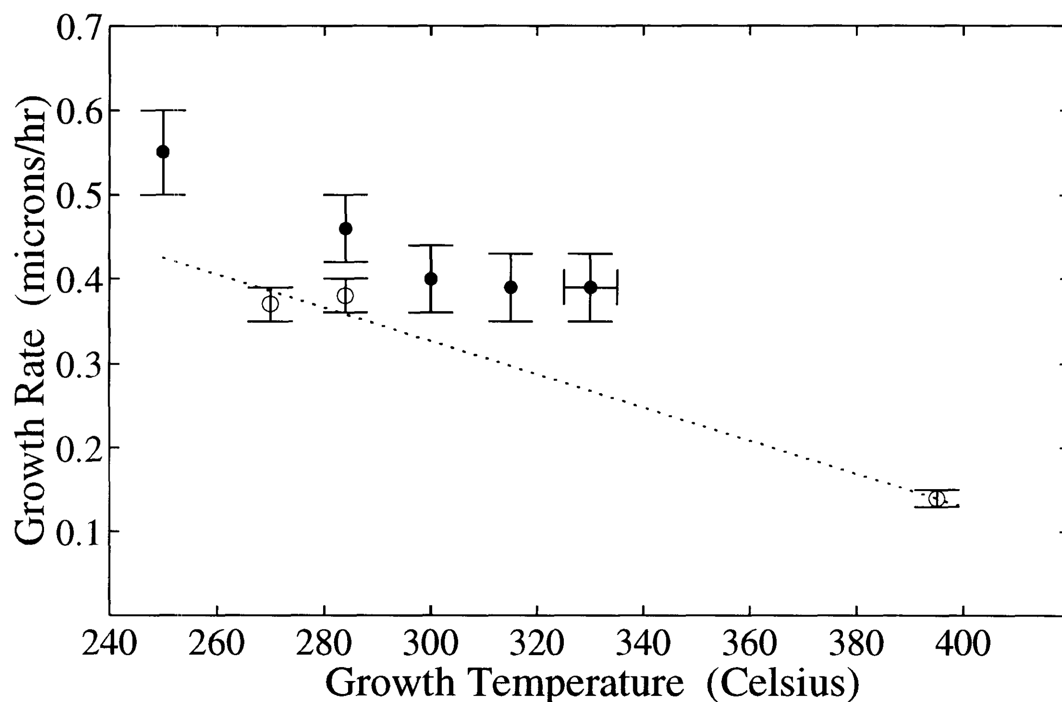

Figure 4.2 Dependence of the growth rate on the growth temperature. The growth conditions of the films whose growth rates are represented by the solid points were grown with a H_2Se flow rate of 2.5 sccm and an average Zn flux of 0.7 Å/s. The H_2Se flow rate was 1.7 sccm and the average Zn flux was 1.0 Å/s for the data represented by the open circles. The dotted line is a linear approximation to the growth rate temperature dependence.

rate and 1.0 Å/s average Zn flux, which resulted in a Zn-rich surface during growth. The error bars are larger for the solid point data reflecting the greater uncertainty in the growth rate under Zn-limited growth conditions. A representative error bar indicating the uncertainty in the temperature measurement is also shown.

4.1.4.2 H_2Se Flow and Zn Flux

GSMBE was observed to be a mass-transport controlled growth process. The growth rate increased with greater H_2Se flow or Zn flux when the growth was Se-limited or Zn-limited, respectively. Figure 4.3 illustrates the linear dependence of the growth rate on the H_2Se flow rate. Table 4.4 summarizes the common growth conditions for the data shown in Figure 4.3.

The ratio of the H_2Se flow rate to the Zn flux to produce a 1:1 surface stoichiometry

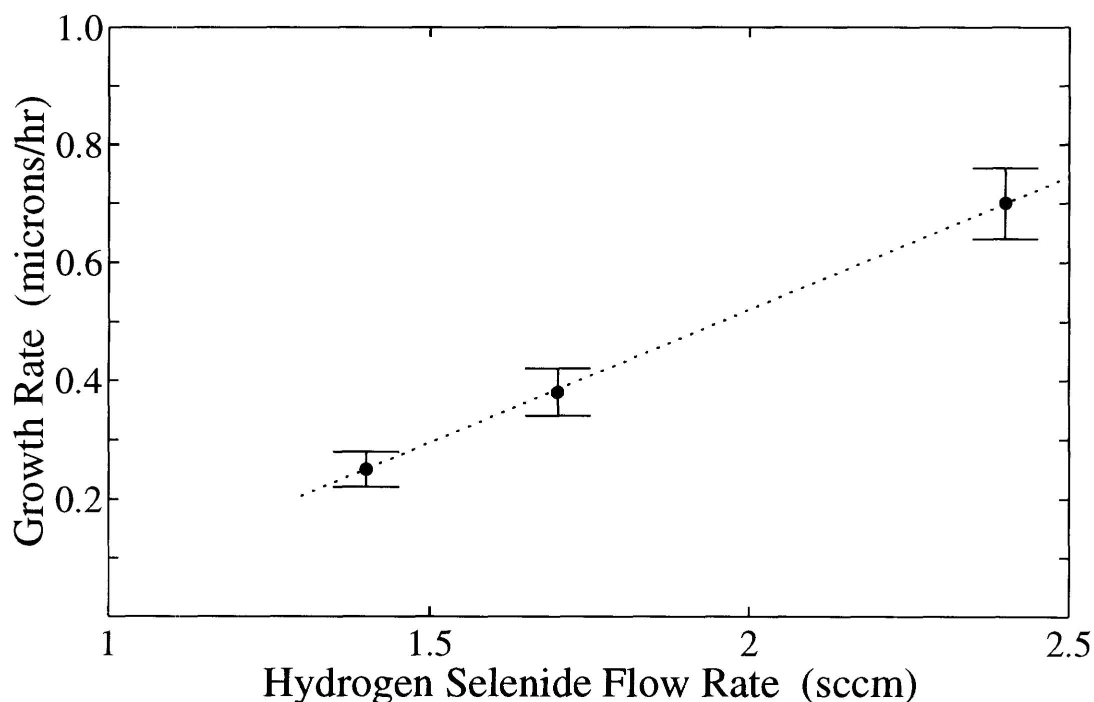

Figure 4.3 Growth rate is a linear function of the H_2Se flow rate indicating that arrival of Se to surface is limiting the growth rate.

Table 4.4 Summary of the common growth conditions of the experiments from which Figure 4.3 was produced.

Growth Variable		Value
Substrate Temperature	(°C)	285-290
H_2Se Cracker Temperature	(°C)	1000
Surface Stoichiometry		Zn-rich
Growth Time	(hr)	3

was estimated from the RHEED reconstructions observed during growth. A 1.8-2.0 sccm H_2Se flow rate (cracked at 1000 °C) was required for every 1.0 Å/s of Zn flux. Therefore, the Se:Zn source ratio for a 1:1 surface stoichiometry during growth was approximately 1.9±1 (sccm)/Å/s. A good correlation between the Se:Zn source ratio and the surface stoichiometry determined from RHEED reconstructions was observed. When the Se:Zn source ratio was ≤ 1.7, the surface was Zn-rich. Conversely, when the source ratio was ≥ 2.1, the RHEED reconstructions indicated Se-rich surfaces.

4.2 Characterization of GSMBE films

The surface morphology and structural properties of the undoped ZnSe were characterized by Nomarski spectroscopy, scanning electron microscopy (SEM), and x-ray diffraction rocking curve measurements. During growth the film surface was analyzed *in-situ* by RHEED. The optical properties were investigated by low temperature photoluminescence. Electrical characterization was possible since the films were normally several microns thick. Hall effect and capacitance-voltage (C-V) measurements were performed to characterize the electrical properties.

4.2.1 Structural Characterization

X-ray diffraction rocking curve measurements of the ZnSe grown heteroepitaxially on GaAs by GSMBE indicated good structural quality. The full width at half maximum

(FWHM) of the ZnSe (400) reflection peak was in the range of 180-220 arcseconds [44], values comparable to the FWHMs of ZnSe grown by MBE.

4.2.1.1 RHEED

Representative RHEED photographs of the observed post-growth reconstruction patterns are displayed in Figure 4.4. The faint two-fold reconstruction in the <011> crystal azimuth (a), and no reconstruction in the <010> direction (b), indicate the final surface was slightly Se-rich, the same stoichiometry that was observed during the growth of the film. The streaky lines suggest the surface at completion of growth was smooth to within a few monolayers. The reconstruction patterns reflected the same surface stoichiometries observed in MBE of ZnSe; hydrogen present at the surface apparently did not alter the surface free energy sufficiently to modify the surface reconstructions.

Figure 4.4 Photographs of post-growth RHEED images. The faint two-fold reconstruction in the <011> azimuth (a), and no reconstruction in the <010> direction (b) indicate the final surface was slightly Se-rich.

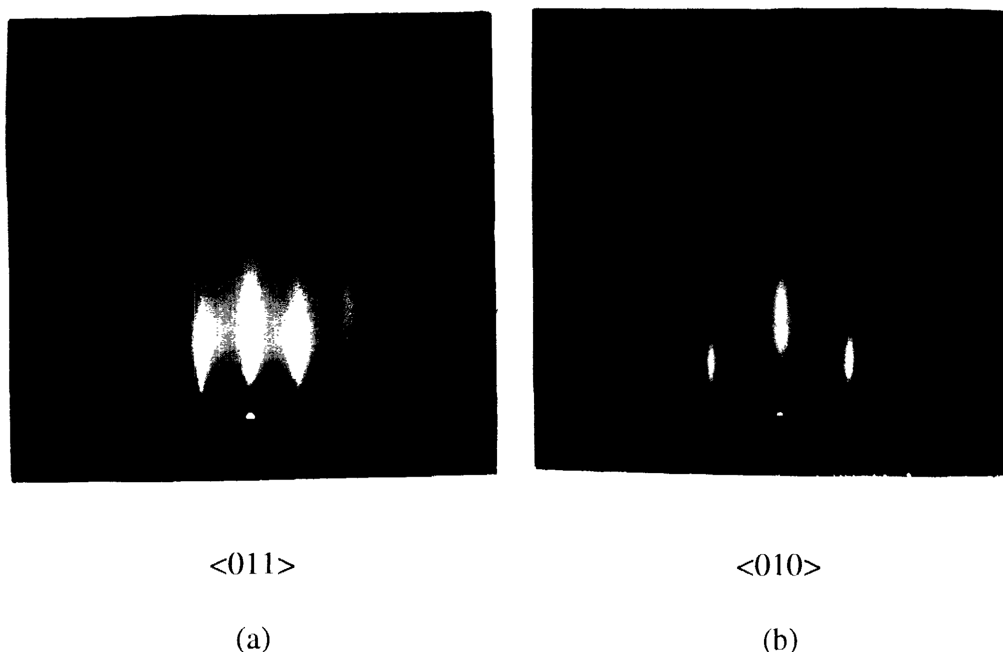

4.2.1.2 Nomarski and Scanning Electron Microscopy

Nomarski microscopy and scanning electron microscopy (SEM) were used to analyze the surface morphology. Nomarski photographs taken at a magnification of 1000x revealed the film surfaces to be featureless in almost all cases. Films that were grown at the lowest substrate temperatures, however, had surfaces that appeared slightly hazy. Scanning electron microscopy was used to examine the surfaces on a finer scale. Figure 4.5 is a SEM image taken at 100,000x magnification that was representative of the surface morphology of most undoped films. The surface is seen to be featureless at this high magnification. The white region in the lower left corner of the image is a dust particle which the SEM operator used to bring the surface in proper focus.

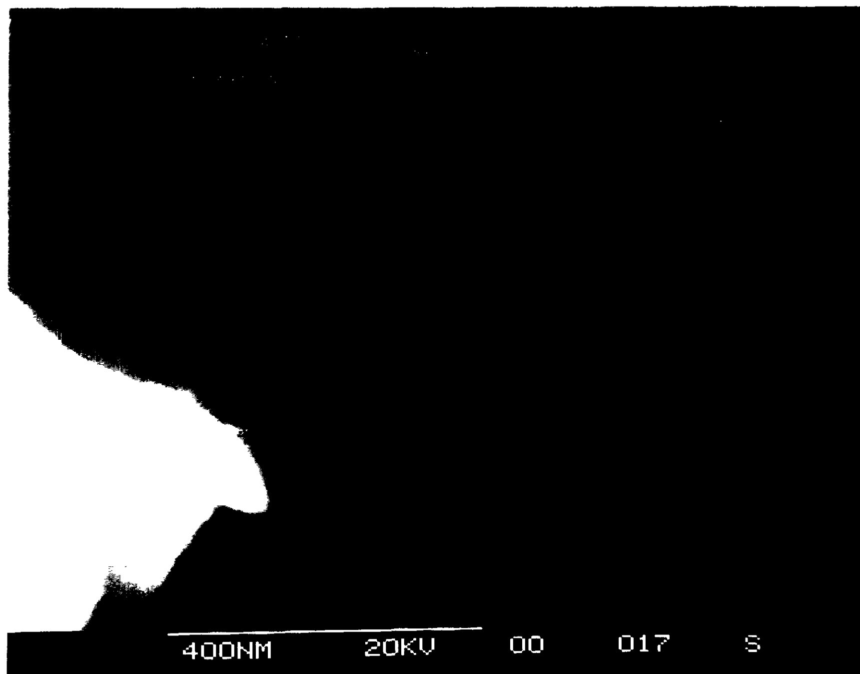

Figure 4.5 SEM image of the typical surface morphology of ZnSe films grown by GSMBE. The scale is indicated by the line on the bottom of the photograph. The white region is a dust particle which was used as an aid in focusing.

The slightly hazy surfaces of films grown at lower temperatures were observed to have a 'sandpaper-like' texture when viewed under a Nomarski microscope at 1000x magnification. Figure 4.6 is a photograph of a film grown under Zn-rich conditions where the substrate temperature dropped below 250 °C. The Zn flux and H_2Se flow rate were similar to those of other films which had featureless surface morphologies. An SEM image of the same hazy surface film is shown in Figure 4.7. The surface at 33,000x magnification appears to be covered with pits that have three-fold symmetry. The origin of these features is unknown, but it is speculated that the low growth temperature which reduced the surface mobility of the Zn and Se atoms might have contributed to the

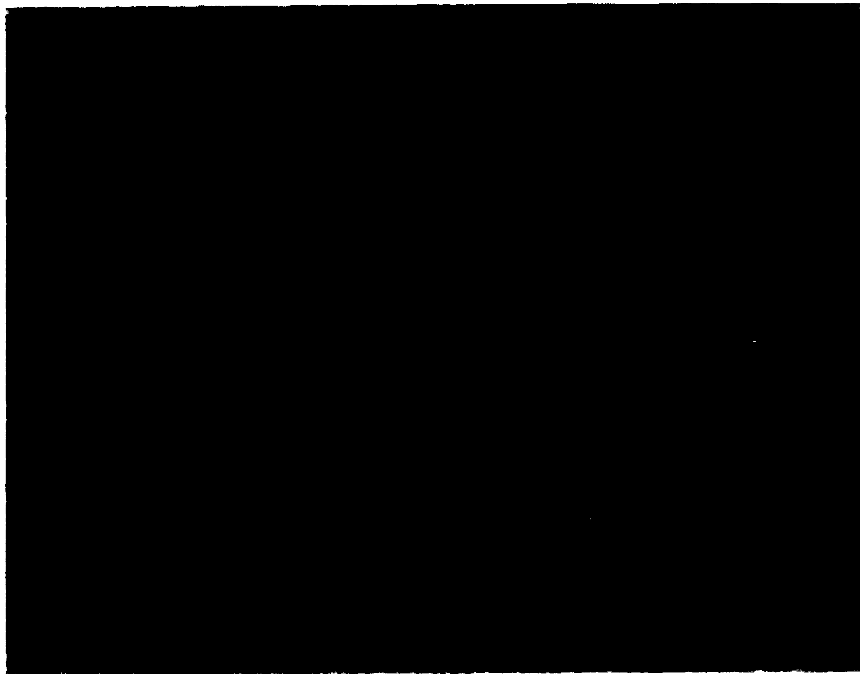

Figure 4.6 Photograph taken using the Nomarski microscope of a film which was grown at an approximate substrate temperature of 250 °C. Magnification is 1000x.

formation of these defects. The surface morphology observed in Figure 4.7 was an exception, most GSMBE ZnSe films were grown at higher substrate temperatures and had surface morphologies similar to Figure 4.5.

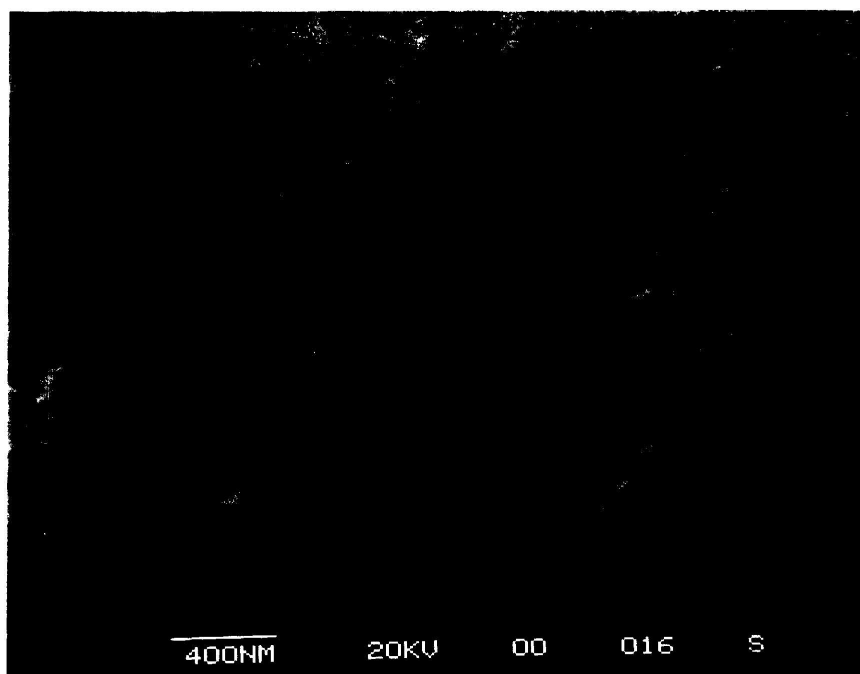

Figure 4.7 SEM image of a ZnSe film where the substrate temperature fell below 250 °C during growth. Pits with three-fold symmetry are visible on the surface. The scale is indicated by the white line at the bottom of the photograph.

4.2.2 Photoluminescence

The optical properties of the ZnSe epitaxial layers were investigated by photoluminescence. Optical excitation was produced by a focused He-Cd laser beam resulting in a power density of approximately 300 mW/cm^2. Appendix C contains a more detailed description of photoluminescence spectroscopy. Figure 4.8 shows a series of 10 K photoluminescence measurements of films grown at different substrate temperatures, but otherwise similar growth conditions. The common growth conditions of these films are listed in Table 4.5. All the films were greater than 1 μm in thickness. The PL at each growth temperature investigated was dominated by an intense donor-bound exciton having

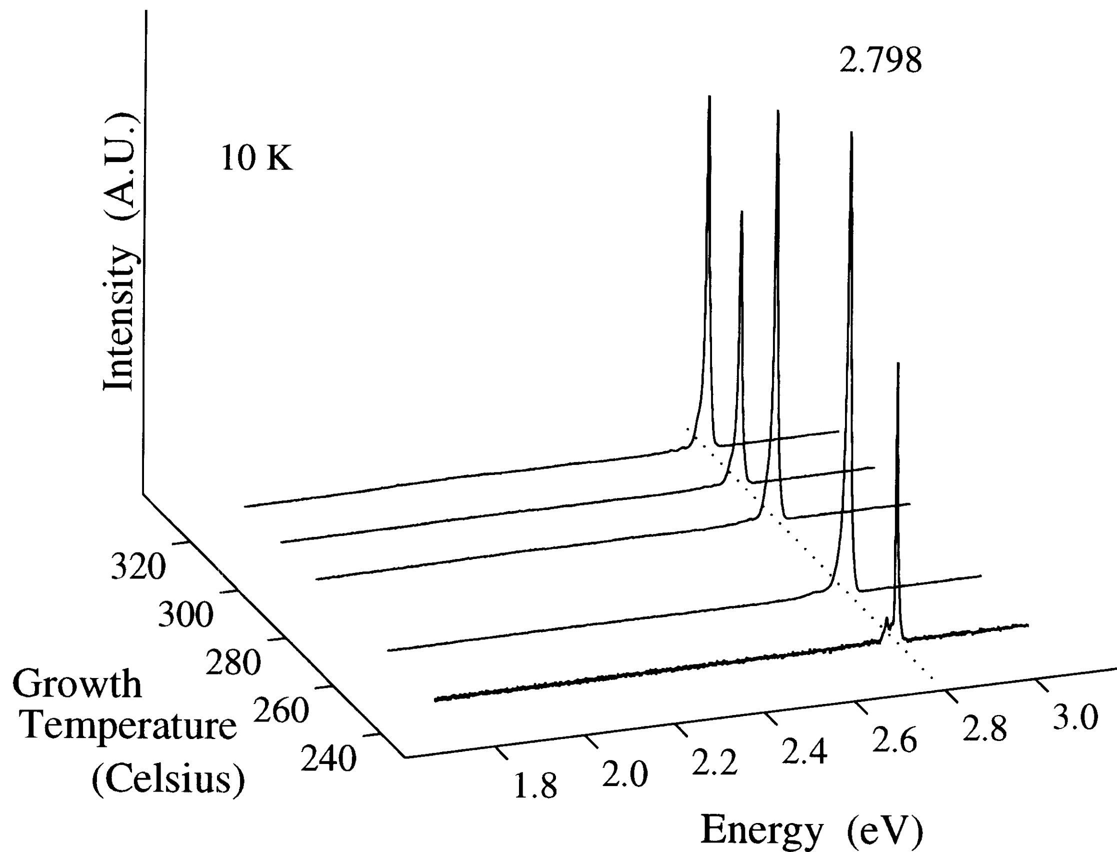

Figure 4.8 Low temperature (10 K) photoluminescence of ZnSe as a function of the growth temperature. The donor-bound exciton feature at 2.798 eV is speculated to be due to chlorine.

Table 4.5 Summary of the growth conditions of the films which are characterized by photoluminescence in Figures 4.6 and 4.7.

Growth Variable		Value
H_2Se flow rate	(sccm)	2.3-2.5
H_2Se Cracker Temperature	(°C)	1000
Zn Effusion Cell Temperature	(°C)	304-305
Zn Flux	(Å/s)	0.68-0.77
Surface Stoichiometry		Se-rich
Growth Time	(hr)	4

an energy of 2.798 eV. Referring to Table C.1 in Appendix C, several donor impurities have energies within the ±1 meV uncertainty of this energy value; energy shifts due to strain are assumed to be small for films 1-2 µm thick. The donor impurity is speculated to be chlorine based on the PL peak energy, and secondary ion mass spectroscopy analysis of ZnSe:N films, to be described in Chapter 6, where chlorine was detected. Though not readily visible in Figure 4.8, a deep luminescence band with an intensity at least 100-1000x weaker than the near-bandedge (NBE) luminescence was centered near 2.25 eV.

To enhance the signal of the defect-related band for closer analysis, the PL of the same set of samples shown in Figure 4.8 were measured at 77 K. As seen in Figure 4.9, the donor-bound exciton remained as the dominant feature in the PL spectra. The energy of the peaks red-shifted to 2.790 eV due to the decrease in the bandgap energy of ZnSe at 77 K. At the lowest growth temperature, a weak luminescence signal originating from a broadly centered defect band was visible near 2.25 eV. For this PL spectrum, the intensity ratio of the donor-bound exciton peak to the defect band was slightly over 10. The energy of the deep luminescence was the same as observed in MOMBE photoluminescence; the origin of this deep level could be due to zinc vacancy complexes. The 77 K PL spectra have more noise than the 10 K spectra because the 77 K scans were measured at a higher lock-in amplifier sensitivity.

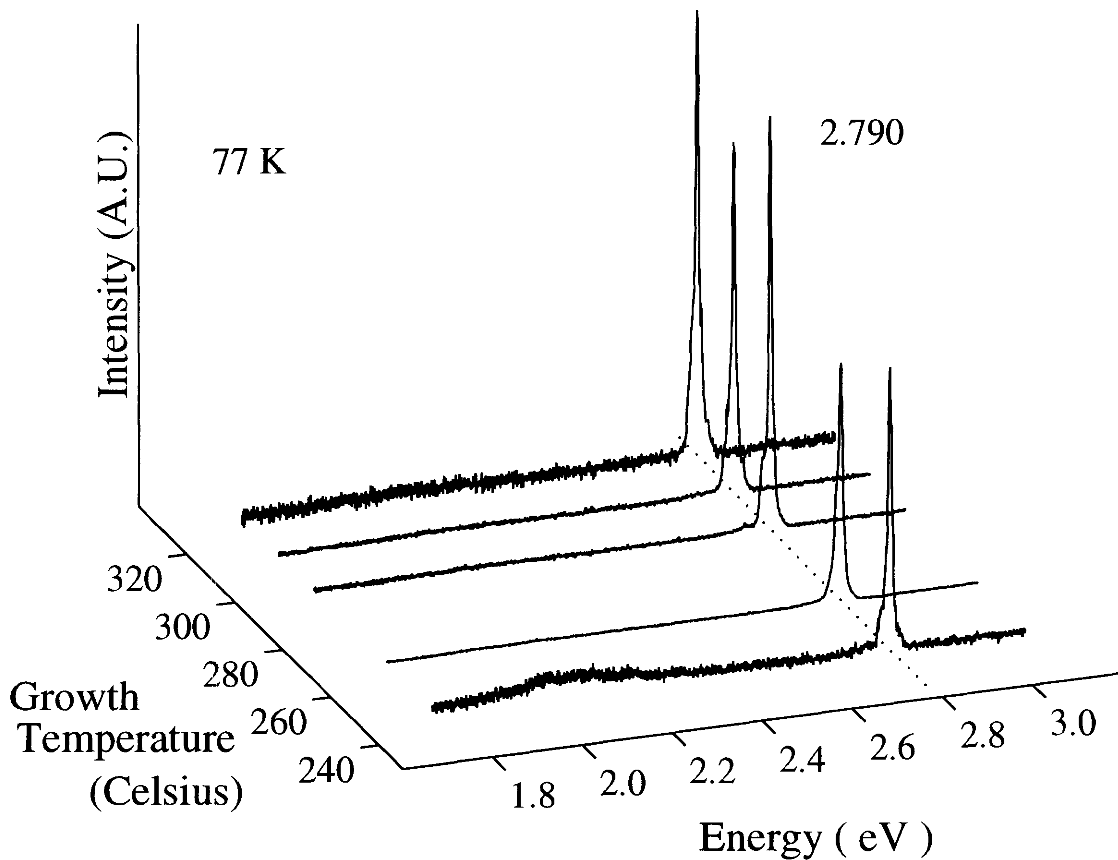

Figure 4.9 77 K photoluminescence of ZnSe as a function of the growth temperature. The donor-bound exciton feature now at 2.790 eV red-shifted in energy due to the decrease in the ZnSe bandgap at 77 K.

A qualitative measure of the ZnSe epilayer quality was obtained from measurements of the integrated intensity of the NBE feature as a function of measurement temperature [86]. A GSMBE grown ZnSe film had its integrated intensity plotted against the PL measurement temperature to quantify the rate of decline in overall luminescent intensity. The integrated intensity fell to 20% of the 10 K value at 77 K, and 5% of the 10 K value at room temperature. Electron-hole pairs created by optical excitation have three possible recombination pathways: (*i*) radiative recombination through free-excitons and bound-excitons, (*ii*) radiative recombination through impurity and defect states within the

bandgap, or (*iii*) recombination at a non-radiative center. A film that has few non-radiative electron-hole trap states is more likely to recombine through the paths described in (*i*) and (*ii*), producing more intense luminescence. As the measurement temperature is raised recombination via path (*iii*) is more favorable. Therefore, films whose integrated intensity decreases slowly with increasing PL measurement temperature are generally of higher crystalline quality.

4.2.3 Electrical Measurements

The undoped ZnSe films were all nominally n-type. Hall effect measurements were performed to determine the free electron concentrations. The Van der Paaw geometry was used for the measurements, and ohmic contacts to the ZnSe were made by In soldering. The free electron concentrations appeared to be influenced by the surface stoichiometry that existed during growth as will be explained in the next section. Electron concentrations ranged from the mid 10^{15} n/cm^{-3} to the low 10^{17} n/cm^{-3}.

4.3 Effect of Surface Stoichiometry

The ZnSe surface was normally maintained in either a Zn-rich or Se-rich surface stoichiometry during a growth. RHEED reconstructions were used to establish whether the surface was Se-rich, (2x1) reconstruction pattern, or Zn-rich, a centered (2x2) pattern. It was observed that the surface stoichiometry during growth influenced the near-bandedge features of the PL, as well as the free carrier concentrations measured by the Hall effect.

Figure 4.10 is a comparison of the photoluminescence of two ZnSe epilayers which were produced using similar growth conditions, except the H_2Se flow was adjusted to produce (a) slightly Se-rich and (b) Zn-rich surface stoichiometry during growth. Independent of the surface stoichiometry, the most intense feature in the near bandedge photoluminescence was a donor bound-exciton transition at 2.798 eV, where the donor

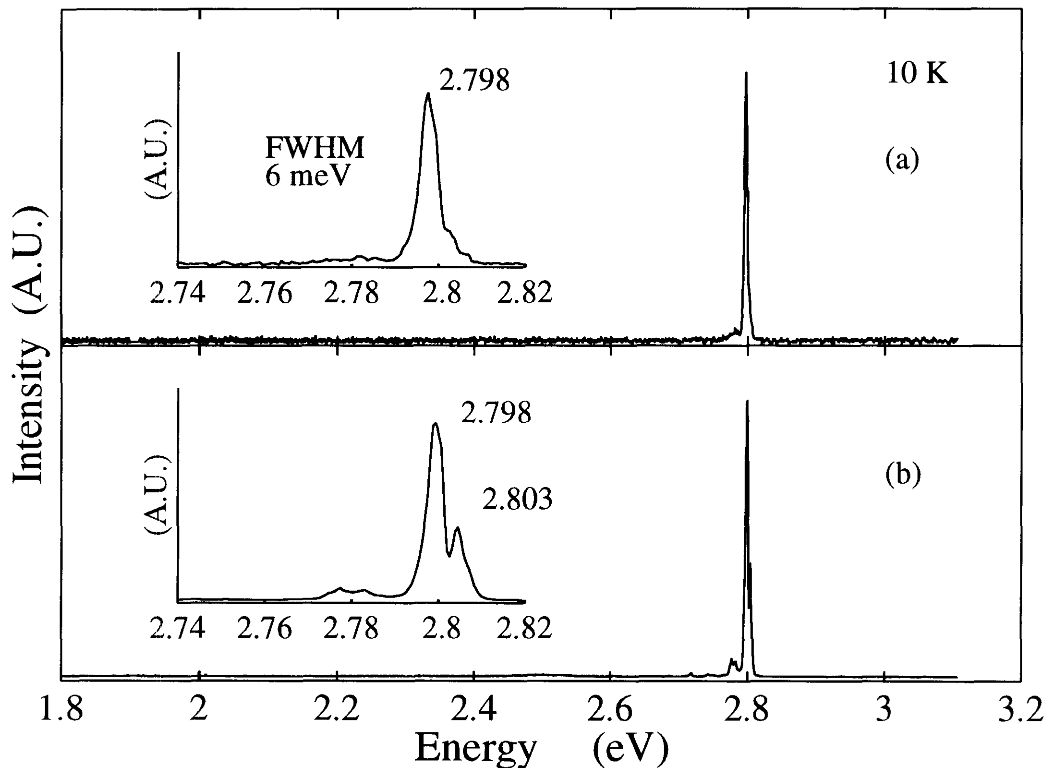

Figure 4.10 Low temperature (10 K) PL illustrating the effect the surface stoichiometry during growth had on near-bandedge features of the photoluminescence. The near-bandedge PL of a film grown with a Se-rich surface (a) was dominated by a donor-bound exciton at 2.798 eV. The film grown with a Zn-rich surface stoichiometry (b) had a distinct free-exciton peak at 2.803 eV.

has been speculated to be chlorine. In the case of the film grown with a Zn-rich surface stoichiometry (b), a free-exciton peak at 2.803 eV is clearly evident. The free-exciton feature appears as a high-energy shoulder of the donor bound-exciton in the Se-rich spectrum (a). The more intense free-exciton peak in spectrum (b) suggested that ZnSe grown under Zn-rich surface stoichiometries would have lower free carrier concentrations.

Hall effect measurements confirmed that films grown with a Zn-rich surface stoichiometry had lower free electron concentrations. Table 4.6 shows the electron concentrations measured for representative films grown with Se-rich and Zn-rich surface stoichiometries. Hall measurements for films grown with a Zn-rich surface had free

Table 4.6 Summary of the effect the surface stoichiometry during growth had on the measured free electron concentrations. Hall effect measurements were performed to obtain the values.

Surface Stoichiometry	Se-Rich		Zn-Rich	
ZnSe Film #	119	123	125	126
Electron Concentration (n/cm^3)	$7x10^{16}$	$5x10^{16}$	$8\text{-}9x10^{15}$	$7\text{-}9x10^{15}$

electron concentrations in the mid 10^{15} n/cm^{-3} to low 10^{16} n/cm^{-3} range. Se-rich films had free electron concentrations an order of magnitude higher in the mid 10^{16} n/cm^{-3} to the low 10^{17} n/cm^{-3} range.

4.5 Summary

High quality ZnSe films 1-2 μm thick were grown by the method of gas source molecular beam epitaxy using elemental zinc and hydrogen selenide. Cracking of the H_2Se at temperatures > 700 °C was required for appreciable growth to occur. GSMBE was observed to be a mass-transport limited growth process and to have a growth temperature dependence similar to MBE. High quality films could be produced over an extended range of growth conditions as indicated by intense low temperature photoluminescence dominated by free- and donor-bound exciton features. Films grown with a Zn-rich surface stoichiometry were observed to have a more intense free-exciton peak in the low temperature photoluminescence, and lower free electron concentrations as measured by the Hall effect, than films which had a Se-rich stoichiometry during growth. Electron concentrations were in the mid 10^{15} to low 10^{16} n/cm^{-3} range for undoped ZnSe grown under Zn-rich surface stoichiometry conditions. Characterization of the structural, optical, and electrical properties of the GSMBE films indicated they were of the same quality as MBE grown ZnSe. This research demonstrates that gas source molecular beam epitaxy

using H_2Se and elemental zinc is capable of producing undoped ZnSe of comparable quality to the established methods of MBE and OMVPE.

Chapter 5

Acceptor Compensation in *P*-Type ZnSe

This chapter discusses the past difficulties in producing low-resistivity *p*-type ZnSe. Reported experimental failures and successes in *p*-type doping are reviewed. Theoretical models of acceptor compensation processes are presented. The motivation for using nitrogen as a *p*-type dopant during GSMBE will become apparent in this discussion. The milestone breakthroughs in achieving low-resistivity *p*-ZnSe [9,10] were preceded by many incremental steps forward in the understanding of compensation processes, and the development of growth techniques which minimized compensation in *p*-ZnSe. Acceptor compensation in ZnSe is once again an active area of research since it has been reported that nitrogen is compensated at high doping levels [87].

The Introduction discussed recent advances in producing *p*-ZnSe:N with substitutional nitrogen (N_{Se}), which resulted in the fabrication of light emitting devices. Prior to the first reports of conductive *p*-ZnSe using Li as a dopant (Li_{Zn}) beginning in 1988 [1,2], ZnSe was seldom mentioned without the accompanying term 'self-compensation.' There was good reason for this association. Attempts to dope ZnSe *p*-type using likely candidates such as Na [88], As [89], and P[90 ,91] yielded highly resistive material. An effort to dope ZnSe using the isoelectronic impurity oxygen as a shallow acceptor also produced highly resistive films [92]. Measurements of the atomic concentrations of the dopants indicated high levels of incorporation into the ZnSe lattice, but very low electrical activation of the acceptors. An accepted explanation for the electrical inactivity was that the intended acceptor atom was inducing the creation of a compensating donor type defect, hence, the common usage of the term self-compensation. While it appears that

most of the difficulties in doping ZnSe *p*-type have been surmounted using nitrogen, it was reported early in the investigations of nitrogen plasma doping that a compensating donor appears at high doping levels [87]. Confirmation of this behavior by other investigators has focused attention on determining the origin of the compensation, so if possible, it may be suppressed. The compensation of the nitrogen acceptor which occurs at high nitrogen doping levels will be discussed in Chapter 7.

Lithium was the first dopant used to achieve low-resistivity *p*-ZnSe [1,2]. Interest in lithium as a *p*-type dopant has waned due to its instability in the ZnSe lattice and the appearance of acceptor compensation at higher doping levels. Lithium was shown to diffuse rapidly throughout the ZnSe matrix during growth at 300 °C [93]. Figure 5.1(a) reproduced from reference [93], illustrates how lithium had diffused into 1.0 μm thick undoped layers from the original 0.5 μm doping region, indicated by the dotted rectangular profile, *during* growth. The SIMS depth profile indicates that Li had diffused into a nearly uniform distribution throughout the entire ZnSe layer. Another serious

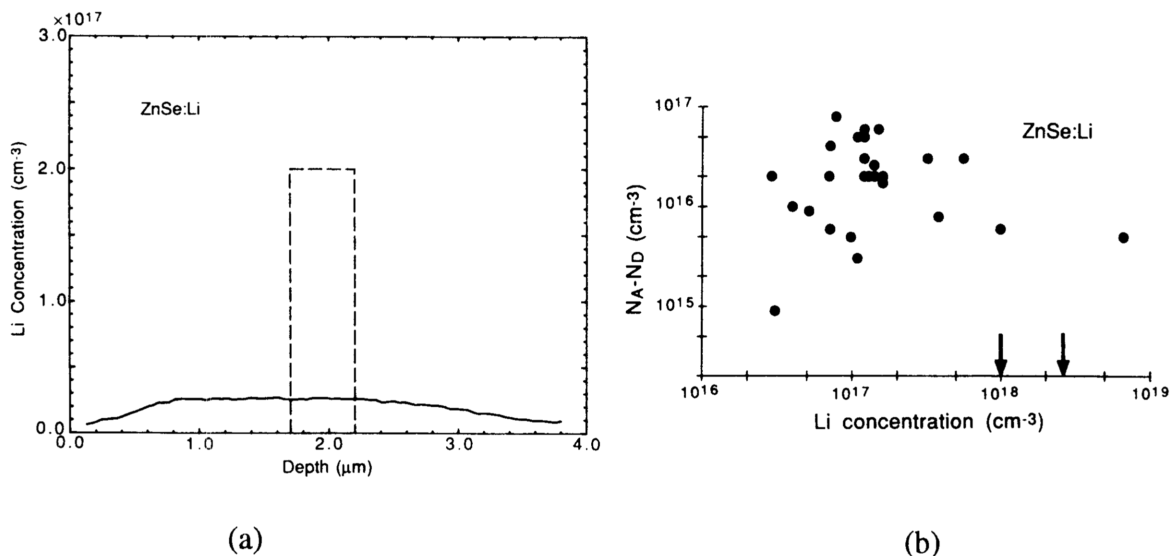

Figure 5.1 Two characteristics of Li which make it a less attractive *p*-type dopant compared to nitrogen. In (a), a SIMS depth profile illustrates how Li diffused into undoped regions during growth from the doped region indicated by the dotted rectangle [93]. The figure in (b) summarizes the net acceptor concentration as a function of the Li concentration. Arrows indicate ZnSe:Li layers which were fully depleted during C-V measurements.

limitation to Li is the appearance of compensating donors, suspected to be Li in interstitial sites or related complexes, which limits the net acceptor concentrations to approximately 10^{17} $(N_A-N_D)/cm^3$. Figure 5.1(b) also taken from [93], illustrates how the net acceptor concentration (N_A-N_D) decreased at higher Li concentrations. In contrast, nitrogen has been reported to be stable in ZnSe at temperatures as high as 400 °C [87]; this temperature is above the processing temperatures currently used to fabricate ZnSe devices.

5.1 Early Compensation Model: Native Defects

The first mechanism suggested for self-compensation was that donors or acceptors introduced into wide bandgap semiconductors would induce the formation of compensated native defects such as vacancies or interstitials by their presence. In 1964 Mandel [94] proposed that the origin of acceptor compensation was through the formation of native defects. It was argued that the host lattice would form electrically active native defects to at least partially compensate the electrical activity of intentionally introduced impurities. Acceptors in ZnSe would be compensated by selenium vacancies in this model. Mandel estimated the degree of compensation based on a formalism first applied by Kroger and Vink [95]. An energy balance was established between the energy supplied by the crystal to form excess defects and the energy gained by the crystal when free carriers interacted with the defects. Calculations based on a singly ionized vacancy model were found to agree with the observed behavior of alkali halides and III-V materials, but could not explain the compensation observed in II-VI materials. Predictions of the degree of compensation in II-VI materials that agreed with the experimental data were obtained by extending the model to include the effect of doubly ionized vacancies. Mandel used thermodynamic data from equilibrium bulk growth processes in estimating the concentrations of native defects; therefore, non-thermal equilibrium growth methods

such as MBE and OMVPE developed after this model was proposed may not be adequately described by this theory.

5.2 Recent Compensation Models

The energies of various defect and impurity configurations within a host lattice have been the subject of several theoretical investigations based on first-principles total energy calculations [12,96 -98]. These calculations were based on the density-functional theory [99] and solved by the pseudopotential method [100]. In addition to estimating the energy of a particular defect or impurity configuration, these models can predict the degree of lattice relaxation caused by a lattice imperfection. Predictions of lattice relaxation can be compared to experimental data to test the validity of a theory.

The study of II-VI materials using magnetic resonance measurement techniques such as electron spin resonance (ESR) [101] or optically detected magnetic resonance (ODMR) [102] has provided information on paramagnetic point defects within host crystals. A defect can be detected using magnetic resonance techniques if a paramagnetic state of the defect exists or can be induced. Defects in semiconductors often have either an unpaired spin state associated with them, or can be easily excited into a paramagnetic state through excitation, e.g. optical illumination. A magnetic resonance spectrum enables the determination of the electron (or hole) g-factor; the g-factor is often unique to a particular defect within a material. Magnetic resonance experiments are of particular interest to defect theorists because the symmetry of the g-tensor, which reflects the symmetry of the defect state, can be determined by measuring the magnetic resonance spectrum at different orientations within a magnetic field. ESR and ODMR have been the primary sources of information on the symmetry of point defects. ODMR measurements were attempted on undoped ZnSe films grown by MOMBE, and on nitrogen doped ZnSe grown by GSMBE. No resonance signals were detected for any of the samples using an ODMR apparatus at MIT. It was subsequently learned after the completion of these

experiments that only a small percentage of ZnSe samples give a detectable magnetic resonance signal [103].

5.2.1 Lattice Relaxation Models

ESR studies of P and As impurities in ZnSe [101] provided some of the first evidence that compensation of acceptors in ZnSe might occur by mechanisms other than native defect formation. It was observed that phosphorus and arsenic in substitutional selenium sites would form deep-levels not associated with any defect, where the symmetry was lowered from T_d to C_{3v} by a Jahn-Teller distortion. Chadi and Chang [12] were the first to propose a mechanism to explain the Jahn-Teller distortion about the impurities using first-principles energy calculations. The Chadi and Chang model postulated a reaction where a neutral and *positive* acceptor state were created from two neutral acceptors. The prediction of a positively charged acceptor state was unusual, but their calculations indicated such a reaction was exothermic and would result in a large lattice relaxation of the type observed in the ESR measurements [101].

Chadi extended the total energy calculations to search for the possibility of a large lattice relaxation in the neutral and ESR active states of column V impurities in ZnSe [96]. It was found that there were *two* distinct configurations for As and P in a neutral charge state. One state was a metastable four-fold coordinated effective-mass-like state. This state which donates a hole will be represented by a^0. The other neutral state was energetically more stable (0.34 eV lower in energy for P) and was characterized by a large lattice relaxation which lowered the symmetry about the acceptor to C_{3v}. The three-fold coordinated state is represented by A^0 in the lattice relaxation reaction shown in Equation (5.1),

$$a^0 \rightarrow A^0 \ . \qquad \text{(Eq. 5.1)}$$

The tetrahedral coordinated a^0 state is metastable since the transition to the A^0 state involves breaking one of the Zn-P bonds, the activation energy for the transformation. Figure 5.2(a-b) are diagrams illustrating the two proposed stable structural configurations for neutral column V acceptors in ZnSe [96]. The four-fold structure of the effective-mass-like state (Figure 5.2(a)) preserves the sp^3 bonding geometry of a substitutional atom in the tetrahedrally bonded zincblende structure. The lattice relaxed state in Figure 5.2(b) has lowered its symmetry from T_d to C_{3v}, resulting in an almost planer sp^2 bonding geometry. The predicted bond displacements of P along the [111] and -[111] directions due to lattice relaxation were in good agreement with the published ESR data [101].

Chadi calculated that N would act as a shallow acceptor in both the four-fold coordinated effective-mass-like state *and* the lower symmetry lattice relaxed state. This prediction might explain the relative success in doping ZnSe *p*-type with nitrogen. Other theorists have performed first-principles energy calculations using more sophisticated pseudopotential models to verify the existence of two stable acceptor states [98]. The preliminary results appear to support Chadi's theoretical predication of a bond-breaking bistability for column V acceptors.

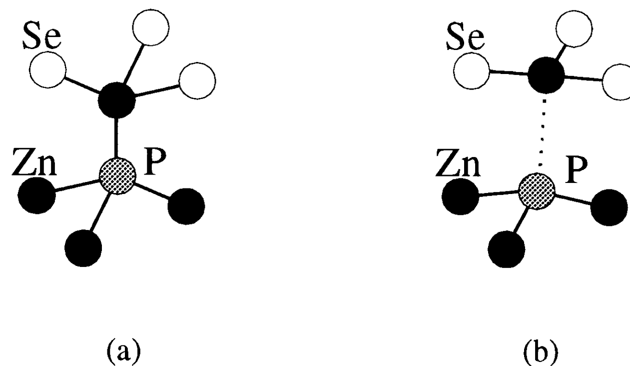

Figure 5.2 Postulated stable structural states of neutral column V acceptors in ZnSe [96]. The four-fold coordinated P in (a) is the shallow effective-mass-like state. The more energetically favorable state (b), characterized by a broken P-Zn bond and subsequent lattice relaxation, has C_{3v} symmetry and a nearly planer sp^2 bonding geometry.

5.2.2 Solubility Limits of Dopants

Theoretical estimates of the solubilities and doping limits of Li, Na, and N in ZnSe have recently been performed [97]. This work calculated the total energies of all native defects and the energies of the various configurations that can be assumed by an impurity in the ZnSe host lattice. The unified treatment of native point defects (vacancies, self-interstitials, and anti-sites) and impurities in the energy calculations allowed the relative concentrations of compensating native defects to be compared to other sources of compensation. Three major findings were advanced based on the calculations: (*i*) under close to stoichiometric growth conditions, native defect concentrations are far too low to explain observed levels of compensation; (*ii*) competition between substitutional and interstitial (compensating) configurations exists for Li; and (*iii*) the solubility limit is imposed by the formation of other phases.

In calculating the solubility limits, precipitation of a new phase was assumed to occur when the chemical potential of a dopant exceeded the chemical potential of the lowest energy compound which could form from Zn, Se, and the dopant element. In the cases of Na, Li, and N, the upper bounds were the chemical potentials of Na_2Se, Li_2Se, and both Zn_3N_2 and N_2, respectively. The solubility limit of Na was calculated to be less than 10^{16} atoms/cm^3; the predicted low solubility limit might explain a previously unsuccessful attempt to dope ZnSe using sodium [88]. The solubility calculations also provide a theoretical basis for the reported success in nitrogen doping. The calculations predict a nitrogen solubility limit greater than 10^{19} atoms/cm^3, and that nitrogen would not experience substitutional/interstitial site competition [97].

In summary, past efforts in doping ZnSe *p*-type reported in the literature have identified nitrogen as the most promising acceptor impurity. Recent total energy calculations predict that acceptor compensation caused by lattice distortions about a column V impurity atom is the lowest for N in the ZnSe lattice. Total energy calculations

have also predicted that the solubility limit of N in ZnSe is greater than 10^{19} atoms/cm^3. Based on the aforementioned evidence, nitrogen doping of ZnSe during GSMBE was investigated.

Chapter 6

Doping With Nitrogen During GSMBE

The discussion in the last chapter identified nitrogen as the best candidate for a *p*-type dopant in ZnSe based on past doping experiments and recent first-principles theoretical calculations. Previous attempts to incorporate nitrogen from N_2 and NH_3 during MBE resulted in low nitrogen incorporation [13], most probably due to very low sticking coefficients of these molecules to the ZnSe surface. Creating a plasma of nitrogen gas prior to injection into the chamber has been demonstrated to greatly enhance the incorporation of N through the creation of species with much higher sticking coefficients [9,10]. Studies of the optical discharges of plasma sources [15,16] suggest that atomic nitrogen is the species created in the plasma leading to high levels of nitrogen incorporation.

This chapter presents the initial results of ongoing research investigating nitrogen doping of ZnSe by a plasma source during gas source molecular beam epitaxy [44]. The effectiveness of a nitrogen plasma source to incorporating nitrogen when operating in the pressure regime of GSMBE (10^{-5}-10^{-4} Torr) was unknown when the doping study was initiated. At GSMBE operating pressures, the molecular mean free path is on the order of the source to substrate distance of 21 cm. At the confluence of the molecular beams in front of the substrate, the probability of a collision is even higher. The concern was that collisions with other molecules would either de-excite an excited state of a N_2 molecule, or remove atomic nitrogen through bonding, reducing the 'active' nitrogen species the plasma source was generating. Nitrogen concentrations as high as 6×10^{18} atoms/cm^3 in ZnSe:N films grown thus far suggest that the sticking coefficient of the 'active' nitrogen

species (now believed to be atomic nitrogen) remains high when the plasma source is operated at GSMBE pressures.

6.1 Radio Frequency Plasma Source

The radio frequency (RF) plasma source (model MPD21) used in these experiments was manufactured by Oxford Applied Research, Crawley Mill, England; future experiments are using an upgraded version of the MPD21 source, a CARS25. The MPD21 is called a free radical source (FRS) by the manufacturer, and will be referred to as a FRS in this thesis. The Oxford RF plasma source is the most common type of plasma source being used for nitrogen doping during MBE; an alternative to a RF source is an electron cyclotron resonance plasma source [104].

6.1.1 Description

The FRS was designed to fit in an effusion oven location on a MBE system. The MPD21 which has a 4.5" mounting flange, was bolted to a 6" source flange on the II-VI epitaxy chamber using a 6" to 4.5" adapter flange. The FRS operated at a frequency of 13.56 MHz. Power from a 600 Watt RF generator (Advanced Energy, model RFX-600) was delivered through a capacitance impedance matching network to the RF coupling on the FRS. ULSI grade nitrogen gas (Matheson Gas Products) was supplied through a two-stage regulator to a precision leak-valve attached to the FRS. The source was cooled using the chilled water heat-exchange system of the II-VI reactor.

A schematic drawing of the source is shown in Figure 6.1. The plasma was struck in the cavity formed by the PBN discharge tube and the aperture. RF excitation was coupled into the plasma via the water cooled RF coil surrounding the discharge tube. A single 0.3 mm hole in the exit aperture allowed a molecular beam of nitrogen species to enter the reactor chamber. The glow of the plasma discharge was visible through the viewport

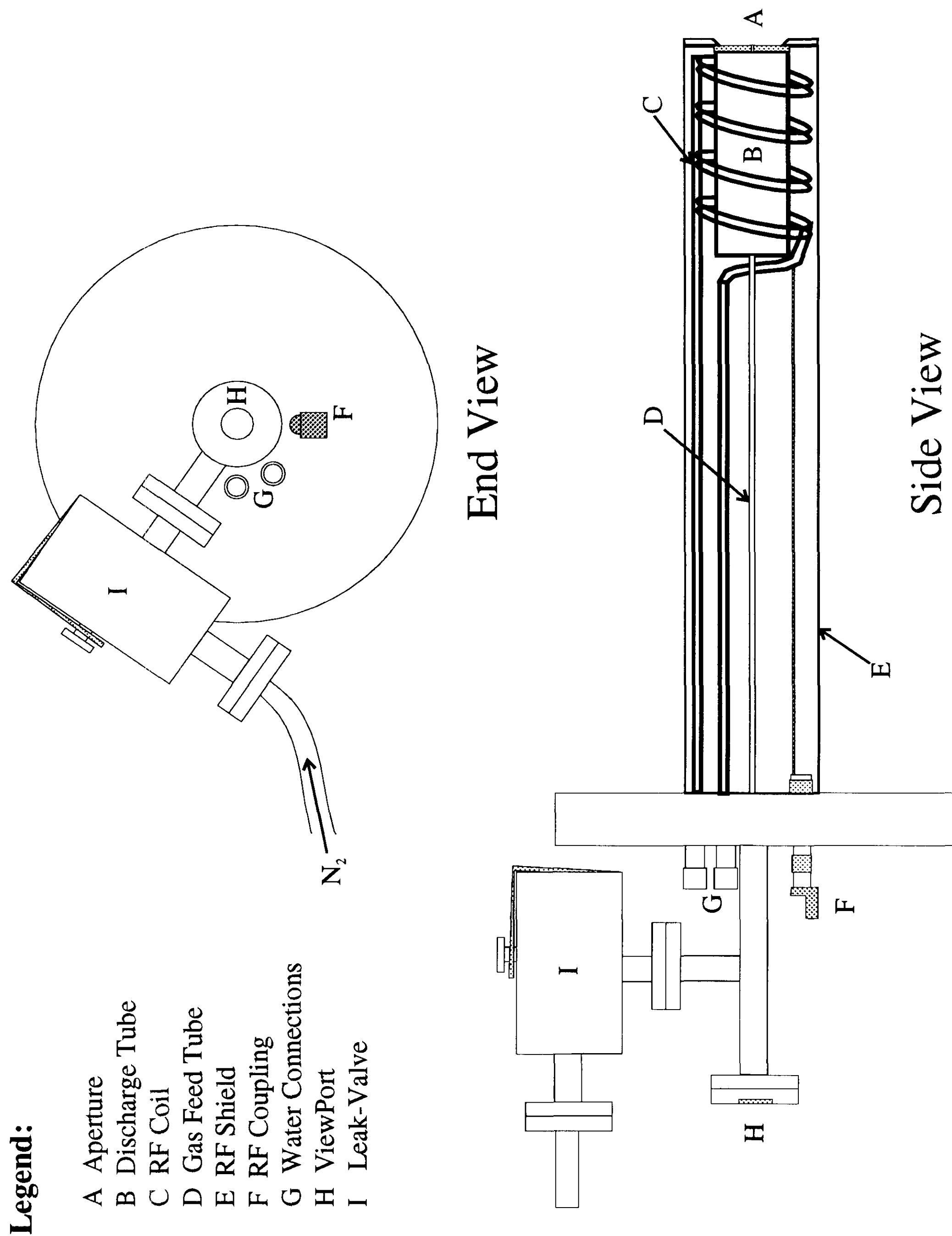

Figure 6.1 Schematic drawing of the Oxford free radical source. The capacitance matching network which makes electrical contact at the RF coupling (F) is not shown.

which looked down the gas feed tube. A Si photodiode could be placed over this viewport to monitor the intensity of the plasma discharge.

6.1.2 Operation

The conditions to strike a plasma in the FRS depended on the nitrogen flow through the plasma discharge region as well as the applied RF power. The plasma had two operating modes, low and high brightness, which could easily be differentiated by eye. The low brightness mode was reported to incorporate nitrogen less efficiently [87], so the FRS was always operated in the high brightness mode. The FRS was purchased with automatic tuning electronics (ATM-600) to adjust the capacitance of the impedance matching network. The reflected power returned to the generator would fall below 1% when the matching network was tuned with the plasma in the high brightness mode.

To establish a measure of the nitrogen flow through the FRS, the background pressure in the chamber due to nitrogen flowing through the FRS was monitored on an ionization gauge. In this chapter a nitrogen flow was defined by the background pressure it created in the epitaxy chamber. A plasma was excited by setting the nitrogen flow $\geq 2 \times 10^{-5}$ Torr and setting the RF power at approximately 200 Watts. Once the plasma struck, the power was set at its desired value and the nitrogen flow allowed to stabilize prior to introducing the H_2Se. The automatic tuning unit optimized the impedance of the capacitance network to minimize the amount of reflected power.

A unique feature of this plasma source is that the plasma discharge region was isolated from the rest of the II-VI chamber. Accelerated ion bombardment damage of the substrate apparently does not occur using this type of plasma source. Past efforts of low energy ion implantation of nitrogen produced polycrystalline material at [N] = 2×10^{18} atoms/cm^3 [10]; no such damage occurs in nitrogen plasma doped ZnSe with [N] > 10^{19} atoms/cm^3, suggesting that few, if any, nitrogen ions bombard the substrate.

6.2 ZnSe:N Produced Using a RF Plasma Source

A systematic study of nitrogen doping using the FRS was undertaken. The goal was to optimize the growth and plasma conditions to maximize the hole concentrations in *p*-ZnSe. Table 6.1 summarizes by experiment number the ZnSe growth conditions and FRS plasma settings which were used in the doping study. The GSMBE growth conditions which had an effect on nitrogen incorporation are listed on the left side of Table 6.1. The ZnSe growths were performed at roughly three temperatures of 250, 270, and 290 °C. The temperatures are grouped according to the surface stoichiometry that was maintained during growth, either Zn-rich or Se-rich. The plasma source settings are shown across the top of Table 6.1. The FRS power was set at 100, 150 (once), 200, or 300 Watts as measured by the forward power meter on the RF generator. The nitrogen flow which was measured by the chamber ionization gauge was set at 5.0×10^{-6}, 1.0×10^{-5}, or 2.0×10^{-5} Torr. The growth conditions and plasma settings were held constant throughout a film growth,

Table 6.1 Summary of growth conditions and plasma source settings used in RF plasma doping study. The experiment number is entered in the matrix location corresponding to the conditions used.

Increasing Atomic Nitrogen →

Growth Conditions Which Enhance Nitrogen Incorporation ↓

Surface Stoichiometry	Substrate Temperature (Celsius) \ Background N_2 Pressure (Torr)	RF Power to FRS (Watts): 100			200		300	
		5×10^{-6}	1×10^{-5}	2×10^{-5}	1×10^{-5}	2×10^{-5}	1×10^{-5}	2×10^{-5}
Se-Rich	290	128	130					
	270	127	129	131, 132	133		135	136
	250			134				
Zn-Rich	270		144	137, 143*		138		148
	250			142		145		146

* Actual power was 150 Watts for 143.

so the [N] was expected to be uniform. It will be shown in section 6.2.2 that growth and plasma source conditions in the bottom right corner of Table 6.1 resulted in greater nitrogen incorporation in the ZnSe films.

6.2.1 Evidence of Nitrogen Incorporation

The presence of nitrogen in the ZnSe was detected by changes in the low temperature photoluminescence attributed to the presence of nitrogen acceptors [13], and secondary ion mass spectroscopy (SIMS) measurements of the atomic nitrogen concentration.

6.2.1.1 Photoluminescence

Photoluminescence of ZnSe:N are shown in Figure 6.2. The 10 K spectra are compared for samples grown under identical growth conditions, however, the nitrogen flow was systematically increased at a fixed RF power of 100 Watts in an attempt to increase the nitrogen incorporation into the films. The growth conditions for these films are summarized in Table 6.2. The top spectrum (Figure 6.2(a)) is the photoluminescence of an undoped film grown under identical growth conditions, and is provided as a reference for the changes that occurred in the PL as the nitrogen flow was increased. The PL of the sample doped using the lowest nitrogen flow (Figure 6.2(b)), had a neutral N acceptor-bound exciton peak at 2.793 eV appear in the near-bandedge region. A free electron-to-acceptor transition (FA) was present at 2.716 eV, and a zero-phonon donor-acceptor-pair (DAP) transition at 2.700 eV with its associated phonon-replicas were also visible. A higher nitrogen flow resulted in a merging of the FA and DAP transitions, forming a dominant peak at 2.707 eV (Figure 6.2(c)). At the highest nitrogen flows investigated (Figure 6.2(d)), the FA transition disappeared, and the DAP and phonon replicas merged into a single broad feature. Similar changes in the PL spectrum, corresponding to increasing levels of nitrogen incorporation as measured by SIMS, had been observed by Ohkawa et al. [10], which suggested that our ZnSe:N incorporated greater [N] with higher nitrogen flows through the FRS.

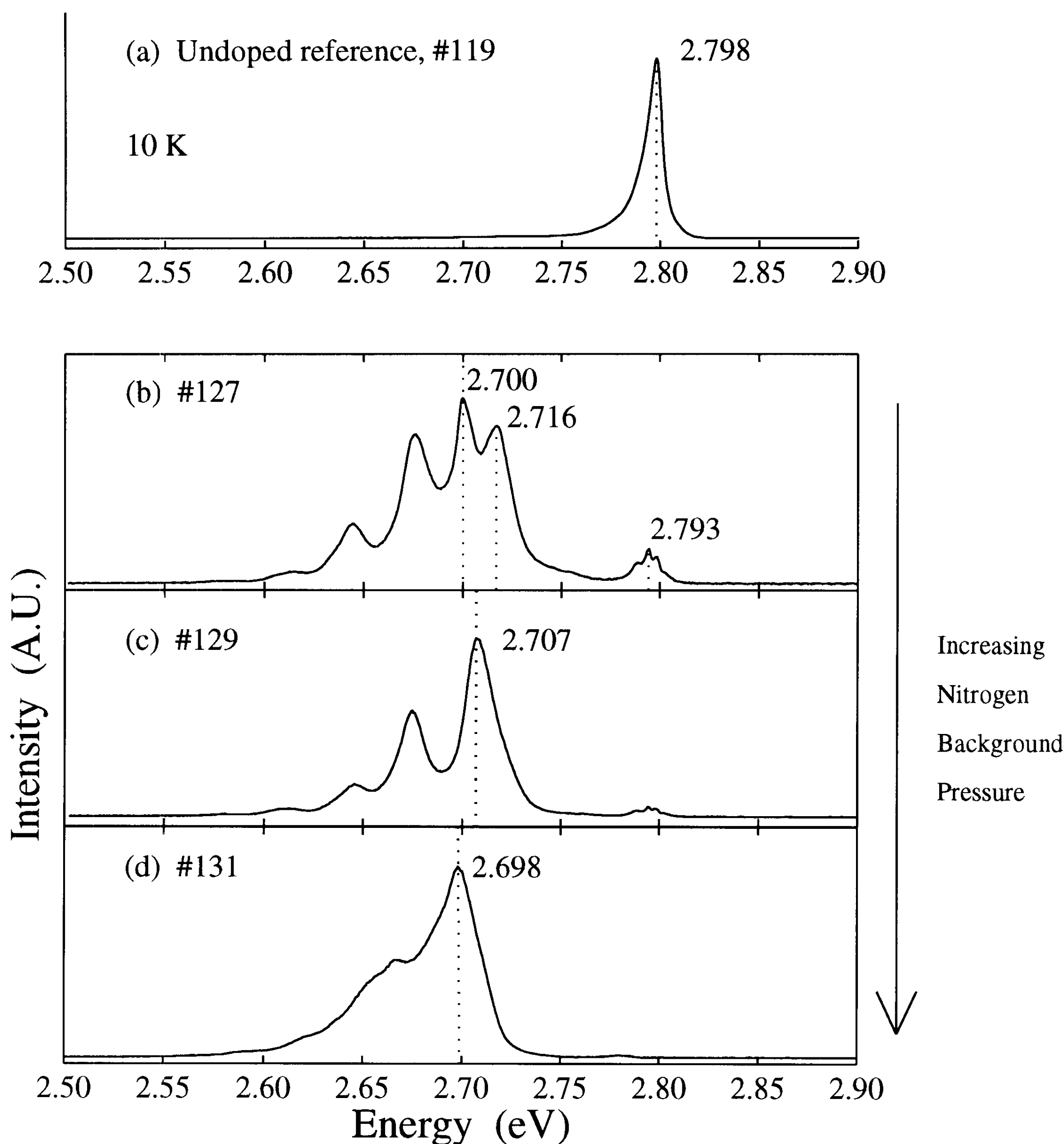

Figure 6.2 The 10 K photoluminescence intensity as a function of energy for nitrogen flows of: (a) no flow (undoped), (b) $5x10^{-6}$ Torr, (c) $1x10^{-5}$ Torr, and (d) $2x10^{-5}$ Torr, measured by the chamber ionization gauge.

The energies of the FA and the zero-phonon DAP transitions can be used to estimate the acceptor ionization energy of the nitrogen acceptor. Subtracting the FA transition energy from the 4 K ZnSe bandgap energy of 2.822 eV gives an acceptor binding energy of 106 meV. The acceptor ionization energy can also be calculated from the equation:

$$E_{DAP} = E_g - (E_D + E_A) + e^2/\varepsilon r \,, \qquad \text{(Eq. 6.1)}$$

where $e^2/\varepsilon r$ is the Coulomb donor-acceptor interaction term (~ 14 meV [24]). Using the donor binding energy for chlorine (26.1 meV [28]), the lightly doped no-phonon DAP value (2.700 eV), and the 4 K bandgap energy, the acceptor binding energy estimated from Equation (6.1) is 109 meV. Both of these values are in good agreement with the value of 110 meV determined by Dean et al. [24].

Table 6.2 Growth conditions of the films which have their photoluminescence shown in Figure 6.2.

Variable		Value
Substrate Temperature	(°C)	270-280
Surface Stoichiometry		Se-Rich
Zn Effusion Cell Temperature	(°C)	303-304
Average Zn Flux	(Å/s)	~ 0.7

6.2.1.2 Secondary Ion Mass Spectroscopy

Secondary ion mass spectroscopy was used to measure the atomic concentrations of nitrogen and likely impurity elements in the ZnSe:N. The SIMS depth profiles were measured by Evan East of Plainsboro, New Jersey. The data was obtained using a Perkin-Elmer Physical Electronics Model 6300 SIMS instrument. A positive cesium ion was the primary bombarding species. The ion current was approximately 200 nAmp with an ion energy of 5 keV. The secondary ion intensities were converted to atomic concentrations using ion implanted ZnSe standards. The profile depths were calibrated after analysis by measuring the depths of the sputtered craters with a stylus profilometer. The overall accuracy of each set of measurements were estimated to be in the 15-20% range.

Figure 6.3 is a SIMS depth profile of ZnSe #148. The calibrated atomic concentrations of nitrogen, hydrogen, and chlorine are shown on the left side axis. The

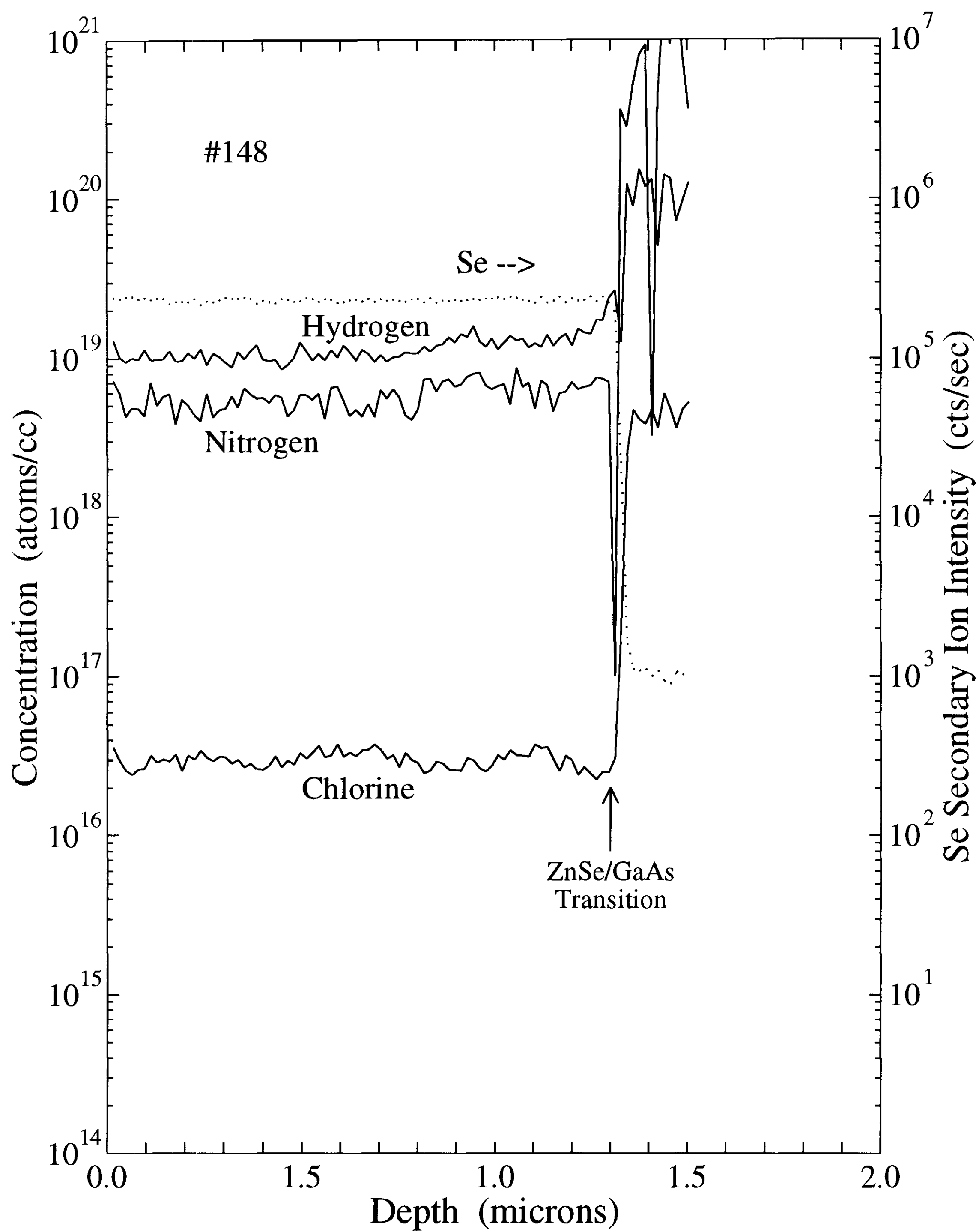

Figure 6.3 SIMS depth profile of ZnSe #148. Depth profiles of the calibrated atomic concentrations of nitrogen, hydrogen, and chlorine are shown. The nitrogen concentration in this uniformly doped film was approximately 5×10^{18} atoms/cm^3.

approximate location of the ZnSe:N/GaAs heterointerface is indicated by the arrow at 1.3μm. ZnSe #148 had the highest measured [N] to date of approximately 6×10^{18} atoms/cm^3. The profile throughout the ZnSe:N layer was uniform which was expected for the constant doping conditions used. The impurities of hydrogen and chlorine are both above their detection sensitivity limits of approximately 1×10^{17} and 2×10^{16} atoms/cm^3, respectively. The concentrations are only valid within the ZnSe:N epilayer since the calibration of atomic concentrations were made using implanted ZnSe standards.

6.2.2 Plasma Doping Dependencies

6.2.2.1 Nitrogen Flow Rate

Figure 6.2 suggests that nitrogen incorporation into the ZnSe lattice was greater when higher nitrogen flows were used during doping. The three ZnSe:N films whose PL is shown in the figure were analyzed by SIMS to determine the [N]. All three films had nitrogen concentrations below the detection limit of approximately 1×10^{17} atoms/cm^3 for the measurements, so it could not be confirmed with this set of samples that the atomic nitrogen concentration was an increasing function of N_2 flow for a fixed power.

6.2.2.2 RF Power

Nitrogen incorporation was found to be strongly dependent on the RF power supplied to the FRS during doping. Figure 6.4 is a plot of the [N] measured by SIMS as a function of the RF power used to excite the plasma. The substrate temperature was 270 °C and the nitrogen gas flow was 2.0×10^{-5} Torr for these doping experiments. ZnSe:N grown with a Zn-rich surface stoichiometry are indicated by the solid points, while the single Se-rich film with a [N] above the detection limit is denoted by the circle. Increasing [N] with increasing RF power is a characteristic reported by all other researchers using a RF plasma source. At higher RF excitation powers the intensity of the plasma emission associated

with atomic nitrogen increased [15,16], implying that the atomic nitrogen concentration in the plasma also increased at higher RF powers.

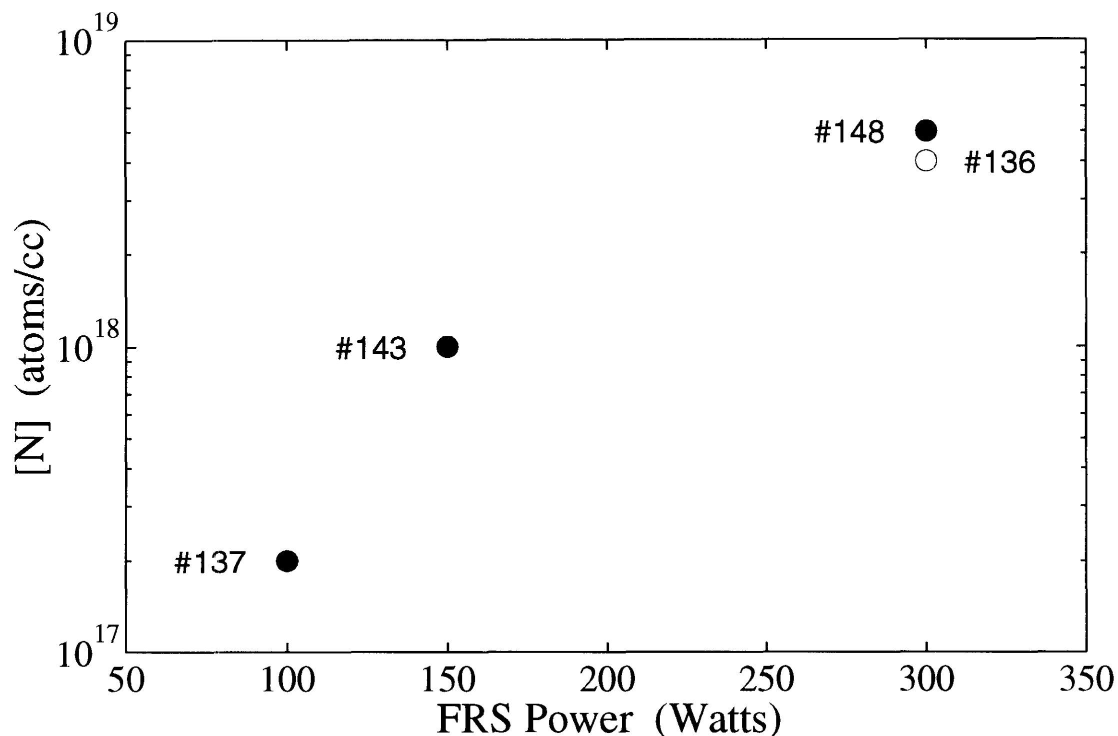

Figure 6.4 Nitrogen concentration measured by SIMS as a function of the RF power supplied to the FRS. The background pressure due to the nitrogen flow was $2x10^{-5}$ Torr during doping. Data denoted by the solid points (•) are from films grown with a Zn-rich surface stoichiometry, while the circle (○) was from a Se-rich growth.

6.2.2.3 Growth Temperature

The substrate temperature was observed to influence the degree of nitrogen incorporation. ZnSe:N films # 137 and # 142 were grown at substrate temperatures of 270 and 250 °C, respectively. The measured nitrogen concentrations for these films were $2x10^{17}$ and $4x10^{17}$ atoms/cm^3, respectively. The greater nitrogen incorporation at lower growth temperatures, and the dependence of nitrogen incorporation on nitrogen flow and RF power, are in agreement with the conclusions of an extensive investigation of nitrogen RF plasma doping during MBE [87].

6.2.2.4 Surface Stoichiometry

In Figure 6.5 the effect of the surface stoichiometry on the incorporation of nitrogen is shown. The figure compares the photoluminescence of films grown with either a Se-rich (a) or Zn-rich (b) surface stoichiometry, but otherwise identical growth conditions. The merging of the DAP transition and its phonon replicas into a single peak in (b) (see Figure 6.2), suggested that nitrogen incorporated more effectively on the Zn-rich surface. SIMS measurements confirmed that the [N] of the ZnSe:N whose PL is shown in Figure 6.5(b) ($2x10^{17}$ atoms/cm^3) was higher than the Se-rich growth of Figure 6.5(a) (< 10^{17} cm^{-3}). This result was in agreement with published papers which examined the effect of the surface stoichiometry on nitrogen incorporation during MBE [10,105].

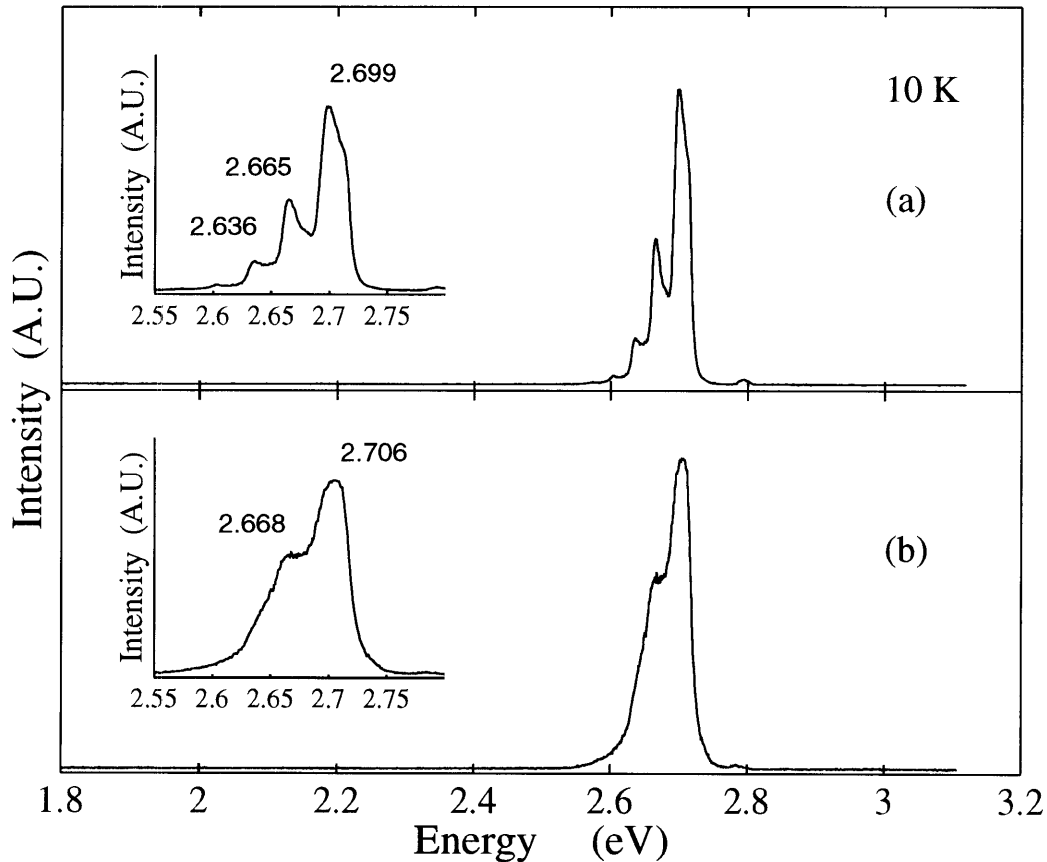

Figure 6.5 The 10 K photoluminescence from films grown with (a) a Se-rich , and (b) Zn-rich surface stoichiometry during growth.

6.3 Characterization of ZnSe:N

The structural characteristics of the GSMBE ZnSe:N films were similar to the undoped layers. RHEED patterns of the ZnSe:N surfaces were streaky, resembling the RHEED of an undoped film shown in Figure 4.4. The surfaces were featureless when view at a 1000x magnification under a Nomarski microscope. The structural properties of the ZnSe:N did not appear to degrade at nitrogen concentrations as high as $\leq 6\text{x}10^{18}$ atoms/cm^3.

It was not possible to use the Hall effect to measure the hole concentrations due to the difficulty in making an ohmic contact to *p*-ZnSe. The valence band of ZnSe is over 1 eV deeper than the GaAs valence band. As a consequence, the Fermi level of *p*-ZnSe is $\geq$ 1.5 eV below the work function of metals such as Au or Pt. Two novel approaches to form contacts to *p*-ZnSe have been described [106 ,107], but the complexity of these methods precluded their use.

Capacitance-voltage (C-V) measurements were made using Cr/Au Schottky contacts in a ring-dot configuration. The devices were typically 200 μm dots with a 20 μm wide separation between the center dot and the outer ground plane. The measurement frequency was 1 MHz. The ZnSe:N epilayers were 1.2-2 μm thick. The depletion layer width W in the semiconductor side of the Schottky contact can be estimated using the equation,

$$W = \sqrt{\frac{2\varepsilon_s}{qN_A}\left(V_{bi} - V - \frac{kT}{q}\right)} \quad [108], \qquad \text{(Eq. 6.2)}$$

where ε_s is the semiconductor permittivity ($9.1\varepsilon_o$ for ZnSe), V_{bi} and V are the Schottky barrier height (built-in potential) and the applied voltage, respectively, and N_A is the concentration of acceptors which will be approximated by (N_A-N_D). The depletion layer width for a net-acceptor density of $5\text{x}10^{15}$ acceptors/cm^3 will be estimated. Assuming a large Schottky barrier height V_{bi} of 1.5 Volts, W = 0.5 μm for no applied voltage. An

additional depletion layer existed at the GaAs/ZnSe heterojunction. The depletion layer within the ZnSe at the heterojunction was widest when a *n*-type GaAs substrate was used (most devices were fabricated on semi-insulating substrates), but the magnitude of the built-in potential for the heterojunction in this worst case depletion layer width scenario was still less then the 1.5 Volt barrier assumed in the Schottky barrier depletion width calculation. A conservative estimate of the total depletion layer thickness (at the Schottky barrier and heterojunction) within a C-V device at zero applied voltage is twice the Schottky depletion width, ~ 1 μm for $(N_A-N_D) = 5x10^{15}/cm^3$. Since the minimum ZnSe:N layer thickness was ~ 1.2 μm, a capacitance-voltage measurement should be valid for $(N_A-N_D) > 5x10^{15}$ net-acceptors/cm^3.

Table 6.3 summarizes the electrical characteristics of all the ZnSe:N produced thus far. The net-acceptor concentrations measured by the capacitance-voltage method are shown in the second column. An entry of 'flat-band' indicates the film had a $(N_A-N_D) \leq 10^{15}$ net acceptors/cm^3 since the capacitance did not change with reverse bias, indicating insulating films. The final three columns of Table 6.3 contain SIMS data if it was available.

The three films which had measurable (N_A-N_D) were not unique when compared to the growth and doping conditions of the other films summarized in Table 6.1. The high resistivity of the films might be due to hydrogen passivation of the N acceptor atoms; hydrogenation will be covered in the next chapter. No explanation can currently be offered to explain why films #135, #136, and #137 were conductive. To check if the conductivity of the films was influenced by the processing of the ring-dot devices, conductive and highly resistive films were processed into ring-dot structures multiple times. Repeated C-V measurements yielded the same values listed in Table 6.3, apparently ruling out the possibility that post-growth device processing was affecting the C-V data.

Table 6.3 Summary of the C-V measurements and chemical concentrations of nitrogen and hydrogen measured by SIMS of the ZnSe:N films grown to date. An entry of 'flat-band' indicates the film was highly resistive resulting in a flat C-V trace. [N] and [H] are shown if available.

ZnSe:N film	C-V $(N_A - N_D)$ /cm^3	SIMS (atoms/cm^3) [N]	[H]	[H]/[N] Ratio
127	flat-band	$< 10^{17}$		
128	flat-band			
129	flat-band	$< 10^{17}$		
130	flat-band	$< 10^{17}$		
131	flat-band	$< 10^{17}$		
132	flat-band			
133	flat-band			
134	flat-band	$< 10^{17}$		
135	10^{16}	$2x10^{18}$	$6x10^{18}$	3
136	10^{16}	$2x10^{18}$		
137	10^{17}	$2x10^{17}$	$2x10^{18}$	10
138	flat-band	$5x10^{18}$		
142	flat-band	$4x10^{17}$	$1.5x10^{18}$	4
143	flat-band	$1x10^{18}$	$2x10^{18}$	2
144	flat-band			
145	flat-band	$2x10^{18}$	$6x10^{18}$	3
146	flat-band	$5x10^{18}$	$1x10^{19}$	2
148	flat-band	$5x10^{18}$	$1x10^{19}$	2

Figure 6.6 is a SIMS depth profile measurement of ZnSe #135. The ZnSe:N layer was grown on a 0.8 μm undoped ZnSe layer. This figure and the SIMS profile in Figure 6.3 indicate that hydrogen incorporated in concentrations greater than the nitrogen concentration. The final column of Table 6.3 shows that the [H]/[N] ratio is typically between 2 and 4. The sharp drop in the [N] concentration at the transition between the doped and undoped layers suggested that substitutional N was stable in the ZnSe matrix at the growth temperature of 270 °C. Profiling through the ZnSe:N/ZnSe layer interface revealed a phenomenon not apparent in the uniformly doped films; hydrogen was preferentially incorporating into layers which were nitrogen doped. Chlorine was also observed in higher concentrations in the ZnSe:N layers, but to a much lesser degree than

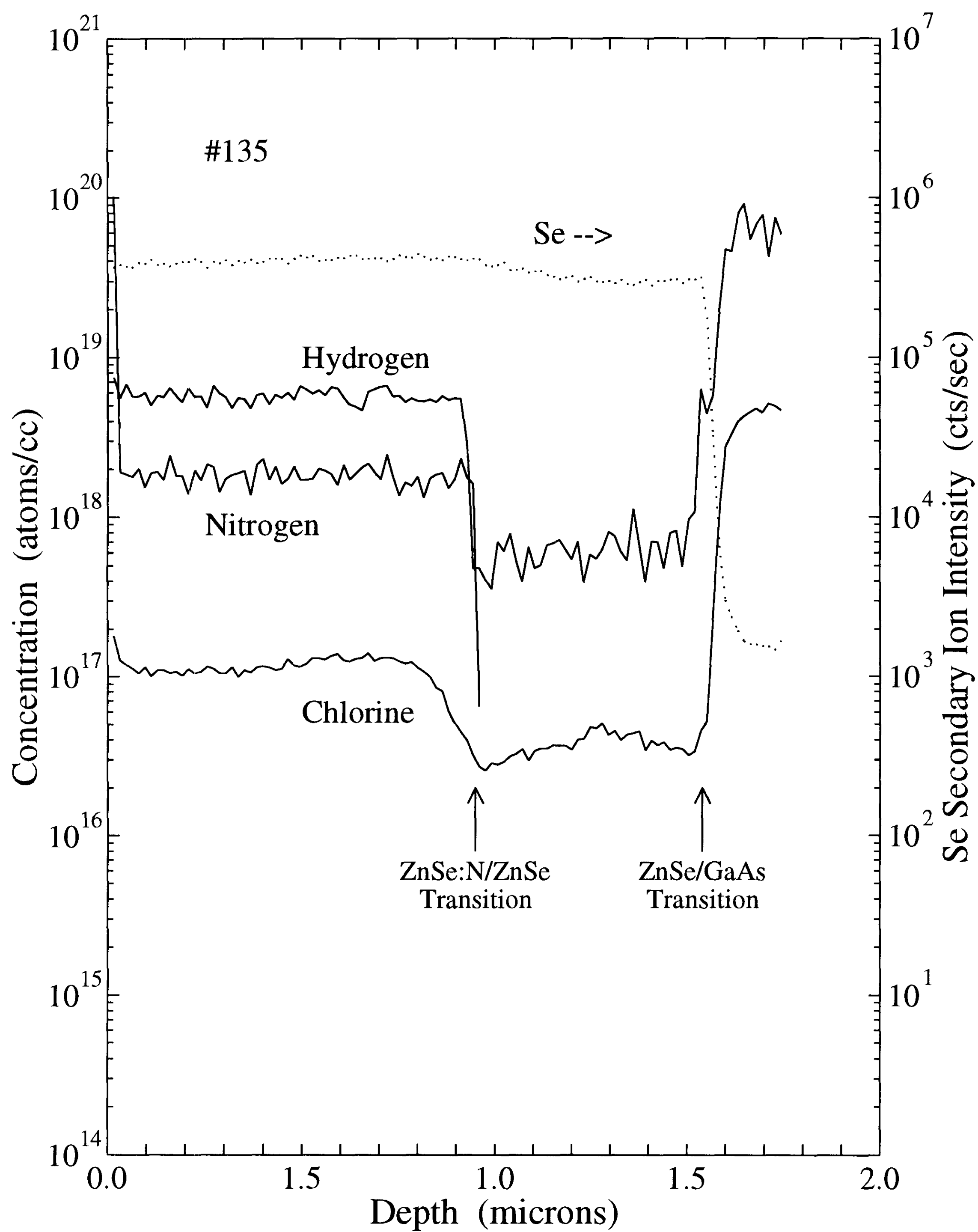

Figure 6.6 SIMS depth profile of ZnSe #135. The structure consists of a doped ZnSe:N layer on an undoped ZnSe layer. The hydrogen and chlorine concentrations are observed to be higher in the nitrogen doped layer.

hydrogen. The concentrations of hydrogen and chlorine fell below the detection limits of the SIMS apparatus in the undoped layer. The very sharp drop in the hydrogen concentration at the ZnSe:N/ZnSe layer interface suggests that there exists a strong interaction between the hydrogen and nitrogen, possibly bonding, which prevents diffusion of the mobile hydrogen into the undoped layer.

Imaizumi et al. at Mitsubishi Electric Corporation have reported obtaining low resistivity *p*-ZnSe:N grown by GSMBE using H_2Se and Zn sources [82]. A RF plasma source was used to incorporate the nitrogen acceptor resulting in ZnSe:N layers with net-acceptor concentrations as high as 10^{18} acceptors/cm^3. The Mitsubishi researchers reported growth rates which were 2 to 4 times higher than we investigated, but the growth temperatures and the H_2Se cracking temperature were similar. Imaizumi et al. speculated that the H_2Se cracking temperature affected the degree of hydrogen incorporation, although they had not conducted extensive experiments to verify this claim. Therefore, further optimization of the growth condition such as the H_2Se cracking temperature might enable us to achieve low resistivity *p*-ZnSe:N.

6.4 Summary

Utilizing a RF nitrogen plasma source during growth, we have produced ZnSe:N films with nitrogen concentrations as high as 6×10^{18} atoms/cm^3 as measured by SIMS. The structural characterization performed to date has not revealed any degradation in the structural qualities of ZnSe:N layers compared to the undoped films, even at the highest levels of nitrogen incorporation. The low temperature photoluminescence exhibited features reported to be characteristic of low resistivity *p*-ZnSe:N grown by MBE. Electrical characterization of the GSMBE grown ZnSe:N by capacitance-voltage measurements indicated that they were highly resistive, except for three films which had (N_A-N_D) in the 10^{16} - 10^{17} net-acceptors/cm^3 range. Thus far, we have been unable to determine or replicate the conditions which produced the ZnSe:N with measurable net-

acceptor concentrations. SIMS measurements revealed that hydrogen was an impurity in the ZnSe:N layers, incorporating in concentrations 2 to 4 times as great as the nitrogen. Hydrogen incorporation in the undoped layers, if it was occurring, was below the detection limit of the SIMS measurements which was approximately 5×10^{17} atoms/cm^3. Based on the characterization, it was concluded that ZnSe:N grown by GSMBE was not conductive due to hydrogen passivation of the nitrogen acceptor. The growth conditions are being optimized in an attempt to lower the hydrogen incorporation to achieve low resistivity *p*-ZnSe:N as has been reported by another group performing GSMBE [82]. The electrical activity of the nitrogen acceptors must be increased if GSMBE growth of ZnSe is to develop into a competitive technology for the fabrication of blue-green light emitting devices.

Chapter 7

Outstanding Issues in Nitrogen Doping

Two issues have developed in using nitrogen as a substitutional acceptor in ZnSe. A critical issue for gaseous growth methods such as GSMBE and OMVPE is hydrogen passivation of the nitrogen acceptor which appears to occur under most growth conditions. A general issue pertaining to all the epitaxial methods is the appearance of a deep donor state in highly doped ZnSe:N which is apparently limiting the hole concentrations to $\leq 10^{18}$ *h*/cm^3.

7.1 Hydrogenation

There have been no reports of low resistivity *p*-type ZnSe:N grown by the method of OMVPE. The highest net acceptor concentration reported for OMVPE grown ZnSe:N has been ~ $1\text{x}10^{17}$ acceptors/cm^3 in a photo-assisted OMVPE doping study [109]. Most researchers have reported (N_A-N_D) concentrations below 10^{16} acceptors/cm^3. Our efforts at producing low-resistivity ZnSe:N by GSMBE have thus far not succeeded, as was documented in the previous chapter. A common factor in the methods of OMVPE and GSMBE is the presence of hydrogen in the growth process. SIMS analysis of our ZnSe:N epitaxial films have revealed heavy hydrogen contamination in the layers doped with nitrogen. Low resistivity *p*-ZnSe:N produced by GSMBE has recently been reported [82], so it may be possible to avoid hydrogenation using this growth method.

7.1.1 Experimental Evidence of N-H bond in OMVPE Grown ZnSe

When the nitrogen plasma doping experiments were initiated, hydrogenation in ZnSe:N had not yet been reported. Recently, two reports have appeared [45,46] which

conclude that acceptor compensation in OMVPE grown ZnSe:N is caused by hydrogen passivation of the nitrogen acceptor. One paper was a study of OMVPE grown ZnSe:N characterized by SIMS and infrared absorption measurements [45]. This study is particularly relevant to our GSMBE doping research due to the striking similarities in a SIMS depth profile presented in the paper to the SIMS depth profile of one of our ZnSe:N layers shown in Figure 6.6. SIMS analysis of an OMVPE grown ZnSe:N layer showed an almost one-to-one incorporation ratio of hydrogen to nitrogen at concentrations exceeding 10^{19} atoms/cm^3 [45]. The ZnSe:N had been grown on an undoped ZnSe layer (the same structure of our sample profiled in Figure 6.6), so changes in the concentrations when entering the undoped layer were visible. The nitrogen and hydrogen concentrations dropped sharply to the detection limits in the undoped OMVPE grown layer. This is qualitatively identical behavior to what is observed in Figure 6.6 for our GSMBE grown ZnSe:N. Spectroscopic evidence of a N-H bond was obtained by infrared absorption measurements at 11 K. An absorption peak at 3193 cm^{-1} was identified which was found to be unique to the nitrogen doped films. This energy is close to the nitrogen-hydrogen stretching mode in the ammonia molecule (3336 cm^{-1} [110]), and in *a*-SiN:H film (3340 cm^{-1} [111]). It was concluded that hydrogen was passivating the intended nitrogen acceptor based on the equal concentrations of nitrogen and hydrogen, and the existence of an infrared absorption peak close in energy to known nitrogen-hydrogen vibrational stretching modes. The compensation mechanism for hydrogen passivation in ZnSe:N was proposed to be the following [45]:

$$N^{-} + h^{+} + H^{0} \rightarrow (NH)^{0} . \qquad \text{(Eq. 7.1)}$$

Thus, the free hole created by the nitrogen acceptor is neutralized when nitrogen and hydrogen bond.

A second paper currently in press [46], studied OMVPE grown ZnSe:N by infrared absorption and Raman spectroscopy. The layers examined had electrically-active acceptor concentrations (measured by C-V) of less than 10^{15} acceptors/cm^3, even though SIMS measurements showed nitrogen concentrations exceeding 10^{18} atoms/cm^3. Infrared absorption measurements at 9 K had two peaks in the spectrum, one at 3194 cm^{-1} and another at 783 cm^{-1}, which were only observed in the nitrogen doped ZnSe; measurements of undoped OMVPE layers did not have these peaks. The high energy peak at 3194 cm^{-1} was attributed to the stretching mode of a N-H complex, and the low energy peak at 783

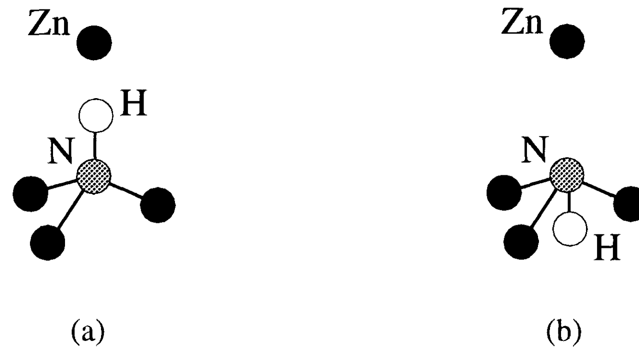

Figure 7.1 Proposed configurations for N-H complex based on C_{3v} symmetry of N-H complex determined from Raman spectroscopy [46]. The configuration in (a) has hydrogen located in the bonding direction (bond centered position), while configuration (b) shows the anti-bonding location.

cm^{-1} to a wagging mode of a N-H complex. Characterization by polarized Raman spectroscopy indicated that the N-H complex had C_{3v} symmetry. A model for the N-H complex was proposed where the H atom is bonded to the N in either a bonding or anti-bonding direction [46]. Figure 7.1 shows the two proposed bonding configurations which satisfy the C_{3v} symmetry observed in Raman measurements.

7.1.2 Possibilities to Reverse Hydrogen Passivation.

Hydrogen has been observed to passivate shallow donors and acceptors in other semiconductors such as Si [112], GaAs [113], and InP [114]. Si and III-V material

which is hydrogen passivated can have extremely low dopant activation, as deduced from comparisons of dopant concentrations measured by SIMS to the net-acceptor densities measured by C-V. Table 6.3 is a compilation of the measured (N_A - N_D), and the nitrogen and hydrogen concentrations, for our GSMBE grown ZnSe:N. A large disparity exists between the nitrogen concentrations and (N_A-N_D), which suggests that the layers are hydrogen passivated. Hydrogen passivation has been demonstrated to be completely reversible in Si, GaAs, and InP. Reactivation of the dopant can be accomplished through annealing. As an example, Te and Sn ions passivated in hydrogenated GaAs can be completely reactivated by annealing for 1 hour at 325 °C [113]. Recently published research on OMVPE grown ZnSe:N has investigated the effect of a rapid thermal anneal (RTA) on the electrical characteristics [115]. An increase in the (N_A-N_D) concentrations into the mid 10^{16} acceptors/cm^3 range has been achieved using a RTA, demonstrating that an anneal will reactivate nitrogen acceptors to some degree. As part of the continuing study of nitrogen doping during GSMBE, RTA experiments will be performed on the ZnSe:N to investigate if the nitrogen acceptor can be reactivated through annealing.

7.2 Compensation in Heavily Doped ZnSe:N

It was first reported by Qui et al. [87] that heavily doped ZnSe:N grown by MBE was compensated. Compensation places an apparent upper limit on (N_A-N_D) of approximately $1x10^{18}$ acceptors/cm^3 [87]. Hole concentrations of 10^{18} h/cm^3 are too low for *p*-ZnSe:N and a metal such as Au or Pt to form an ohmic contact. The Fermi level of *p*-ZnSe:N is > 1.5 eV below the work function of candidate contact metals [107], hence, large hole concentrations are necessary for an ohmic contact to occur through tunneling.

7.2.1 Evidence of a Deep Donor State

Detailed photoluminescence studies of heavily doped ZnSe:N grown by MBE has been reported by several groups [87,116 -118]. These studies stated that a second DAP

transition series, associated with a new compensating donor state, appears at high levels of nitrogen incorporation. The zero-phonon peak energy of this second DAP transition has been reported to range from a low value of 2.623 eV [87] to a high value of 2.689 eV [118]. The scatter in the reported values for the position of the zero-phonon DAP transition might be due to a dependence of the DAP peak position on the PL excitation intensity [117]. Photoluminescence measurements of our films with the highest nitrogen incorporation (#146 and 148) had a peak energy of the DAP feature at approximately 2.65 eV. It is possible that compensation through a new donor state which appears at high [N] is occurring in these layers, but this can not be proven until increased conductivity is obtained in our GSMBE doped films. Optically detected magnetic resonance has been used to investigate the recombination associated with the deep DAP transitions [119]. A new anisotropic donor magnetic resonance was observed for the deep DAP transition. This deep donor resonance was not present in lightly doped ZnSe:N, which suggests that it is associated with the nitrogen compensation mechanism occurring at high doping levels. The anisotropy of the *g*-tensor suggested that the symmetry about the donor or donor complex would have axial symmetry.

7.2.2 Proposed Models for Compensation

Hauksson et al. [116] have proposed a model for the compensation process in ZnSe:N based on their photoluminescence measurements. The model postulates that the compensating donor is a complex of V_{Se} - Zn - N_{Se} which is depicted in Figure 7.2. The complex involves a selenium vacancy in the next-nearest neighbor position to a substitutional nitrogen atom. A V_{Se} is a double donor with an ionization energy of 300 meV [120], but the complex of V_{Se} - Zn - N_{Se} is expected to be a shallow single donor. This model can account for the axial symmetry observed in ODMR [119] and polarization-dependent photoluminescence measurements [118].

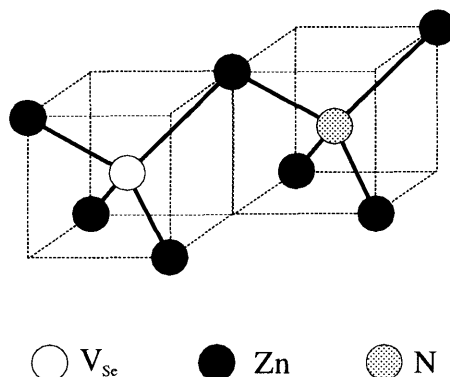

Figure 7.2 Model for the deep donor complex in ZnSe:N involving the next-nearest neighbor association of a selenium vacancy and nitrogen acceptor [116].

Chadi and Troullier [121] have suggested that the origin of self-compensation in nitrogen-doped ZnSe might be due to interstitial nitrogen. Based on previous first-principles total energy calculations of self-interstitials in Si and GaAs [122], they predict that nitrogen can occupy three energetically stable two-fold coordinated interstitial sites in ZnSe. Two of the interstitial configurations are predicted to be acceptors, but the third interstitial configuration is a shallow donor which is the speculated source of compensation. Recently, two new deep trap states in *p*-ZnSe:N have been detected using deep-level transient spectroscopy techniques [123] which lends credibility to the model of Chadi and Troullier which predicts three energetically stable interstitial sites. This model can also account for the observed experimental evidence concerning nitrogen compensation collected thus far, so further characterization of compensated ZnSe:N is still required to clarify the actual nature of the compensating defect.

Chapter 8

Summary and Suggested Future Work

ZnSe was grown by the method of metalorganic molecular beam epitaxy using diethylzinc and/or diethylselenium. The growth rates during MOMBE were unusually low at less than 400 Å/hr whenever a diethyl metalorganic source gas was used; this included MOMBE experiments where the diethylzinc or diethylselenium were replaced by elemental zinc/DMZn or elemental Se, respectively. It was proposed that surface sites for incorporation of the metal atoms (zinc in particular) were saturated by chemisorbed ethyl radicals at the low growth temperatures, thus limiting the growth rate. In a parallel investigation of laser-assisted MOMBE, it was observed that laser illumination of the substrate during growth would reduce the site blockage phenomenon under appropriate growth conditions. Electron-beam irradiation of the substrate using the RHEED gun was found to have qualitatively the same effect on growth as the laser beam. In one experiment, the measured growth rate in the laser illuminated region was increased by as much as a factor of 15 over the unilluminated growth rate. It is hypothesized that the laser illumination or electron-beam irradiation created holes which drifted to the surface and participated in oxidation reactions, leading to the removal of the ethyl radicals, thus allowing Zn to incorporate into the lattice increasing the growth rate. A model for the laser-assisted growth rate enhancement was developed in section 3.8 which could qualitatively explain what was observed experimentally when laser-assisted MOMBE was performed using at least one diethyl metalorganic source.

The quality of the undoped ZnSe grown by MOMBE was strongly dependent on the surface stoichiometry which existed during growth. Control of the surface stoichiometry through adjustments of the metalorganic gas flows was greatly reduced when surface

passivation of the metal incorporation sites by the ethyl radicals occurred, resulting in a degradation of the optical and structural properties of the films. Low temperature photoluminescence measurements of most films were dominated by a deep defect-related luminescence band centered near 2.25 eV. This defect band has been attributed to highly nonstoichiometric growth, and is postulated to be due to zinc vacancy complexes in the MOMBE films. X-ray diffraction rocking curves of fully strained ZnSe on GaAs substrates had FWHMs of approximately 220 arc seconds. Fully strained MBE grown ZnSe films have FWHMs in the 150 arc seconds range, indicating less perfect internal structure of the MOMBE films. Structural characterization of the film surfaces indicated comparable quality to MBE grown ZnSe. Laser illumination was observed to enhance the incorporation of Zn, which under certain conditions would dramatically improve the optical quality of the films by promoting a surface stoichiometry with a Zn:Se ratio closer to unity.

High quality ZnSe films 1-2 μm thick were grown by the method of gas source molecular beam epitaxy using elemental zinc and hydrogen selenide. GSMBE was observed to be a mass-transport limited growth process and to have a growth temperature dependence similar to MBE. High quality films were produced under a variety of growth conditions as indicated by intense low temperature (10 K) photoluminescence dominated by free- and donor-bound exciton features. Films grown with a Zn-rich surface stoichiometry were observed to have a larger free-exciton peak in the low temperature PL, and lower free electron concentrations as measured by the Hall effect, than films which had a Se-rich stoichiometry during growth. Characterization of the structural, optical, and electrical properties of the GSMBE films indicated they were of comparable quality to MBE grown ZnSe.

Employing a RF nitrogen plasma source during growth, ZnSe:N films with nitrogen concentrations as high as $6x10^{18}$ atoms/cm^3 as measured by SIMS were produced. The

low temperature photoluminescence exhibited features reported to be characteristic of low-resistivity *p*-ZnSe:N grown by MBE. Electrical characterization of the GSMBE grown ZnSe:N by capacitance-voltage measurements indicated that they were highly resistive, except for three films which had (N_A-N_D) in the 10^{16}-10^{17} net-acceptor/cm^3 range. SIMS measurements revealed that hydrogen was an impurity in the ZnSe:N layers, incorporating in concentrations 2 to 4 times as great as the nitrogen. Based on the electrical characterization and SIMS analysis, it was concluded that ZnSe:N grown by GSMBE was not conductive due to hydrogen passivation of the nitrogen acceptor.

Thus far, hydrogen passivation of the nitrogen acceptor has been a severe impediment to the fabrication of low resistivity *p*-ZnSe:N using epitaxial methods which have hydrogen in the growth process. From a materials growth standpoint, the best approach is to avoid incorporating hydrogen as an impurity in the ZnSe matrix. It might be possible to reduce the incidence of N-H bond formation by altering the growth conditions from those currently used. Experiments should be performed where the H_2Se cracker temperature is raised or lowered from its current value of 1000 °C to evaluate the effect on hydrogen incorporation; researchers who have reported low resistivity *p*-ZnSe:N grown by GSMBE have speculated that the degree of hydrogen incorporation is sensitive to the H_2Se cracking temperature [83]. The substrate temperature could also be raised to investigate the effect of higher growth temperatures on hydrogen incorporation. Laser-assisted GSMBE experiments should be conducted if possible, since the highest reported net-acceptor concentrations for OMVPE grown ZnSe:N were obtained using photo-assisted growth [111]. A parallel investigation into possible methods to reactivate the nitrogen acceptor is also recommended. Rapid thermal anneals are suggested for ZnSe due to the degradation of the material properties with extended high temperature processing. If the aforementioned approaches should fail, it may be necessary to switch to another source

gas for selenium which does not release hydrogen during its decomposition to release the selenium metal.

Significant progress in the development of ZnSe-based blue-green light emitters was described in Chapter 1. The rapid advances over the last three years which culminated in the demonstration blue laser-diodes, might suggest that commercial blue and green wavelength light emitters based on the ZnSe material system are eminent in the near future. Unfortunately, significant materials issues still need to be resolved before ZnSe-based light emitters can enter the commercial marketplace. Nitrogen compensation appears to be a long-term problem which presents two significant challenges. Currently, the formation of ohmic contacts requires expensive, hard to implement techniques [106,107], since the free hole concentrations are limited by compensation to 10^{18} h/cm^3, a concentration to low for tunneling to occur across the large Schottky barrier at the metal *p*-ZnSe interface. A potentially more serious problem associated with nitrogen compensation is that it may be contributing to the short lifetimes of current blue-green light emitting devices.

The difficulties in creating ohmic contacts to *p*-ZnSe reduces the economic competitiveness of ZnSe-based light emitters compared to other alternatives for blue-green light emitting devices Both of the approaches to achieve ohmic contacts require that epitaxial layers which can be heavily doped *p*-type be deposited between the *p*-ZnSe and the contact metal. The necessity of using another epitaxial growth step (usually in a separate epitaxy chamber) adds complexity to the production process and incurs additional cost in equipment; this is not an attractive option if ZnSe-based devices are going to be developed commercially. Eliminating compensation in ZnSe:N or raising the threshold for compensation to high hole concentrations will be required if low-cost evaporated metal contacts are to be used.

The use of nitrogen as a *p*-type dopant in ZnSe may be in jeopardy if it is demonstrated that the nitrogen compensation mechanism is contributing to the degradation of blue-green light emitters. It has recently been reported that the photoluminescence decay time of heavily doped ZnSe:N is less than 11 picoseconds [124]. The very rapid PL decay was attributed to a high concentration of Schockley-Read nonradiative recombination centers, possibly the result of nitrogen self-compensation. Current blue-green light emitters degrade very rapidly through the formation of dislocation networks in the active region [33]. The dislocations in the active region nucleate at existing defects (nonradiative recombination centers), in a fashion characteristic of electronically-enhanced defect reactions [34]. Therefore, it may be necessary to use another *p*-type dopant for ZnSe if the nitrogen compensation at high doping levels can not be eliminated or greatly suppressed.

Appendix A

RHEED

Reflection high-energy electron diffraction (RHEED) is an *in-vacuo* technique to monitor the smoothness of a surface and the reconstructions that develop to minimize the surface free energy. RHEED is accomplished by directing an electron-beam at near glancing incidence to a film's surface. The electrons reflected off the surface strike a phosphor screen causing luminescence wherever one impinges. Electron interference generated by diffraction from periodic arrangements of atoms near the film surface produce patterns which depend on the orientational azimuth of the substrate. The shallow glancing angle limits the electron penetration depth to a few monolayers since the normal component of the electrons' energy is small. Therefore, a RHEED image is the diffraction from lattice atoms just below the surface and from any periodic surface reconstruction. Figure A.1 is a drawing of the geometry used for RHEED in these experiments. The electron-beam angle of incidence was between 1-2° and depended on the physical dimensions of the sample holder used.

The power of RHEED as a surface diagnostic tool will be illustrated in a discussion of how the surface smoothness may be inferred from observed RHEED patterns. Electrons penetrated only a few monolayers deep into a sample since the normal component of their kinetic energy was low in the glancing incidence geometry. Electrons which were incident on a surface growing in a layer-by-layer fashion (Frank-van der Merwe mode), where only a few monolayers are not complete at any given time, experienced true reflection diffraction. The diffraction pattern consisted of elongated lines (streaky features) resulting from the constructive interference of electrons diffracted from atoms which were parallel

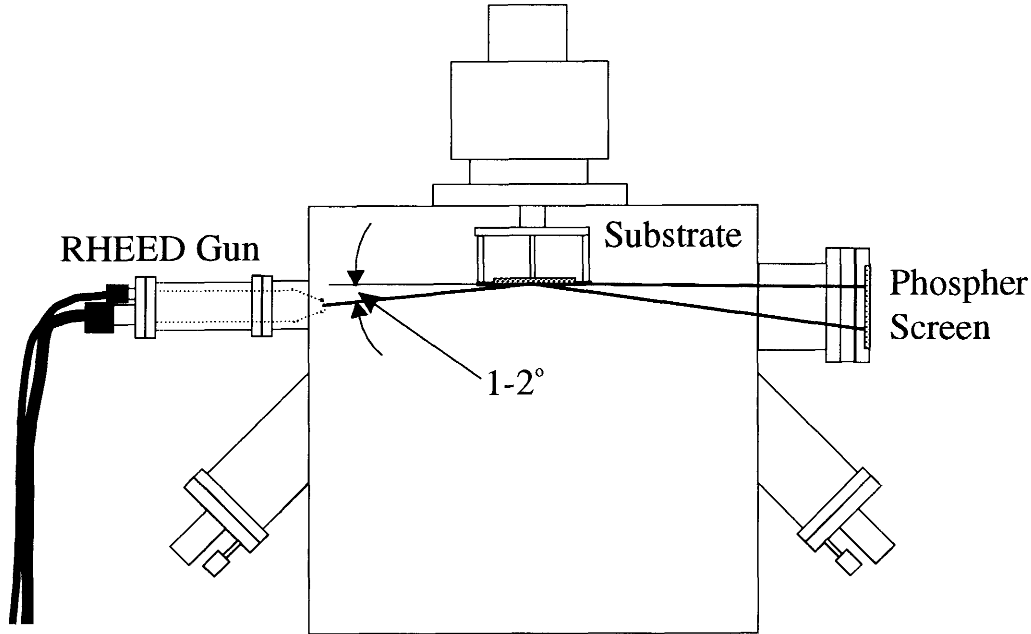

Figure A.1 Geometry of RHEED configuration on the II-VI chamber.

to the electron beam direction and resided within the first few monolayers. If growth were to proceed in a Volmer-Weber mode, where islands many monolayers high coalesce to form a layer, the diffraction patterns would be points (spotty) since the electron-beam underwent transmission-reflection through the islands. Interference occurring normal to the surface collapses the lines to points so the image resembles a bulk x-ray diffraction pattern. The intermediate case of layer plus island formation, the Stranski-Krastanov growth mode, lies between the aforementioned cases and appears as a combination of streaky lines and spots in the RHEED image. Figure A.2(a-c) illustrate what has been described above concerning the origin of the RHEED patterns.

Surface reconstruction features could be prominent in a RHEED image due to the shallow penetration depth of the electron-beam. A surface reconstruction was the orderly rearrangement of surface atoms so as to minimize the surface free energy at the adsorbed gas-solid interface. Many dangling bonds exist at a surface. The free energy of the

Figure A.2 Illustrations of the origins of RHEED patterns [52]. The surface smoothness may be inferred from the particular RHEED pattern observed. Surface reconstructions are not shown in the figure.

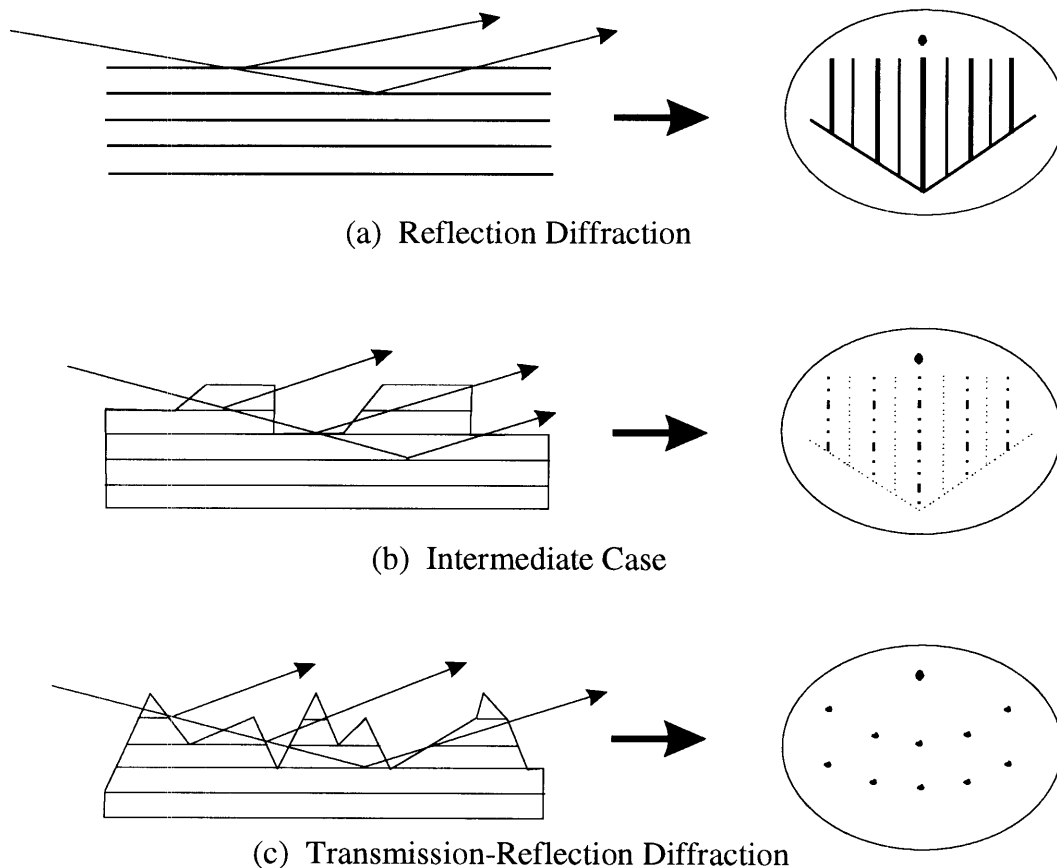

surface could be reduced if atoms or molecules chemisorb to the dangling bonds. The energy could be reduced further if the chemisorbed atoms or molecules would form cross-link bonds with each other, and/or displaced their equilibrium positions relative to the bulk lattice positions. The resultant surface reconstruction, which had a periodicity that was a multiple of the underlying lattice periodicity, appeared as features within the lattice diffraction lines. An example of a surface reconstruction can been seen in Figure 3.10.

Appendix B

DCXRD

Double crystal x-ray diffraction (DCXRD) is a high resolution method to determine the lattice constant of a thin film. A rocking curve measurement records the angular separation between substrate and layer diffraction peaks. From the relative positions and angular separation of the substrate and layer diffraction peaks the degree of relaxation of a film can be determined and the composition of an alloy estimated. The angular separation of a (400) reflection was used to determine the out-of-plane lattice constant; the in-plane lattice constant was calculated from the out-of-plane value through an expression relating the elastic constants of ZnSe. The full width at half maximum (FWHM) of a peak has been correlated with the defect density in the film (misfit dislocations) so it provides a qualitative measure of the structural quality.

A schematic drawing of the DCXRD apparatus is shown in Figure B.1. The first crystal used to collimate the x-ray beam was an InP substrate; since the first crystal was different from the GaAs substrates being measured, it was necessary to set the detector at an angle of 4.2°. The second axis where the sample was mounted was rocked very slowly by a stepper motor to generate the angular scan. A personal computer controlled the stepper motors on the DCXRD and recorded the counts from the detector. X-ray counts would be recorded when diffraction from a set of lattice planes satisfied the the Bragg diffraction condition for constructive interference,

$$n\lambda = 2d\sin\Theta \ . \qquad \text{(Eq. B.1)}$$

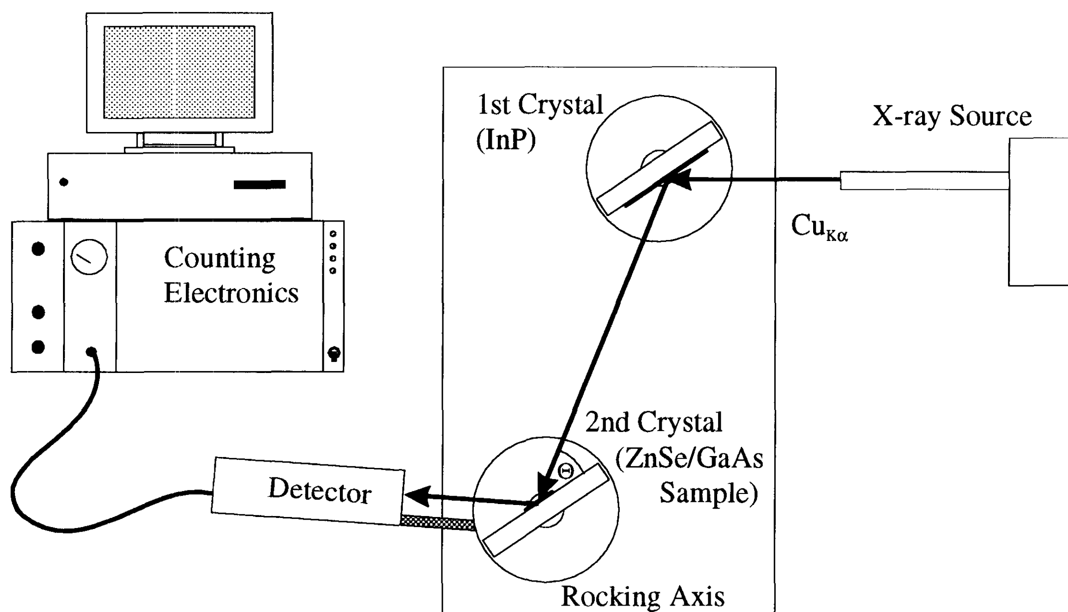

Figure B.1 Schematic drawing of double crystal x-ray diffractometer used to measure rocking curves.

In equation (B.1) λ is the wavelength of the x-rays, d is the spacing between diffraction planes, and Θ is the angle between the incident x-rays and the surface.

The $Cu_{K\alpha 1}$ and $Cu_{K\alpha 2}$ beams were sometimes both incident on the sample since one of the beams was not removed with an aperature. The actual linewidths were broadened by this apparatus limitation if both the x-ray beams were incident on the sample. A good quality GaAs substrate normally has a FWHM of 10-20 arcseconds, but values of 30-40 arcseconds were sometimes recorded.

Appendix C

Photoluminescence

Photoluminescence (PL) is a sensitive optical method to probe the quality of a semiconductor thin film. A PL measurement records the intensity of radiative recombination versus the emission wavelength (often converted to photon energy) from a sample that is optically excited. The optical excitation generates electron-hole pairs in the semiconductor. The photo-generated carriers rapidly relax to the band edges, or if available, to lower energy states within the bandgap. Electron-hole pairs created by optical excitation in a semiconductor at low temperatures (10 K) have three possible recombination pathways: (*i*) band-to-band radiative recombination of free-excitions, (*ii*) band-to-impurity radiative recombination or transitions between defect states within the bandgap, and (*iii*) recombination at a non-radiative center. A film that has few non-radiative electron-hole trap states is more likely to recombine through the paths described in (*i*) and (*ii*) producing more intense luminescence.

Photoluminescence was normally measured at 10 K where the thermal energy available in the lattice phonons was insufficient to dissociate the Coulombic pairing of electrons and holes (excitons). The binding energy of excitons in ZnSe is 21 meV; this large binding energy allows excitons in ZnSe to exist at room temperature. At 10 K the radiative recombination peaks due to free or bound excitons can be extremely sharp (2-3 meV FWHM) and very specific in energy. The features in a PL spectrum can often be identified by the wavelength (energy) at which they appear. Many luminescent transitions in ZnSe originating from a specific impurity or lattice defect have been identified in past low temperature PL studies. Table C.1 identifies some of the known luminescence features

Table C.1 Known luminescence transitions in unstrained ZnSe based on low temperature PL measurements. Values were based on data in Ref. [86] unless otherwise indicated.

Symbol	Transition		Energy (eV)
E_x^1	Free Exciton, light hole		2.802 [105]
I_1^N	Neutral acceptor-bound exciton,	nitrogen	2.791 [87]
I_2^C	Neutral donor-bound exciton,	carbon	2.792
I_2^{Cl}	Neutral donor-bound exciton,	chlorine	2.797
I_2^{GA}	Neutral donor-bound exciton,	gallium	2.798
I_2^{In}	Neutral donor-bound exciton,	indium	2.799

observed in bulk ZnSe. References to the tabulated data will be made in the analysis of PL spectra presented in this thesis. Photoluminescence is capable of detecting impurities at low concentrations, making this one of the most sensitive methods of identifying impurities in semiconductor films.

Recombination also occurs at point and extended defects such as vacancies and dislocations. Due to the greater configurational possibilities which result in a range of possible binding energies, these features are generally much broader than excitonic peaks. Emission associated with recombination at dislocation lines and the Zn and Se atom vacancies have been reported.

The photoluminescence measurements were made with the sample mounted on a closed-cycle He cryostat capable of cooling the sample to 10 K. The bandgap of ZnSe at this measurement temperature was approximately 2.822 eV (see Table 1.1). The large bandgap energy required that a UV laser be used for excitation. A He-Cd laser which has an emission wavelength of 325 nm (3.82 eV) was used. The laser was focused onto the samples producing a relatively low power density of 300 mW/cm^2.

A schematic drawing of the PL apparatus is shown in Figure C.1. Laser light is passed through a beam chopper (BC) and directed at normal incidence to a sample mounted on the cryostat's cold-finger by reflection off a mirror sliver (MS). The sample's

luminescence is collected by the first collimating lens and focused by a second lens onto the aperture of a 1/2 meter spectrometer. The grating spectrometer only passes light of a narrow band of wavelengths into the photomultiplier tube (PMT) which detects the photons. The small output signal is boosted by pre-amplifier before it reaches the lock-in amplifier. The signal-to-noise ratio was improved by modulating the laser at 1000 Hz using the beam chopper which was used as a reference frequency for the lock-in amplifier. The voltage signal from the lock-in amplifier was sampled by an analog-to-digital converter within the control computer. Data collection and analysis were done using the computer. The resolution of the spectrometer has been estimated to be 3 Å or 1 meV in energy [86].

The energy of the radiative recombination of electrons and holes is a function of the bandgap of the material. The states within the bandgap are to first order constant with

Figure C.1 Schematic drawing of photoluminescence apparatus. The laser light path is indicated schematically by the lines. The labels M, L, BC, MS, and PMT correspond to a mirror, lens, beam chopper, mirror sliver, and photomultiplier tube, respectively.

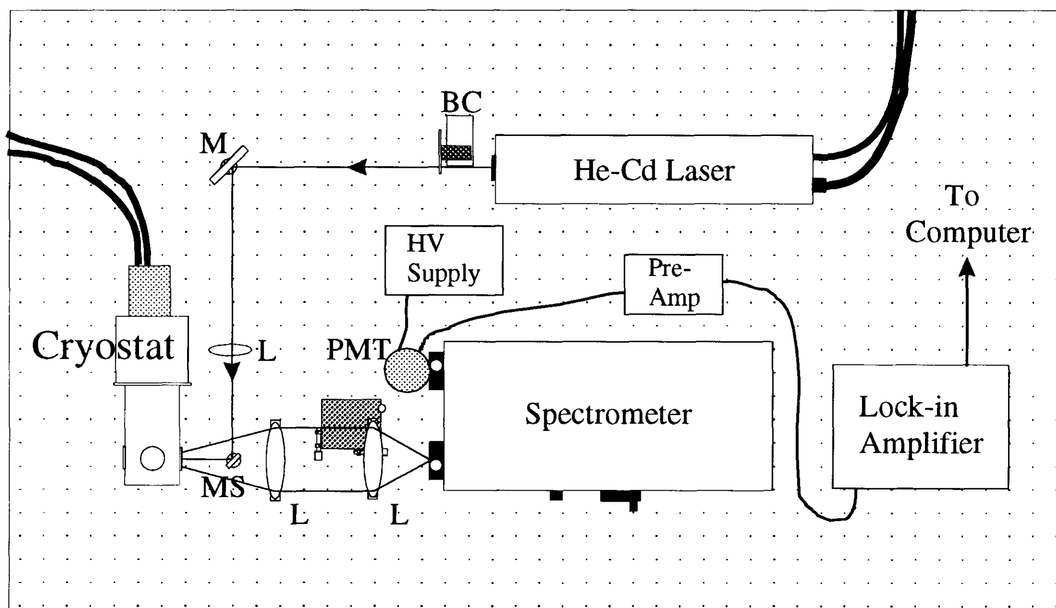

respect to the valence and conduction band edges from which they are measured, hence, any red or blue shift of the energy of a particular feature from its bulk value is due to a change in the bandgap. The bandgap is a function of both temperature and pressure (i.e. strain). At 10 Kelvin or less the bandgap is practically independent of temperature and has a value of 2.822 eV. If PL is measured at higher temperatures the contraction of the bandgap needs to be accounted for using an expression similar to equation 3.4. The bandgap energy shift due to strain is of particular concern since it will blue (red) shift the bulk energy values for a compressive (tensile) strain. The increase in energy of PL features for a pseudomorphic ZnSe film (compressive strain) has been estimated to be ~ 6 meV and the decrease in energy for films 1-2 μm thick under tensile strain to be ~ 2 meV [86]. In the absence of knowledge of the strain present in the film the identification of bound-excitons is ambiguous without additional information. Fortunately, if free-excitons are present, they serve as a reference for the energy shift induced by strain.

Appendix D

Estimate of GSMBE Growth Rate Uncertainty

The GSMBE growth rate was shown in section 4.1.4 to be dependent on the H_2Se flow rate, the Zn beam flux, and the substrate temperature. An estimate of the GR uncertainty is possible based on the uncertainties in these independent variables. Equation (D.1) relates the total uncertainty in the growth rate to the uncertainties in each of the growth variables.

$$\Delta GR(N_{Se}, N_{Zn}, T_{Sub}) = \frac{\partial GR}{\partial N_{Se}}(\Delta N_{se}) + \frac{\partial GR}{\partial N_{Zn}}(\Delta N_{Zn}) + \frac{\partial GR}{\partial T_{Sub}}(\Delta T_{Sub})$$

(Eq. D.1)

In the above expression, N_{Zn} and N_{Se} are the number of molecules or atoms of Zn and Se impinging on the substrate per unit area per second, which will be referred to as the flux. The Se flux was assumed to be an Se_2 beam produced in cracking the hydrogen selenide. GSMBE was shown in Section 4.1.4 to be a mass-transport limited growth process, so the GR was linearly proportional to the incident fluxes. Since ZnSe is a binary compound, the growth rate was limited by the flux which contained the fewest atoms of Zn or Se to incorporate into the film surface. The majority of the films were grown under conditions where one element was mass-transport limited, i.e. Zn- or Se-rich growth. Hence, the uncertainty in the GR was affected by the uncertainty in the flux of the mass-transport limited element only; excess Zn or Se arriving at the surface did not affect the growth rate because Zn or Se coverage beyond one monolayer would desorb. When the ratio of the

Zn to Se on the surface was nearly unity as determined by RHEED reconstructions, the uncertainty in both fluxes was assumed significant.

The effect of the uncertainty in a source flux on the uncertainty in the growth rate can be demonstrated by a simplified example. Assume that growth is occurring at a constant temperature, and that one of the element fluxes is constant and high enough to insure that this element is always in excess at the surface. The GR is then linearly dependent on the mass-transport limiting element flux N, as shown in Equation (D.2). This simple formula, where c is a constant, is the growth rate formula for MBE [52]. The derivative of the GR with respect to the flux is shown in Equation (D.3). The first two terms in Equation (D.1) are the contributions to the GR uncertainty due to the uncertainty in the Se and Zn fluxes.

$$GR = cN \qquad \text{(Eq. D.2)}$$

$$\frac{\partial GR}{\partial N} = c \qquad \text{(Eq. D.3)}$$

$$\left(\frac{\Delta GR}{GR}\right)_{Flux} = \frac{\left(\frac{\partial GR}{\partial N}\right)\Delta N}{GR} = \left(\frac{c\Delta N}{cN}\right) = \left(\frac{\Delta N}{N}\right) \qquad \text{(Eq. D.4)}$$

The percentage uncertainty in the GR due to flux N can be found by dividing a flux uncertainty term in Equation (D.1) by the growth rate expressed in Equation (D.2). The result shown in Equation (D.4) demonstrates that the percentage uncertainty in a source flux causes the same percentage uncertainty in the growth rate.

The zero flow setting of the hydrogen selenide mass flow controller drifted slowly from the 0.0 sccm value. The time scale of the drift was a tenth of a sccm over several days, so drift was not a factor during an experiment. It was necessary to establish what the zero flow setting was prior to initiation of growth so the actual flow could be set correctly. The zero flow value was determined by directing H_2Se into the vent, and recording the flow setting of the MFC where gas was first detected on the vent line cold-

cathode gauge. The offset in the zero flow value was determined to within ±0.1 sccm using this method. The percentage uncertainty in the H_2Se flow (and, hence, Se flux) decreased with increasing flow; a sample of forty experiments had an average uncertainty of 6%.

The uncertainty in the growth rate due to the fluctuating Zn flux was estimated from a simple statistical analysis of the Zn flux values measured before and after growth. Forty experiments were used to obtain values for the average percentage uncertainty and the standard deviation in the percentage uncertainty. The average uncertainty and the standard deviation in the average uncertainty were 5% and 4%, respectively. These values were then added together giving a 9% ΔGR due to the unstable Zn flux.

Estimating the uncertainty due to temperature was more complicated since the GR was observed to be a non-linear function of the substrate temperature as shown in Figure 4.2. In order to get an estimate, the GR dependence on temperature was approximated by a linear function. Equation (D.5) is the approximation function which is shown as a dotted line in Figure 4.2.

$$GR = -(0.002)T_{Sub} + 0.97 \quad (\mu m/hr/^{o}C) \qquad \text{(Eq. D.5)}$$

Taking the derivative of Equation (D.5), substituting into the third term in Equation (D.1), and then dividing by the GR, the percentage change in the GR due to the uncertainty in the substrate temperature is estimated in Equation (D.6) to be,

$$\left(\frac{\Delta GR}{GR}\right)_{T_{Sub}} = \frac{-(0.002)\Delta T_{Sub}}{(-0.002T_{Sub} + 0.97)} \ . \qquad \text{(Eq. D.6)}$$

The substrate temperature was determined to within ±5 °C of an absolute temperature reference using the calibration method described in Section 2.4. The majority of GSMBE experiments were conducted at temperatures less than 300 °C. Assuming a substrate

temperature of 300 °C, and a ±5 °C uncertainty in this value, the percentage uncertainty in the GR was 2%. At lower growth temperatures where the GR was higher, the uncertainty was even lower.

Table D.1 displays the total percentage uncertainty in the GR due to the error terms of Equation (D.1). The uncertainty in the Zn flux was greater than the uncertainty in the H_2Se flow, hence, Zn-limited growth was subject to a greater variance in the growth rate. Any variations in the growth rate due to oscillations of PID controlled instrumentation around their setpoints were assumed to be second order because the PID controllers regulated very closely. The uncertainty in the thickness measurement of ±50 Å was very small compared to film thicknesses of 1-2 μm, so the uncertainty introduced by measurement error is not included in the growth rate uncertainty.

Table D.1 Percentage uncertainty in growth rate (ΔGR/GR) for different growth conditions. Entries are given as the percentage uncertainty in the growth rate caused by the uncertainty in the variable listed.

Variable	Surface Stoichiometry:	Se-Limited	(ΔGR/GR) Zn-Limited	1:1
Substrate Temperature		± 2%	± 2%	± 2%
H_2Se Flow Rate		± 6%	*	± 6%
Zn Effusion Cell Flux		*	± 9%	± 9%
	Total (ΔGR/GR)	± 8%	11%	± 17%

* No contribution to GR uncertainty with the indicated surface stoichiometry.

Bibliography

[1] T. Yasuda, I. Mitsuishi, and H. Kukimoto, *Metalorganic vapor phase epitaxy of low-resistivity p-type ZnSe*, Appl. Phys. Lett. **52** (1988) 57.

[2] H. Cheng, J.M. DePuydt, J.E. Potts, and T.L. Smith, *Growth of p-type ZnSe:Li by molecular beam epitaxy*, Appl. Phys. Lett. **52** (1988) 147.

[3] M. Haase, J. Qiu, J.M. DePuydt, and H. Cheng, *Blue-green laser diodes*, Appl. Phys. Lett. **59**, (1991) 1272.

[4] H. Jeon, J. Ding, W. Patterson, A.V. Nurmikko, W. Xie, D.C. Grillo, M. Kobayashi, and R.L. Gunshor, *Blue-green injection laser diodes in (Zn,Cd)Se/ZnSe quantum wells*, Appl. Phys. Lett. **59** (1991) 3619.

[5] Z. Yu, J. Ren, B. Sneed, K.A. Bowers, K.J. Gossett, C. Boney, Y. Lansari, J.W. Cook, Jr., and J.F. Schetzina, *High-resolution study of stimulated emission from blue-green laser diodes*, Appl. Phys. Lett. **61** (1922) 1266.

[6] I.S. Hausson, S.Y. Wang, J. Simpson, M.R. Taghizadeh, K.A. Prior, and B.C. Cavenett, *Development and characterization of II-VI blue-green diode lasers*, Physica B **191** (1993) 124.

[7] H. Okuyama, T. Miyajima, Y. Morinaga, F. Hiei, M. Ozawa, and K. Akimoto, *ZnSe/ZnMgsSe blue laser diode*, Electron Lett. **28** (1992) 1798.

[8] J.M. Gaines, R.R. Drenten, K.W. Haberern, T. Marshall, P. Mensz, and J. Petruzello, *Blue-green injection lasers containing pseudomorphic* $Zn_{1-x}Mg_xS_ySe_{1-y}$ *cladding layers and operating up to 394 K*, Appl. Phys. Lett. **62** (1993) 2462.

[9] R.M. Park, M.B. Troffer, C.M. Rouleau, J.M. DePuydt, and M.A. Haase, *P-type ZnSe by nitrogen beam doping during molecular beam epitaxial growth*, Appl. Phys. Lett. **57**, (1990) 2127.

[10] K. Ohkawa, T. Karasawa, and T. Mitsuyu, *Characteristics of p-type ZnSe layers grown by molecular beam epitaxy with radical doping*, Jpn. J. Appl. Phys. **30**, (1991) L152.

[11] W. Stutius, *Growth and doping of ZnSe and* ZnS_xSe_{1-x} *by organometallic chemical vapor deposition*, J. Crystal Growth **59** (1982) 1.

[12] D.J. Chadi and K.J. Chang, *Self-compensation through a large lattice relaxation in p-type ZnSe*, Appl. Phys. Lett. **55**, (1989) 575.

[13] R.M. Park, H.A. Mar, and N.M. Salansky, Photoluminescence properties of nitrogen-doped ZnSe grown by molecular beam epitaxy, J. Appl. Phys. **58** (1985) 1047.

[14] T. Mitsuyu, K. Ohkawa, and O. Yamazaki, *Photoluminescence properties of nitrogen -doped ZnSe layers grown by molecular beam epitaxy with low-energy ion doping*, Appl. Phys. Lett. **49** (1986) 1348.

[15] K.J. Gossett, Z.Yu, K.A. Bowers, J.W. Cook, Jr., and J.F. Schetzina, *Optical properties of nitrogen-doped ZnSe and ZnSSe thin films,* paper presented at the 35th Electronic Materials Conference, held in Santa Barbara, CA, June 23-25, 1993.

[16] R.M. Park, *Nitrogen doping of wide-gap II-VI compounds during molecular beam epitaxy,* J. Cryst. Growth, to be published.

[17] A. Taike, M. Migita, and H. Yamamoto, *P-type conductivity control of ZnSe highly doped with nitrogen by metalorganic molecular beam epitaxy*, Appl. Phys. Lett. **56** (1990) 1989.

[18] M. Migita, A. Taike, M. Momose, and J. Gotoh, *Blue-green light-emitting diodes with p-ZnSSe highly doped with nitrogen by MOMBE and MBE*, J. Cryst. Growth, to be published.

[19] R.M. Park, and H.A. Mar, *Growth and photoluminescence characterization of ZnSe layers grown on (100) Ge by molecular beam epitaxy*, J. Mater. Res. **1** (1986) 543.

[20] J. Kleinman, R.M. Park, and H.A. Mar, *On epilayer tilt in ZnSe/Ge heterostructures prepared by molecular beam epitaxy*, J. Appl. Phys. **64** (1988) 1201.

[21] J.C. Phillips, in Bands and Bonds in Semiconductors (Academic Press: New York, 1973).

[22] A. Yariv, in Optical Electronics, 3rd ed. (Holt, Rinehart and Winston: New York, 1985) 280.

[23] E. Kaldis, in Current Topics in Materials Science, Vol. 9 (North-Holland: Amsterdam, 1982).

[24] P.J. Dean, W. Stutius, G.F. Neumark, B.J. Fitzpatrick, and R.N. Bhargava, *Ionization energy of the shallow nitrogen acceptor in zinc selenide*, Phys. Rev. B **27** (1983) 2419.

[25] C.M. Wolfe, N. Holonyak, Jr., G.E. Stillman, in Physical Properties of Semiconductors (Prentice-Hall:Englewood Cliffs, 1989)

[26] A.V. Nurmikko, seminar given at MIT, 1993.

[27] G.E. Hite, Physics Review, 156 (1967) 850.

[28] P.J. Dean, D.C. Herbert, *Donor bound-exciton excited states in zinc selenide*, Phys. Rev. B **23** (1981) 4888.

[29] M.A. Haase, H. Cheng, D.K. Misemer, T.A. Strand, and J.M. Depuydt, *ZnSe-ZnSSe electro-optic waveguide modulators*, Appl. Phys. Lett. **59** (1991) 3228.

[30] B.H. Lee, *Elastic constants of ZnTe and ZnSe between 77 - 300 K*, J. Appl. Phys. **41** (1970) 2984.

[31] W.J. Kozlovsky, W. Lenth, E.E. Latta, A. Moser, and G.L. Bona, *Generation of 41 mW of blue radiation by frequency doubling of a GaAlAs diode laser*, Appl. Phys. Lett. **56** (1990) 2291.

[32] D.B. Eason, C. Boney, J. Ren, Z. Yu, J.W. Cook, Jr., J. F. Schetzina, and N.A. El-Masry, *Quaternary II-VI alloys for blue and green light emitting diode applications*, J. Cryst. Growth, to be published.

[33] S. Guha, J.M. DePuydt, M.A. Haase, J. Qui, and H. Cheng, *Degradation of II-VI based blue-green light emitters*, Appl. Phys. Lett. **63** (1993) 3107.

[34] L.C. Kimerling, *The influence of electronic excitation on the performance and reliability of semiconductor devices*, Reviews of Solid State Science **4**, (1990) 335.

[35] P. Petroff and R.L. Hartman, *Defect structure introduced during operation of heterojunction GaAs lasers*, Appl. Phys. Lett. **23** (1973) 469.

[36] P. W. Hutchinson, P.S. Dobson, S. O'Hara, and D.H. Newman, *Defect structure of degraded heterojunction GaAlAs-GaAs lasers*, Appl. Phys. Lett. **26** (1975) 250.

[37] M.B. Panish, H. Temkin, and S. Sumski, *Gas-source MBE of InP and* $Ga_xIn_{1-x}P_yAs_{1-y}$*: Materials properties and heterostructure lasers*, J. Vac. Sci. Technol. B **3** (1985) 657.

[38] K. Ichino, Y. Wu, Y. Kawakami, Sz. Fujita, and Sg. Fujita, *Metalorganic molecular beam epitaxy of* $Zn_{1-x}Cd_xS_ySe_{1-y}$ *quaternary allows on GaAs substrates*, Jpn. J. Appl. Phys. **30** (1991) L1624.

[39] C.A. Coronado, E. Ho, L.A. Kolodziejski, and C.A. Huber, *Photoassisted metalorganic molecular beam epitaxy of ZnSe*, Appl. Phys. Lett. **61** (1992) 534.

[40] C.A. Coronado, E. Ho, L.A. Kolodziejski, and C.A. Huber, *Laser-assisted growth of ZnSe by Metalorganic Molecular Beam Epitaxy*, Mat. Res. Soc. Symp. Proc., Vol. **263** (1992) 181.

[41] E. Ho, C.A. Coronado, and L.A. Kolodziejski, *Elimination of surface site blockage due to ethyl species in MOMBE of ZnSe*, J. Elect. Mat. **22** (1993) 473.

[42] C.A. Coronado, E. Ho, and L.A. Kolodziejski, *Effect of laser on MOMBE of ZnSe using gaseous and solid sources*, J. Cryst. Growth **127** (1993) 323.

[43] E. Ho, C.A. Coronado, and L.A. Kolodziejski, *Photo-assisted chemical beam epitaxy of II-VI semiconductors*, Mat. Res. Soc. Symp. Proc., Vol. 279 (1993) 635.

[44] C.A. Coronado, E. Ho, P.A. Fisher, J.L. House, K. Lu, G.S. Petrich, and L.A. Kolodziejski, *Gas source molecular beam epitaxy of ZnSe and ZnSe:N*, J. Elect. Mat. **23** (1994) 269.

[45] A. Kamata, H. Mitsuhashi, and H. Fujita, *Origin of the low doping efficiency of nitrogen acceptors in ZnSe grown by metalorganic chemical vapor deposition*, Appl. Phys. Lett. **63** (1993) 3353.

[46] J.A. Wolk, J.W. Ager III, K.J. Duxstad, E.E. Haller, N.R. Tasker, D.R. Dorman, and D.J. Olego, *Local vibrational mode spectroscopy of nitrogen-hydrogen complex in ZnSe*, Appl. Phys. Lett. **63** (1993) 2756.

[47] D.A. McQuarrie, in Statistical Mechanics (Harper & Row: New York, 1976) 180.

[48] L.I. Maissel and R. Glang , in Handbook of Thin Film Technology (McGraw-Hill: New York, 1970)1-16.

[49] H. Ando, A. Taike, R. Kimura, M. Konagai, and K. Takahashi, *Metalorganic molecular beam epitaxial growth of ZnSe using diethylzinc and diethylselenide*, Jpn. J. Appl. Phys. **25** (1986) L279.

[50] N. Kobayashi, Y. Shinoda, and Y. Kobayashi, *Comparative Study of ZnSe growth rate by metal organic molecular beam epitaxy using different Zn sources*, Jpn. J. Appl. Phys. Lett. **27** (1988) L1728.

[51] G.B. Stringfellow, in Organometallic vapor-phases epitaxy, (Academic Press: Boston, 1989) 21.

[52] M.A Herman and H. Sitter, Editors, in Molecular Beam Epitaxy: Fundamentals and Current Status, (Springer-Verlag: Berlin, 1989).

[53] H. Ando, A. Taike, R. Kimura, M. Konagai, and K. Takahashi, *Metalorganic molecular-beam epitaxy of ZnSe and ZnS*, J. Appl. Phys. **62** (1987) 1251.

[54] H. Mitsuhashi, I. Mitsuishi, and H. Kukimoto, *MOCVD growth of ZnSxSe1-x epitaxial layers lattice-matched to GaAs using alkyls of Zn, S and Se*, Jpn. J. Appl. Phys. **24** (1985) L864.

[55] A.J. Murrell, A.T.S. Wee, D.H. Fairbrother, N.K. Singh, J.S. Foord, G.J. Davies and D.A. Andrews, *Surface chemical processes in metal organic molecular-beam epitaxy; Ga deposition from triethylgallium on GaAs (100),* J. Appl. Phys. **68** (1990) 4053.

[56] B.A. Banse, and J.R. Creighton, *The adsorption of triethylgallium on GaAs(100)*, Surface Sci. **257** (1991) 221.

[57] M.A. Rueter and J.M. Vohs, *Adsorption and reaction of diethylzinc on GaAs(100),* J. Vac. Sci. Technol. B **10** (1992) 2163.

[58] C.L. French and J.S. Foord, *Reaction kinetics for the CBE growth of GaAs from triethylgallium; computer modeling studies incorporating recent surface spectroscopic data*, J. Cryst. Growth **120** (1992) 63.

[59] V.M. Donnelly and A. Robertson, Jr., *Kinetic modelling of GaAs chemical beam epitaxy*, Surface Sci. **293** (1993) 93.

[60] D. Rajavel, J.J. Zinck, and J.E. Jensen, *Growth kinetics and properties of (001) ZnSe/GaAs films grown by metalorganic molecular beam epitaxy,* J. Cryst. Growth, to be published.

[61] J.E. Cunningham, AT&T Bell Laboratories (private communication).

[62] D. Rajavel, Hughes Research Laboratories (private communication).

[63] S. Imai, S. Yamazaki, T. Iizuka, O. Sugiura, and M. Matsumura, *Atomic layer epitaxy of germanium using atomic hydrogen,* paper presented at the 35th Electronic Materials Conference, held in Santa Barbara, CA, June 23-25, 1993.

[64] H. Ando, H. Inuzuka, M. Konagai, and K. Takahashi, *Photoenhanced metalorganic chemical vapor deposition of ZnSe films using diethylzinc and dimethylselenide*, J. Appl. Phys. **58**, (1985) 802.

[65] Sz. Fujita, A. Tanabe, T. Sakamoto, M. Isemura, and Sg. Fujita, *Investigations of photo-association mechanism for growth rate enhancement in photo-assisted OMVPE of ZnSe and ZnS*, J. Cryst. Growth **93**, (1988) 259.

[66] A. Yoshikawa, T. Okamoto, T. Fujimoto, K. Onoue, S. Yamaga, and H. Kasai, *Ar ion laser-assisted MOVPE of ZnSe using DMZn and DMSe as reactants*, Jpn. J. Appl. Phys. **29**, (1990) L225.

[67] Y. Aoyagi, M. Kanazawa, A. Doi, S. Iwai, and S. Namba, *Characteristics of laser metalorganic vapor-phase epitaxy in GaAs*, J. Appl. Phys. **60** (1986) 3131.

[68] S.A. Hussien, A.A. Fahmy, N.A. El-Masry, and S.M. Bedair, *A criterion for the suppression of plastic deformation in laser-assisted chemical vapor deposition of GaAs*, J. Appl. Phys. **67** (1990) 3853.

[69] M. Ohishi, H. Saito, H. Okano, and K. Ohmori, *Photo-assisted MBE growth of ZnSe crystals*, J. Crystal Growth **95**, (1989) 538.

[70] R. L. Gunshor, L. A. Kolodziejski, A. V. Nurmikko, and N. Otsuka, Strained-Layer Superlattices: Materials Science and Technology, in Semiconductors and Semimetals, Vol. **33** (T.P. Pearsall, Ed.)(Academic Press: Boston, 1990) 337.

[71] N. Matsumura, T. Fukada, K. Senga, Y. Fukushima, and J. Saraie, *Photo-assisted MBE growth of ZnSe on GaAs substrates*, J. Cryst. Growth **111**, (1991) 787.

[72] J. Simpson, S. J. A. Adams, S.Y. Wang, J. M. Wallace, K. A. Prior, and B. C. Cavenett, *UV laser assisted growth of molecular beam epitaxial ZnSe*, J. Crystal Growth 117, (1992) 134.

[73] B.V. Shanabrook, J.R. Waterman, J.L. Davis, and R.J. Wagner, *Large temperature changes induced by molecular beam epitaxial growth on radiatively heated substrates*, Appl. Phys. Lett. **61** (1992) 2338.

[74] H. Hou, Z. Zhang, U. Ray, and M. Vemon, *A crossed laser molecular-beam study of the photodissociation dynamics of* $Zn(C_2H_5)_2$ *and* $(Zn(C_2H_5)_2)_2$ *at 248 and 193 nm*, J. Chem. Phys. **92** (1990) 1728.

[75] A. Yoshikawa, *Ar ion laser-assisted metalorganic vapor phase epitaxy of ZnSe*, Physica B **185** (1993) 50.

[76] A. Yoshikawa, T. Okamoto, and T. Fujimoto, *Effects of Ar ion laser irradiation on MOVPE of ZnSe using DMZn and DMSe as reactants*, J. Cryst. Growth **107** (1991) 653.

[77] J. Zheng, J.W. Allen, D.E. Spence, W.E. Sleat, and W. Sibbett, *Decay time of the blue luminsecence in ZnSe at room temperature*, Appl. Phys. Lett. **62** (1993) 63.

[78] J.A. McCaulley, V.R. McCrary, and V.M. Donnelly, *Laser-induced decomposition of triethylgallium and trimethylgallium absorbed on GaAs(100)*, J. Phys. Chem. **93** (1989) 1148.

[79] J. Petruzzello, B. Greenberg, D. Cammack, and R. Dalby, *Structural properties of the ZnSe/GaAs system grown by molecular-beam epitaxy*, J. Appl. Phys. **63** (1988) 2299.

[80] J.M. Gaines, J. Petruzzello, and B. Greenberg, *Structural properties of ZnSe films grown by migration enhanced epitaxy*, J. Appl. Phys. **73** (1993) 2835.

[81] P.J. Dean, D.C. Herbert, C.J. Werkhoven, B.J. Fitzpatrick, and R.N. Bhargava, *Donor bound-exciton excited states in zinc selenide*, Phys. Rev. B **23** (1981) 4888.

[82] M. Imaizumi, Y. Endoh, K. Ohtsuka, T. Isu, and M. Nunoshita, *Active-nitrogen-doped p-type ZnSe grown by gas-source molecular beam epitaxy for blue-light-emitting devices*, Jpn. J. Appl. Phys. **32** (1993) L1725.

[83] M. Imaizumi, Y. Endoh, K. Ohtsuka, M. Suita, T. Isu, and M. Nunoshita, *Blue light emitting laser diodes based on ZnSe/ZnCdSe structure grown by gas source molecular beam epitaxy*, Jpn. J. Appl. Phys. **33** (1994) L13.

[84] A. Yoshikawa, T. Okamoto, H. Yasuda, S. Yamaga, and H. Kasai, *"MBE-like" and "CVD-like" atomic layer epitaxy of ZnSe in MOMBE system*, J. Cryst. Growth **101** (1990) 86.

[85] Hydrogen in Semiconductors: Semiconductors and Semimetals, vol. 34 (Academic Press; Boston).

[86] J.L. House, Optical Characterization of ZnSe by Photoluminescence, Master's Thesis, Massachusetts Institute of Technology, (1994).

[87] J. Qui, J.M. DePuydt, H. Cheng, and M.A. Haase, *Heavily doped p-ZnSe:N grown by molecular beam epitaxy*, Appl. Phys. Lett. 59 (1991) 2992.

[88] H. Cheng, J.M. DePuydt, J.E. Potts, and M.A. Haase, *Growth of p- and n-type ZnSe by molecular beam epitaxy*, J. Cryst. Growth **95** (1989) 512.

[89] S.M. Shibli, M.C. Tamargo, B.J. Skromme, S.A. Schwarz, C.L. Schwartz, R.E. Nahory, R.J. Martin, *Arsenic doped ZnSe grown by molecular-beam epitaxy*, J. Vac. Sci. Technol. B **8** (1990) 187.

[90] T. Yao and Y. Okada, *Phosphorus acceptor levels in ZnSe grown by molecular beam epitaxy*, Jpn. J. Appl. Phys. **25** (1986) 821.

[91] J.M. DePuydt, T.L. Smith, J.E. Potts, H. Cheng, and S.K. Mohapatra, *Detection and control of impurity incorporation in MBE-grown ZnSe*, J. Cryst. Growth 86 (1988) 318.

[92] K. Akimoto, T. Miyajima, and Y. Mori, *Photoluminescence spectra of oxygen-doped ZnSe grown by molecular-beam epitaxy*, Phys. Rev. B **39** (1989) 3138.

[93] M.A. Haase, H. Cheng, J.M. DePuydt, and J.E. Potts, *Characterization of p-type ZnSe*, J. Appl. Phys. **67** (1990) 448.

[94] G. Mandel, *Self-compensation limited conductivity in binary semiconductors, I. Theory*, Phys. Rev. **134** (1964) A1073.

[95] F.A. Kroger and H. J. Vink, in Solid State Physics, Vol. 3, (Edited by F. Seitz and D Turnbull) (Academic Press: New York, 1956) p.310.

[96] D.J. Chadi, *Column V acceptors in ZnSe: Theory and experiment*, Appl. Phys. Lett. **59** (1991) 3589.

[97] C.G. van de Walle, D.B. Laks, G.F. Neumark, and S.T. Pantelides, *First-principles calculations of solubilities and doping limits: Li, Na, and N in ZnSe*, Phys. Rev. B **47** (1993) 9425.

[98] K.W. Kwak, R.D. King-Smith, and D. Vanderbilt, *Pseudopotential total-energy calculations of column-V acceptors in ZnSe*, Physica B **185** (1993) 154.

[99] P. Hohenberg and W. Kohn, *Inhomogeneous electron gas*, Phys. Rev. **136** (1964) B864.

[100] D.R. Hamann, M. Schlüter, and C. Chiang, *Norm-conserving pseudopotentials*, Phys. Rev. Lett. **43** (1979) 1494.

[101] R.K. Watts, W.C. Holton, and M. de Wit, *Phosphorus and arsenic impurity centers in ZnSe. I. Paramagnetic Resonance*, Phys. Rev. B **3** (1971) 404.

[102] B.C. Cavenett, *Optically detected magnetic resonance (O.D.M.R.) investigations of recombination processes in semiconductors*, Adv. in Phys. **30** (1981) 475.

[103] J. Michel, Massachusetts Institute of Technology, (private communication).

[104] S. Ito, M. Ikeda, and K. Akimoto, *Plasma doping of nitrogen in ZnSe using electron cyclotron resonance*, Jpn. J. Appl. Phys. 31 (1992) L1312.

[105] S. Matsumoto, H. Tosaka, T. Yoshida, M. Kobayashi, and A. Yoshikawa, *Planar-doping of molecular beam epitaxy grown ZnSe with plasma-excited nitrogen*, Jpn. J. Appl. Phys. **32** (1993) L229.

[106] Y. Fan, J. Han, L. He, J. Saraie, R. L. Gunshor, M. Hagerott, H. Jeon, A.V. Nurmikko, G.C. Hua, and N. Otsuka, *Graded band gap ohmic contact to p-ZnSe*, Appl. Phys. Lett. **61** (1992) 3160.

[107] Y. Lansari, J. Ren, B. Sneed, K.A. Bowers, J.W. Cook, Jr., and J.F. Schetzina, *Improved ohmic contacts for p-ZnSe and related p-on-n diode structures*, Appl. Phys. Lett. **61** (1992) 2554.

[108] S.M. Sze, in Physics of Semiconductor Devices (John Wiley & Sons: New York, 1981) 248.

[109] Sz. Fujita, T. Asano, K. Maehara, and Sg. Fujita, *Nitrogen doping in ZnSe by photo-assisted metalorganic vapor phase epitaxy*, J. Elect. Mat. **23** (1994) 263.

[110] G. Herberg, in Molecular Spectra and Molecular Structure II: Infrared and Raman Spectra of Polyatomic Molecules (Van Nostrand: New York, 1966), p. 295.

[111] H. Karata, M. Hirose, and Y. Osake, *Wide optical-gap, photoconductive* $a\text{-}Si_xN_{1-x}:H$, Jpn. J. Appl. Phys. **20** (1981) L811.

[112] J.I. Pankove, D.E. Carlson, J.E. Berkeyheiser, and R.O. Wance, *Neutralization of shallow acceptor levels in silicon by atomic hydrogen*, Phys. Rev. Lett. **51** (1983) 2224.

[113] S. J. Pearton, W.C. Dautremont-Smith, J. Chevallier, C.W. Tu, and K.D. Cummings, *Hydrogenation of shallow-donor levels in GaAs*, J. Appl. Phys. **59** (1986) 2821.

[114] G.R. Antell, A.T.R. Briggs, B.R. Butler, S.A. Kitching, J.P. Stagg, A. Chew, and D.E. Sykes, *Passivation of zinc acceptors in InP by atomic hydrogen coming from arsine during metalorganic vapor phase epitaxy*, Appl. Phys. Lett. **53** (1988) 758.

[115] N.R. Tasker, B.A. Khan, D.R. Dorman, and K. Shahzad, *Novel technique for p-type nitrogen doped ZnSe epitaxial layers*, Appl. Phys. Lett. **62** (1993) 270.

[116] I.S. Hauksson, J. Simpson, S.Y. Wang, K.A. Prior, and B.C. Cavenett, *Compensation processes in nitrogen doped ZnSe*, Appl. Phys. Lett. **61** (1992) 2208.

[117] Z. Zhu, K. Takebayashi, K. Tanaka, T. Ebisutani, J. Kawamata, and T. Yao, *Photoluminescence properties of nitrogen-doped ZnSe grown by molecular-beam epitaxy*, Appl. Phys. Lett. **64** (1994) 91.

[118] K.J. Gossett, Z. Yu, K.A. Burns, J. Ren, C.A. Schetzina, and J.F. Schetzina, *Optical properties of p-type nitrogen-plasma-doped ZnSe and ZnSSe thin films*, J. Cryst. Growth, to be published.

[119] B.N. Murdin, B.C. Cavenett, C.R. Pidgeon, J. Simpson, I. Hauksson, and K.A. Prior, *Optically detected magnetic resonance of deep centers in molecular beam epitaxy ZnSe:N*, Appl. Phys. Lett. **63** (1993) 2411.

[120] M. Karai, K. Kido, H. Naito, K. Kurosawa, and M. Okuda, *Defect states in ZnSe single crystals irradiated with gamma rays*, J. Appl. Phys. **69** (1991) 291.

[121] D.J. Chadi and N. Troullier, *Self-compensation in nitrogen-doped ZnSe*, Physica B **185** (1993) 128.

[122] D.J. Chadi, *Self-interstitial bonding configurations in GaAs and Si*, Phys. Rev. B **46** (1992) 9400.

[123] B. Hu, G. Karczewski, H. Luo, N. Samarth, and J.K. Furdyna, *Deep hole traps in p-type nitrogen-doped ZnSe grown by molecular beam epitaxy*, Appl. Phys. Lett. **63** (1993) 358.

[124] J.S. Massa, G.S. Butler, A.C. Walker, J. Simpson, K.A. Prior, and B.C. Cavenett, *Photoluminescence decay measurements of n-and p-type doped ZnSe grown by molecular beam epitaxy*, Appl. Phys. Lett. 64 (1994) 589.

MIT Libraries
Document Services

Room 14-0551
77 Massachusetts Avenue
Cambridge, MA 02139
Ph: 617.253.5668 Fax: 617.253.1690
Email: docs@mit.edu
http://libraries.mit.edu/docs

DISCLAIMER OF QUALITY

Due to the condition of the original material, there are unavoidable flaws in this reproduction. We have made every effort possible to provide you with the best copy available. If you are dissatisfied with this product and find it unusable, please contact Document Services as soon as possible.

Thank you.

Some pages in the original document contain pictures, graphics, or text that is illegible.